CHALMERS
UNIVERSITY OF TECHNOLOGY

PHD THESIS

Snow Contamination of Cars

Adhesive Particle Collisions with Exterior Surfaces

TOBIAS EIDEVÅG

DEPARTMENT OF CHEMISTRY AND CHEMICAL ENGINEERING
CHALMERS UNIVERSITY OF TECHNOLOGY
Gothenburg, Sweden 2022
www.chalmers.se

THESIS FOR THE DEGREE OF DOCTOR OF PHILOSOPHY

Snow Contamination of Cars

Adhesive Particle Collisions with Exterior Surfaces

Tobias Eidevåg

Department of Chemistry and Chemical Engineering

CHALMERS UNIVERSITY OF TECHNOLOGY

Gothenburg, Sweden, 2022

Snow Contamination of Cars
Adhesive Particle Collisions with Exterior Surfaces

TOBIAS EIDEVÅG
ISBN: 978-91-7905-666-7

Doktorsavhandlingar vid Chalmers tekniska högskola
Ny serie nr 5132.
ISSN 0346-718X

Department of Chemistry and Chemical Engineering
Chalmers University of Technology
SE-412 96, Gothenburg
Sweden
Telephone + 46 (0)31-772 1000

Cover
Photograph of a car driving on a snow-covered road.

Printed by Chalmers digitaltryck,
Gothenburg, Sweden 2022.

Snow Contamination of Cars

Adhesive Particle Collisions with Exterior Surfaces

Tobias Eidevåg

Department of Chemistry and Chemical Engineering
Chalmers University of Technology

Abstract

An ongoing challenge regarding autonomous vehicles is the obstruction of sensors by contaminants on exterior surfaces. This often occurs when driving in harsh weather conditions, where the contaminant can be, for example, water spray, dirt, or snow. Certain regions on a vehicle can have higher rates of deposition compared to others and it is therefore crucial when developing an autonomous vehicle to choose sensor locations that avoid contamination. The present research has aimed to increase the knowledge regarding snow deposition when a vehicle is driving on a snow-covered road.

Mathematical models for the cohesive properties of snow and ice have been developed to predict and understand snow deposition on exterior vehicles surfaces. The models were solved analytically or numerically for ice particle collisions with exterior surfaces. Multiple experimental studies were conducted ranging from small-scale experiments on millimeter-sized single ice particle collisions to large-scale climate wind tunnel experiments on bluff bodies. The cohesive properties of snow were measured using an experimental setup for the angle of repose of snow.

In summary, this thesis presents results for single ice particle collisions, the angle of repose of snow, and snow contamination on bluff bodies. A regime map for ice particle collisions was developed that predicts a nonlinear dependency between impact velocity and collisional damping. The angle of repose of snow was shown to strongly correlate with temperature, but also with particle size and fall height. Experimental results for the snow contamination of bluff bodies show that snow tends to deposit near aerodynamic wake regions and reattachment regions where the airflow velocities are expected to be low. A numerical model was proposed for the transport of ice particles in a turbulent flow. Simulations that replicate the experiments, show that the numerical model captures the main characteristics of the snow deposition obtained in the experiments.

Keywords: exterior soiling, snow adhesion, icing, snow physics, premelting, sensor availability, turbulent dispersion, particle laden flow, snow deposition, particle resuspension.

List of Publications

This thesis is based on the work contained in the following publications:

I. T. Eidevåg, P. Abrahamsson, M. Eng, A. Rasmuson
“Modeling of dry snow adhesion during normal impact with surfaces”
Powder Technology, 361, 1081–1092. 2020.
doi.org/10.1016/j.powtec.2019.10.085

II. T. Eidevåg, E. S. Thomson, S. Sollén, J. Casselgren, A. Rasmuson
“Collisional damping of spherical ice particles”
Powder Technology, 383, 318-327. 2021.
doi.org/10.1016/j.powtec.2021.01.025

III. T. Eidevåg, E. S. Thomson, D. Kallin, J. Casselgren, A. Rasmuson
“Angle of Repose of Snow: An experimental study on cohesive properties”
Cold Regions Science and Technology, 194, 103470. 2022.
doi.org/10.1016/j.coldregions.2021.103470

IV. T. Eidevåg, D. Kallin, M. Eng, T. S. B. Narahari, Y. Bharadhwaj, J. Casselgren, A. Rasmuson
“Snow contamination of simplified automotive geometries: A comparison between wind tunnel experiments and numerical modeling”
WCX SAE World Congress Experience, SAE Technical Paper, 2022-01-0901. doi.org/10.4271/2022-01-0901

Other relevant publications

[a] H. Bahaloo, T. Eidevåg, P. Gren, J. Casselgren, F. Forsberg, P. Abrahamsson, M. Sjödahl “Ice sintering: Dependence of sintering force on temperature, load, duration, and particle size”
Journal of Applied Physics, 131, 025109,2022.
doi.org/10.1063/5.0073824

Contribution Report

Paper I: I developed the computational model and made all added code implementations in the DEM software. I designed and performed the DEM simulations. I performed the evaluation of the results with feedback from the co-authors. I am the main author of the paper.

Paper II: I performed the experiments with help from S. Sollén. I developed and performed the image analysis of the experiments. I evaluated the experimental results together with the co-authors. I developed the collisional damping model proposed in the paper as well as the regime map. I am the main author of the paper.

Paper III: I designed the experimental setup and performed all experiments with help from D. Kallin and J. Casselgren. I performed the snow characterization of the samples used in the study. I evaluated the results and revised the manuscript based on the feedback from the co-authors. I am the main author of the paper.

Paper IV: I supervised the development of the Ahmed body test object and participated in the experiments on the Ahmed body. The paper is based on work done by master thesis students, and I implemented the numerical aerodynamic model based their work. I derived and implemented: the adhesion model, the resuspension criterion, and the virtual wall model. I made the grid evaluation as well as the comparison to previous studies. I performed all the simulations in the paper. I evaluated the results with feedback from the co-authors. I am the main author of the paper.

Acknowledgments

First, I want to reach out and thank all the people who have helped me throughout my PhD study. I'm thankful for all the workshop technicians, wind tunnel personal, as well as all engineers and researchers that have found the time to help me when I was in need.

I would like to thank my supervisor, Anders Rasmuson, for all the academic freedom and support he has given me. I feel blessed to have a supervisor that has always been encouraging while I have been exploring a diversity of ideas. Thank you also for always being available to review my work and for the nice discussions about science, hiking, and life in general.

Special thanks to Erik Thomson at Gothenburg University for all your support within ice physics as well as the great feedback you have given on academic writing.

Thanks to both Matthias Eng and David Kallin for their project support from Volvo Cars side. Matthias, thank you for initiating the research project and helping me to start the research and thank you David for continuing in Matthias' footsteps and for all your dedication on finalizing the research.

I would like to express my gratitude towards everyone at the division of Fluid and Experimental Mechanics at Luleå University of Technology where I received a warm welcome during my research visit in 2019. Special thanks to my co-supervisor Johan Casselgren for always being positive and open to discussing new ideas. Thanks to Per Gren for all the help developing the experimental setup for measuring the coefficient of restitution. Thanks also to Hassan Bahaloo for all of the interesting talks about contact mechanics and the adhesion of ice.

Thanks to everyone at Contamination and Core CFD (Volvo Cars) as well as everyone at Chemical Engineering (Chalmers). I'm gratefully to have such great colleagues at both offices.

Thanks to the thesis students I have supervised for all your great work, and thanks for giving me the opportunity to mentor you in your thesis work. I hope you all have learned as much working with me as I have done by mentoring you.

This work has been financially supported by Volvo Cars and Vinnova within the strategic vehicle research and innovation programme FFI (2017-03029), which I gratefully acknowledge.

Finally, I want to express my gratitude to my close friends and family who are always there for me. Thanks to my best friend and wife, and love of my life, Emily.

Contents

Chapter 1

Introduction

1.1 Snow Deposition on Sensor Surfaces of Cars

Safety systems in vehicles have increased in functionality in recent years, from passive systems, such as airbags and seat belts, into active systems such as brake assistance and collisional avoidance.

This development has led to a reduction in accidents, for example, insurance data reveals that collision avoidance features have reduced rear-end collisions by 37% in Sweden [1]. Advancement within machine learning has accelerated this development and today practically all car manufacturers develop sophisticated cruise control systems with the goal of achieving an autonomous system (self-driving) [2]. A self-driving car will rely on on-board sensors that give input to the autonomous system. Commonly used sensors are radars, cameras, lidars, and ultrasonic sensors. Harsh weather conditions caused by rain, fog or snow can impair the performance of these sensors and potentially cause malfunction of an autonomous system. These phenomena, when the exterior surfaces of a vehicle get soiled by a contaminant, are referred to as surface contamination where the contaminant (snow, water, or dirt) obstructs the sensor by depositing on sensor surfaces. Many studies have previously been conducted regarding water as the surface contaminant, and the topic is then referred to as vehicle soiling or exterior water management [3–7].

This work is about surface contamination when the contaminant is snow, i.e., snow contamination. Winter season causes snowy roads in large areas of the Northern Hemisphere, where snow covers up to half of this hemisphere in midwinter [8]. Over 70% of the US population lives in areas with annual snowfall of more than 5 inches (13 cm) [9] and snowy roads account for 24% of all weather-related vehicle crashes in US [9]. Approximately half of the population in Europe lives in areas with yearly snow cover in January, and all regions in Sweden get annual snow. Many drivers can therefore be affected by snow contamination when it causes malfunction of safety systems. Annual winter weather reduces visibility and decreases pavement friction, which increases the likelihood of vehicle accidents. Snowy roads can therefore cause situations where active safety systems for vehicles driving on these roads are less available precisely when they are needed the most. As an example, Jokela et al. [10] tested various lidars, and all sensors in question malfunctioned during the snow tests [10]. Despite these challenges, only few experimental [11, 12] and numerical [13–15] studies have been conducted regarding snow contamination on vehicles, and most studies have been conducted in recent years. There is especially a gap regarding the understanding of how and where snow is expected to accumulate when driving on a snow-covered road.

The phenomena of snow contamination when driving on winter roads can be divided into three types of driving scenarios: self-contamination, third-party contamination, and precipitation contamination. Self-contamination is occurring when the driving car lifts snow from the ground via the tires and the vehicle is then contaminating itself. This type of contamination is always present if there is a sufficiently thick snow layer on the road. Third-party contamination occurs when the car of interest is driving in a snow cloud generated by another vehicle in front of the vehicle, and this type of contamination is then in practice always present together with self-contamination. The scenario is typically worse when the frontal area of the third-party vehicle is large, for example, a truck, since the aerodynamic wake behind it then will be large which is directly related to the generated snow cloud. Precipitation contamination is referred to the scenario when a car is driven during snowfall and often occurs together with self-contamination. In exterior water management, this type of scenario (during rainfall) is often referred to as ”primary contamination” [4] or ”direct soiling” [3], however since snow can accumulate and stay on the road for a long time, this is not, generally speaking, a primary source of contamination. To avoid confusion such terminology is not used in this thesis.

This thesis addresses snow contamination of cars by describing the problem using mechanistic mathematical models. The intention of this research has been to predict when snow will adhere and accumulate on exterior surfaces. However, the increased understanding of the underlying transport phenomenon is also expected to aid in the understanding of how accumulation of snow can be avoided. The results in this work were intended to be general, enabling them to be applied to any situation where adhesive particles adhere and accumulate on surfaces.

1.2 Aim and Objectives

The aim of this thesis is to contribute to the understanding of snow contamination of cars. This has been achieved by addressing the following objectives:

- Investigate and quantify the cohesive properties of snow experimentally in terms of temperature, particle size, etc.
- Investigate collisions of ice particles and how material properties affect the adhesive loss in a collision.
- Develop a computational model for ice particle-wall collisions predicting the energy loss in the collisions.
- Experimentally study the snow contamination of aerodynamic bluff bodies.
- Establish a complete computational model for snow contamination of aerodynamic bluff bodies.

1.3 Limitations

The research focus of this thesis is on the driving scenarios: self-contamination and third-party contamination. Precipitation contamination is regarded as less well defined and experiments are also more difficult to perform with repeatability.

The particles are assumed to be spheroid shaped. Less attention was directed towards precipitation particles with complex shapes such as needles, plates, and dendrites. While the ranges of forms are highly complex and sensitive to atmospheric conditions, they are expected to change towards round particles over time when at rest on the ground.

The snow studied in this work was assumed to be free of any impurities that would alter the freezing point, such as salt, and we furthermore assumed that electrostatic charges are not present at the surface of ice. The snow is studied at temperatures below 0 °C and thus we excluded studying complex melt forms of snow near 0 °C such as slush, where round ice particles are immersed in water.

The motivation for this research is to assert when vehicle sensors are available while driving on snow-covered roads. However, this thesis does not include predictions of how sensors perform when snow is present on a sensor surface. Instead, surface areas with snow present are simply regarded as blocked for any potential sensor, and complex sensor processes such as sensor fusion are not taken into account in the thesis.

1.4 Thesis Outline

This thesis proceeds with a chapter summarizing previous research conducted in the most relevant scientific disciplines on the topic of this thesis (Chapter 2). Then, tests on the snow contamination of cars follows in Chapter 3, which show results from in-field as well as wind tunnel tests. Subsequently, three chapters follow which summarize the current research, where the chapters are defined thematically, and each chapter includes sections on the scientific approach, results, and discussions. Chapter 4 addresses the energy losses for ice particles colliding with massive walls, where the simulation results from Paper I and the experimental results in Paper II are combined to formulate an overall regime map for ice particle-wall collisions. Chapter 5 is about the angle of repose of snow, where the experimental method and results from Paper III are presented. The succeeding chapter addresses snow deposition when a turbulent flow field is present, using simplified bluff bodies (Chapter 6) where the chapter contains both wind tunnel experiments and in-field tests. The results of Paper IV are summarized in Chapter 6, however the chapter also includes recent results obtained from in-field tests on the bodies that are not included in Paper IV. Chapter 7 consists of short summaries of the publications this work is based on, and finally Chapter 8 condenses the concluding remarks of the thesis.

Chapter 2

Background

The work in this thesis extends across multiple scientific disciplines. While the core of the topic is about adhesive particles within chemical engineering, scientific fields such as fluid mechanics, atmospheric science, and automotive engineering are all relevant for the work presented in this thesis. This chapter summarizes, from the aforementioned fields, the most important theoretical concepts for the thesis.

2.1 Snow and Ice Physics

Snow is a complex material in regard to many chemical and physical aspects, with multiple perspectives and definitions. This work is dedicated foremost to the snow present on the ground and snow is defined as a porous material consisting of ice particles and pore space. Utilizing the international classification for seasonal snow on the ground [16], the morphology class round grains is central to the thesis, however machine made snow, surface hoar, and precipitation particles are also relevant. Terminology for bulk entities of snow such as snow particles or grains will be avoided and instead, in order to increase clarity, the entities of snow are referred to as ice particles. It is common to classify snow as either wet or dry, depending on if the snow is at or below its melting temperature [17]. This is not necessarily the standard bulk melting temperature of water (0 °C) since melting point depression can be caused by ionic impurities or curvature [18]. This thesis examines dry snow in the sense that the bulk ice is below the melting point, however, this does not mean that the ice is free of any liquid. Ice is the crystalline solid form of water, and a liquid-like layer can exist on the surface of ice at thermodynamic equilibrium for temperatures well below the bulk melting temperature of water [19–21].

For common temperatures on Earth ($T > -50$ °C) ice is to be considered close to its melting point. A measure of how close a material is to its melting temperature is the homologous temperature, which is defined as;

$$T_H = \frac{T}{T_m}, \tag{2.1}$$

where T is the material temperature, and T_m is the bulk melting temperature. Ice at -55 °C corresponds to $T_H = 80\%$ which is to be regarded as a high temperature for the material [22]. As a comparison, $T_H = 80\%$ for iron or silver would correspond to 1174 °C or 714 °C. Ice at $T = -10$ °C corresponds to $T_H = 0.96$, which is an exceptionally high value of T_H and can be compared to heated stones, or lava, when heated to 1141 °C.

2.1.1 The Premelting of Ice

A crystalline material can start to form a disordered structure among the top molecules at the surface of the material when the material is close to its melting point. This phenomenon is called premelting and can occur on a surface which is in contact with vapor (surface melting) or can occur at the interface between two objects (interfacial melting). Premelting occurs for many crystalline materials, e.g., in ceramics [23] or ice [19]. Michael Faraday postulated the existence of a liquid layer on ice below its melting point already in 1842, and proved this theory experimentally [19]. This was however disputed by James Thomson who instead incorrectly accredited the experimental results to pressure melting [24]. For a long time, the theory of premelting was overlooked by the scientific community, but in the 1950s new experiments were conducted that provided evidence of the existence of premelting on ice [25]. The premelting of ice is currently an active research topic with many recent studies investigating the implications of premelting. 70% of Earth is covered by water, and premelting has been found to explain many interesting phenomena on Earth such as the possibility to ice skate [24], mass charges of thunderstorms [26], frost heave [20], and glacier movement [20].

The distorted layer that arises because of premelting on the surface of ice can have properties between solid ice and liquid water [21]. In this thesis, this layer will therefore be referred to as a quasi-liquid layer (QLL). The presence of a stable QLL can be explained with interfacial thermodynamics. A derivation for the QLL thickness d in thermodynamic equilibrium will now be shown based on the work by Dash et al. [20, 26] and Thomson [27]. As a start, consider a solid to be in thermodynamic equilibrium with a vapor at temperature T and pressure P. If there is a finite QLL of thickness d, the free energy per unit area of this layer will be the sum of the free energy of the bulk and surface terms, i.e.

$$G_{qll}(T, P, d) = [\rho_l \mu_l(T, P)]d + F_{total}, \tag{2.2}$$

where ρ_l is the density of the liquid, F_{total} is the total excess surface free energy per unit area, and $\mu_l(T, P)$ is the chemical potential of the bulk liquid. The chemical potential of the QLL is then,

$$\mu_{qll}(T, P, d) = \frac{1}{\rho_l}\frac{\partial G_{qll}}{\partial d} = \mu_l(T, P) + \frac{1}{\rho_l}\frac{\partial F_{total}}{\partial d}. \tag{2.3}$$

In thermodynamic equilibrium, μ_{qll} is equal to the chemical potential of the solid μ_s, i.e.

$$\mu_{qll}(T, P) = \mu_l(T, P) + \frac{1}{\rho_l}\frac{\partial F_{total}}{\partial d} = \mu_s(T, P). \tag{2.4}$$

This equation implies a difference in chemical potential between the solid and the bulk liquid caused by the derivative of F_{total}. This causes a displacement of the phases, which can be evaluated using a first-order Taylor expansion such as:

$$\Delta\mu(T,P) = \mu_s(T,P) - \mu_l(T,P) = \frac{q_m}{T_m}(T - T_m) + \frac{\rho_l - \rho_s}{\rho_l \rho_s}(P - P_m), \quad (2.5)$$

where q_m is the latent heat of fusion, and ρ_s is the density of the solid. Putting together Eq. (2.4) and Eq. (2.5), it follows that

$$\Delta\mu(T,P) = \frac{1}{\rho_l}\frac{\partial F_{total}}{\partial d} = \frac{q_m}{T_m}(T - T_m) + \frac{\rho_l - \rho_s}{\rho_l \rho_s}(P - P_m). \quad (2.6)$$

The derivative of F_{total} can be expressed as [28]

$$\frac{\partial F_{total}}{\partial d} = -\frac{A_H}{6\pi d^3}, \quad (2.7)$$

where A_H is the effective Hamaker coefficient representing the strength of the polarization forces. Inserting Eq. (2.7) in Eq. (2.6), it can be shown that

$$d = \left(\frac{|A_H|}{6\pi\rho_l(\frac{q_m}{T_m}(T_m - T) + \frac{\rho_l - \rho_s}{\rho_l \rho_s}(P_m - P))} \right)^{1/3}. \quad (2.8)$$

Dash et al. [20] used a different notation where the derivative of F_{total} was expressed as

$$\frac{\partial F_{total}}{\partial d} = \frac{3\Delta\gamma\sigma^2}{d^3}, \quad (2.9)$$

where σ is a constant on the order of a molecular diameter. $\Delta\gamma$ is the difference between the coefficients of dry and wetted interfaces,

$$\Delta\gamma = \gamma_{lv} + \gamma_{sl} - \gamma_{sv}, \quad (2.10)$$

where subscript l is for liquid, v is for vapor, and s is for solid. Combining Eq. (2.7) and Eq. (2.9), the Hamaker coefficient can be expressed as

$$A_H = 12\pi\Delta\gamma\sigma^2. \quad (2.11)$$

Fig. 2.1 shows the predicted d as a function of T (solid line) where $\Delta\gamma = -0.024$ J/m^2 [29] was used together with $\sigma = 2.8$ Å, yielding $A_H = -7.1 \cdot 10^{-20}$ J. The dashed line indicates the molecular length of one water molecule.

The displacement $\Delta\mu(T,P)$ can increase in the presence of impurities μ_s (for instance salt [30]), by an electrostatic potential μ_e [27], or by damage at the interface μ_D due to a collision [26]. Wåhlin and Klein-Paste [30] expressed the chemical potential due to salt as

$$\mu_s = R_0 T \ln(\alpha_w), \quad (2.12)$$

where R_0 is the gas constant and α_w is the activity of the solution. An electrostatic potential can be present when there is an ionic solution, and Thomson [27] derived that

$$\mu_e = \frac{q_s^2}{\rho_l \epsilon\epsilon_0}(1 - \frac{1}{\kappa d})\exp(-\kappa d), \quad (2.13)$$

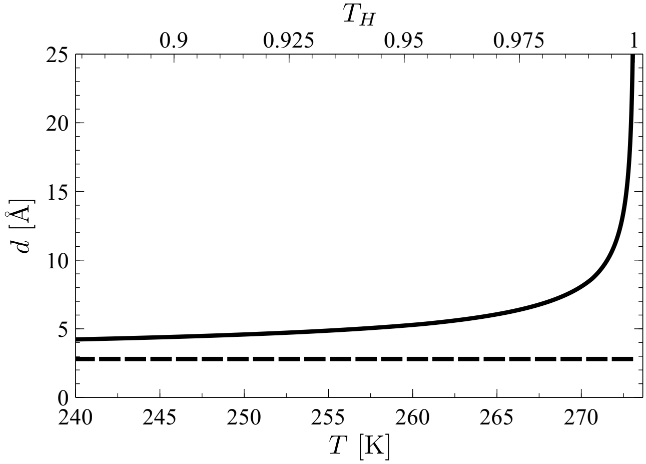

Figure 2.1: Calculation of the quasi-liquid layer (QLL) thickness d on ice as a function of temperature T. The solid line shows the calculated d and the dashed line shows 2.8 Å, illustrating the molecular length of a water molecule.

where κ^{-1} is the Debye length, ϵ, is the dielectric constant, ϵ_0, is the permittivity of free space, and q_s is the surface charge. Wettlaufer [31] proposed that μ_D can be expressed as the ratio between a fraction ξ of the kinetic energy at impact, E_i, and the premelted mass $\rho_l \pi a_d^2 d$, i.e.,

$$\mu_D = \frac{\xi E_i}{\rho_l \pi a_d^2 d}, \tag{2.14}$$

where a_d is the maximum contact radius. The damage term is used to describe how microscopic and mesoscopic changes lead to the deterioration of macroscopic material properties. With these expressions for the chemical potentials, the displacement $\Delta\mu(T, P)$ (Eq. (2.5)) can be expressed in general as

$$\frac{q_m}{T_m}(T_m - T) + \frac{\rho_l - \rho_s}{\rho_l \rho_s}(P_m - P) = \mu_{vdw} + \mu_s + \mu_D + \mu_e, \tag{2.15}$$

where

$$\mu_{vdw} = -\frac{A_H}{6\pi\rho_l d^3}. \tag{2.16}$$

In the same way as for Eq. (2.8), this generalized equation can be used for ice when predicting the thickness d of the QLL, when there is damage at the interface, when adding salt, or when an electrostatic potential is present on the surface.

2.1.2 Snow Morphology

Snowfall typically starts with ice crystals that are formed in the troposphere by nucleation of liquid droplets. The droplets in the troposphere are so small that their curvature causes a depression of the ice nucleation temperature, and homogeneous nucleation is therefore an unlikely process which may occur at temperatures as low as −38 °C. Instead, it is more common that nucleation occurs when these droplets collide with nanometer-sized aerosol particles, which triggers heterogeneous nucleation at an elevated temperature. This nucleation can occur for temperatures from 0 °C to −37 °C depending on the particle properties [32]. Once an ice crystal has formed, it grows through mass transfer and deposition where surrounding water vapor transforms into solid ice on the crystal. This occurs while the crystal falls from the sky, and the resulting shape of the crystal is affected by the local humidity which is surrounding the crystal, and the air temperature, both which will change as the crystal is falling towards the ground. The resulting crystal is commonly referred to as a snowflake, and due to variations in weather, these snowflakes can take many different forms such as needles, columns, prisms, or dendrites [33].

A snowflake has a high specific surface area, and the T_H for seasonal snow covers is typically close to 100%. Since the material is so close to its melting temperature, it can easily change phase from solid to liquid or from solid to vapor (sublimation). The process to change phase is driven by the minimization of the energy state and is sensitive to humidity, temperature gradients, pressure, and curvature of the ice surface [17]. A snowflake which has settled on the ground will therefore be thermodynamically very active and can rapidly begin to change size and shape. This process is called snow metamorphism [17]. For snow below its melting temperature, snow metamorphism is commonly divided into two categories: equilibrium metamorphism and kinetic metamorphism. Kinetic metamorphism occurs at a fast rate of growth where a temperature gradient and humidity cause deposition, and the crystal takes a hexagonal form. The equilibrium form, in contrast, occurs at slower growth rates, where individual ice particles are changing under isothermal conditions. For a solid ice particle under these conditions, the lowest energy configuration is a sphere and therefore the thermodynamics of the material are driving ice particles present in a snow cover to change shape towards spherical ice particles [34]. These particles can either grow or shrink in size [17] and the duration of the snow metamorphism will affect the particle size distribution expected for ice particles in a snow cover [35]. For example, particles with a radius of 1 μm have such a high curvature that they are expected to disappear (by sublimation) within 1 hour, while particles with a radius of 100 μm are expected to disappear in 1 year [36]. Typically, it is expected that the ice particles in a snow cover consist of round ice particles in the size range from a few hundred microns up to a few millimeters in diameter [34]. Langlois et al. [37] studied the particle size distribution of the seasonal snow cover in northern Canada and found that most round particles were a few hundred microns to one millimeter in size with an average diameter of 700 μm. Abrahamsson et al. [11] performed an in-field study on road snow and measured similar sizes for round ice particles on the ground. The authors also studied the particles adhering to the rear of a car that had been driven on a snow-covered road, and they measured that these particles, were on average, significantly smaller than the average size observed on the ground.

2.1.3 Sintering of Ice

Sintering is a thermal process where the compactness of a material is increasing over time. Sintering causes the strength of the bonds between particles in contact to grow. This process is common to observe for various crystalline materials, for example many different metals and ceramics [38]. The sintering of ice is a commonly observed phenomenon, where ice particles in contact with each other will increase bond strength over time [34, 39]. This phenomenon is closely connected to snow metamorphism, which means that particles will not only change shape and size over time but the bonds between the particles will also change over time. The sintering bond between two particles forms as a grain boundary groove geometry, where grooves on the surface grow close to the grain boundaries. This was first shown by Colbeck [39] and before this, it was incorrectly believed that the geometry could be described as a concave bond similar to how a liquid bridge is formed between particles. This bond formation is contact time dependent, and the speed of growth is temperature dependent [39]. A general regime map for a sintering material has been presented by Li et al. [40], which describes different contact regimes. In their work, the initial phase of sintering for short contact times was found to be dominated by adhesive-elastic interactions that can be described by the Johnson, Kendall, and Roberts (JKR) model, while longer contact times were dominated by other contact regimes, such as a viscoelastic contact and a viscous flow regime (see Fig. 8 in Li et al. [40] for more details).

2.1.4 Energy Dissipation for Ice Particle Collisions

The coefficient of restitution e_n is a measure of the energy loss for a particle colliding with another particle or a wall and is defined as

$$e_n = \frac{V_r}{V_i}, \tag{2.17}$$

where V_r is the rebound velocity, and V_i is the impact velocity. The subscript n refers to a collision in normal direction, and similarly e_t is referred to the coefficient of restitution in tangential direction. Multiple experimental studies have been conducted measuring e_n for ice particles, the most comprehensive study was done by Higa et al. [41, 42] where ice particle collisions with massive ice walls were studied at different temperatures regarding different particle sizes. The particles which were studied had diameters from 0.14 to 3.6 cm, and it was concluded that for V_i above a certain threshold velocity V_c, the energy dissipation starts to drastically increase for increasing V_i. Based on the results, an empirical model for e_n was proposed;

$$e_n = \begin{cases} e_{qe}\left(\frac{V_i}{V_c}\right)^{-\ln(V_i/V_c)} & V_i \geq V_c, \\ e_{qe} & V_i < V_c, \end{cases} \tag{2.18}$$

where e_{qe} is the quasi-static coefficient of restitution independent on V_i. The study reported that V_c is dependent on R, and an empirical equation has been proposed by Higa et al. [42], which is simplified in this thesis and is expressed as

$$V_c = K_1 \exp\left(\frac{K_2}{k_b T}\right) R^{-0.5}, \tag{2.19}$$

valid for $T > 229$ K, where $K_1 = 7.055 \cdot 10^{-7}$ and $K_2 = 0.25$ are the resulting constants based on the best fit of the experimental measurements in Higa et al. [42]. The authors of Higa et al. [42] accredited the change of e_n with increasing V_i to cracking and fragmentation of the particles at collision.

An alternative theory was proposed by Wettlaufer [31], where he suggested that the damage and distortion caused by the collision, increase the premelting of ice. Dash et al [26] and Wettlaufer [31] have previously shown that μ_D becomes dominant in Eq. (2.15) for low values of damage. Wettlaufer [31] derived an expression for the premelted thickness d for a collision as

$$d = \frac{\xi E_i}{\pi \rho_l a_d^2} \frac{1}{\left(\frac{q_m}{T_m}(T_m - T) + \frac{\rho_l - \rho_s}{\rho_l \rho_s}(P_m - P) \right)}, \tag{2.20}$$

and proposed a collisional fusion model for collisions between ice particles, which predicts when two particles colliding will fuse together.

2.2 Particle Dynamics and Interactions

Snow adhesion and the associated sensor contamination involve ice particles that collide with other objects, for example other particles or walls. During these collisions the particles interact with the colliding object. These interactions define whether a particle will stick or bounce, and specifically depend on the intermolecular attraction as well as the elasticity of the material. This chapter summarizes concepts for particle-particle and particle-wall interactions relevant to particle collisions. Static interactions that depend on intermolecular forces are combined with dynamic interactions which depend on the collision process.

It is worth emphasizing that this thesis focuses on macroscopic particles i.e., particles that are at least micrometer-sized. Some of the continuity and macroscopic assumptions that are made do not apply for nanometer-sized particles.

2.2.1 Intermolecular Interaction

Intermolecular forces are common sources of adhesion and occur due to electrodynamic interactions between molecules and/or atoms. These forces are most often attractive, but can be repulsive. There are three main intermolecular forces relevant for the adhesive interactions which are considered in this thesis: dipole-dipole (Keesom), dipole-induced dipole (Debye), and induced dipole-induced dipole (London/Dispersion) [28]. These forces are collectively often called the van der Waals forces. The terminology is however not consistently used in literature and sometimes only the dispersion forces are defined as the van der Waals forces. Hydrogen bond is a special case of dipole-dipole interaction that is stronger than the usual dipole-dipole interaction [28], and because of this it is sometimes excluded from the van der Waals forces. No distinction is made between the different types of forces in this thesis and all these intermolecular forces will be referred to as van der Waals forces.

Van der Waals forces are long-range in the sense that they act longer than an atomic bond or chemical bond [43]. However, for a micrometer-sized particle their range is so short that they are considered to only be active when particles are in contact. The effects of van der Waals forces grow as objects get smaller since the ratio between surface area and the mass of a particle grows with decreasing size. The interaction energy per unit area $G(l)$ between two flat plates of different materials in a medium is calculated as [28]

$$G(l) = \frac{A_H}{12\pi l^2}, \tag{2.21}$$

where l is the separation distance, and A_H is the effective Hamaker coefficient for the two materials in the medium. For applications with air as a medium, it is often assumed that this is similar to no medium at all (vacuum). The A_H can be determined experimentally but can also be calculated using the dielectric functions of the materials [44]. The adhesive force per unit area $F(l)$ for two rigid spheres can be estimated using the Derjaguin approximation as [28]

$$F(l) = 2\pi R^* G(l), \tag{2.22}$$

where

$$R^* = \frac{R_1 R_2}{R_1 + R_2}, \tag{2.23}$$

is the effective radius of the contact, and R_1 and R_2 are the radii for the two objects in contact. This thesis will often address the case when a particle is interacting with a flat wall. For this case $R^* = R_1$ since $R_2 = \infty$.

2.2.2 Adhesive-Elastic Contacts

The force in Eq. (2.22) is valid for completely rigid particles. However, real particles are never completely rigid, and they deform elastically upon contact [28]. This deformation can occur due to externally applied forces as well as intermolecular forces that either push or pull the contact. A theory that predicts this elastic deformation due to intermolecular forces is the JKR model, which is an extension of the Hertz contact theory. The JKR model was formulated by Johnson, Kendall, and Roberts [45] and is today a basis for modern theories of how to model adhesive contacts [28]. While the Hertz model predicts a linear relation between normal contact force, F_n and central displacement δ, the JKR model predicts a nonlinear relationship. δ is the difference between the undeformed and deformed radius of the particle in contact. In this model, F_n can be both attractive and repulsive, while it is always repulsive in the Hertz model. The pull-off force F_c in the JKR model, which is the force needed to detach a particle in contact, is obtained as

$$F_c = \frac{3}{2}\pi R^* W, \tag{2.24}$$

where W is the work of adhesion, the amount of work required to separate two flat surfaces from contact to infinity. W can be estimated using Eq. (2.21) for a fixed distance upon contact $l = z_0$ so that $W = G(z_0)$, however, this will then be sensitive to the choice of z_0. The dielectric functions of the materials are not always known such that A_H can be calculated. Another way to calculate W is by usage of surface energies [28], for two objects with the same material W is simply

$$W_{11} = 2\gamma_1. \tag{2.25}$$

Rules regarding how to combine surface energies are typically applied for dissimilar materials. Fowkes [46] composed surface energies into dispersive and a-scalar contributions (combined contribution from the polar interactions: dipole, induced and hydrogen bonding [47]) as

$$\gamma = \gamma^d + \gamma^a, \tag{2.26}$$

where W can then be approximated as [47]

$$W_{12} = 2\Big(\sqrt{\gamma_1^d\gamma_2^d} + \sqrt{\gamma_1^a\gamma_2^a}\Big). \tag{2.27}$$

However, when dispersion forces are responsible for most of the interaction, W_{12} can be calculated as [28]

$$W_{12} = 2\sqrt{\gamma_1^d\gamma_2^d}. \tag{2.28}$$

As shown by Chokshi et al. [48], the JKR model can be written in a dimensionless form as

$$\frac{F_n}{F_c} = 4\Big(\frac{a}{a_0}\Big)^3 - 4\Big(\frac{a}{a_0}\Big)^{\frac{3}{2}}, \tag{2.29}$$

and

$$\frac{\delta}{\delta_c} = 6^{\frac{1}{3}}\left(2\left(\frac{a}{a_0}\right)^2 - \frac{4}{3}\left(\frac{a}{a_0}\right)^{\frac{1}{2}}\right), \tag{2.30}$$

where a is the contact radius, a_0 is the contact radius at equilibrium, and δ_c is the critical displacement, which is the separation distance needed for the contact to break. These variables are defined as

$$\delta_c = \frac{a_0^2}{2(6)^{\frac{1}{3}}R^*}, \tag{2.31}$$

and

$$a_0 = \left(\frac{9\pi W R^{*2}}{2E^*}\right)^{\frac{1}{3}}. \tag{2.32}$$

The effective Young modulus E^* is defined as

$$\frac{1}{E^*} = \frac{1-\nu_1^2}{E_1} + \frac{1-\nu_2^2}{E_2}, \tag{2.33}$$

where E_k is the Young modulus, and ν_k is the Poisson's ratio of material k.

Eq. (2.29) and Eq. (2.30) give F_n as an implicit function of δ that can only be solved numerically. Fig. 2.2 shows F_n/F_c as a function of δ/δ_c. Four points of interest are highlighted in the figure: A, B, C, and D, which are ordered for a collision in the sequence of events. Fig. 2.3 shows exaggerated illustrations of the particle deformations at these four points for a particle upon collision with a wall. A is the initial contact point when $\delta = 0$, and the model then predicts an attractive contact force ($F_n < 0$). The particle therefore accelerates towards the wall. Point B is the equilibrium point where $F_n = 0$ and $a = a_0$, and after this point, the particle will experience a repulsive contact force ($F_n > 0$) and subsequently decelerate. This will occur up to point C, which is the maximum compression point, where the velocity of the particle will be zero and the particle will start to rebound. The particle will then rebound and accelerate from C to B and then decelerate again until point A. If there is only energy dissipation caused by the adhesive-elastic interaction, there will so far be no loss of energy for the particle since the force path going from $A \rightarrow B \rightarrow C$ is the same as going from $C \rightarrow B \rightarrow A$. After this, the JKR model predicts a necking stage of the contact, i.e. even though δ is negative, there is still a contact due to a deformed contact neck and subsequently an attractive contact force ($F_n < 0$) up to point D, which is the point of critical displacement when $\delta = -\delta_c$. This extra force path from A to D causes a loss of energy in the collision which is equal to the shaded area in Fig. 2.2.

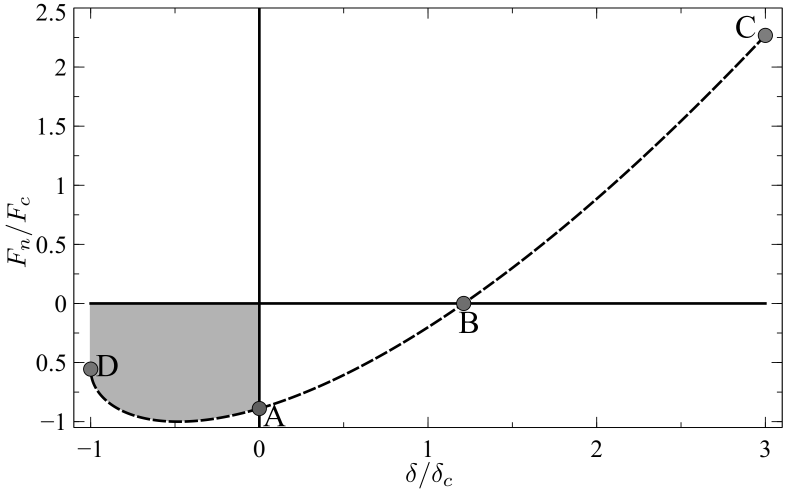

Figure 2.2: Contact force F_n/F_c for the JKR model as a function of central displacement δ/δ_c, where both quantities are plotted in dimensionless form. Notation shows four points of interest: A - Initial contact point, B - Equilibrium point, C - Maximum compression point, and D - Critical tear-off point.

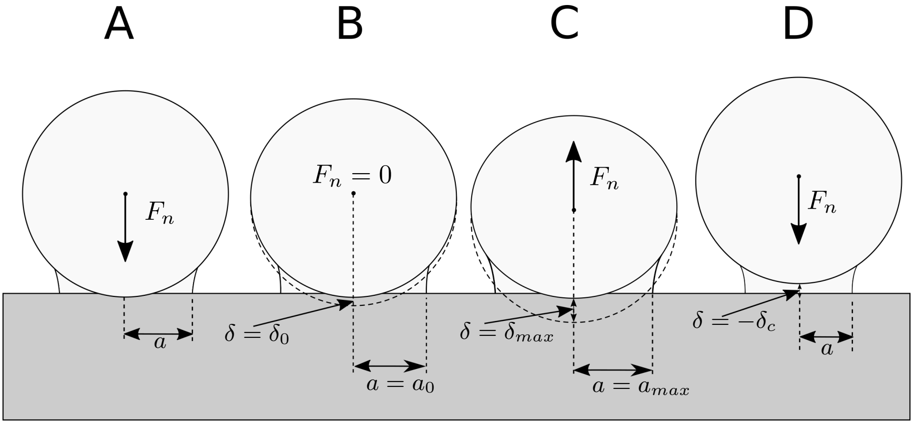

Figure 2.3: Illustration of different points of interest during a particle-wall collision: A - Initial contact point, B - Equilibrium point, C - Maximum compression point, and D - Critical tear-off point.

While the JKR theory models the adhesive-elastic interactions in the normal direction for collisions, particles can also move in tangential direction, where tangential interactions can take place. Tangential interactions are especially important for oblique impacts but can also be a major source of energy loss when agglomerates impact on a massive wall in normal direction [49]. If tangential forces are present in the interaction between particles or a particle and a wall, they can cause particles to roll or slide. This will depend on which resistance is the lowest, and the particle will then either move at a certain tangential velocity V_t or rotate with an angular velocity Ω. The particle and the contact will then deform. This is illustrated in Fig. 2.4, where the deformed adhesive contact bond is exaggerated to make the illustration clearer.

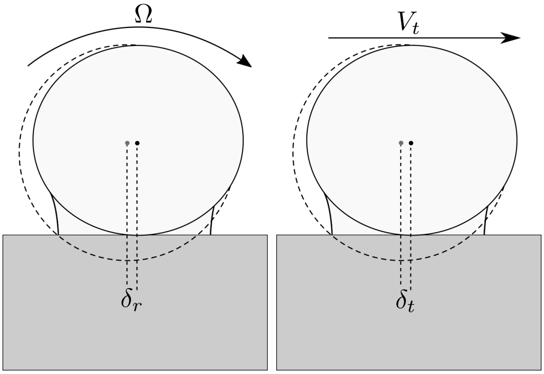

(a) Rolling (b) Sliding

Figure 2.4: Adhesive-elastic tangential particle interactions with a wall.

A simplified approach to model the resistance of adhesive particles to slide was proposed by Thornton [50], where the sliding force F_t is related to F_n, F_c, and the friction coefficient f_t as

$$F_t = f_t|F_n + 2F_c|. \tag{2.34}$$

Theoretically, however, this will only apply to rigid particles and a resistance force lower than F_t can cause elastic deformation that stores energy, that can later be released. f_t can be viewed as a material property, but it can also be increased to model the surface roughness of a particle. Sliding is rarely seen for adhesive particles [51], and modeling of this resistance is mainly done to avoid sliding, so the particles instead roll, for example, when performing particle simulations.

Multiple ways to model the adhesive rolling resistance of particles have been proposed in previous studies. A comprehensive model based on the asymmetric pressure distribution at the contact point has been proposed by Dominik and Tielens [52]. This model assumes perfect spherical particles where the critical torque for irreversible adhesive rolling is obtained as

$$M_a = 4F_c\left(\frac{a}{a_0}\right)^{3/2}\delta_{r,c}, \tag{2.35}$$

where $\delta_{r,c}$ is the critical rolling distance. Krijt et al. [53] showed that $\delta_{r,c}$ can be expressed in terms of a_0 and variable they called the adhesion hysteresis for rolling $\Delta\gamma/\gamma$, as

$$\delta_{r,c} = \frac{a_0}{12}\frac{\Delta\gamma}{\gamma}. \tag{2.36}$$

In this model, $\frac{\Delta\gamma}{\gamma}$ is a material parameter that can be obtained based on experimental data.

2.2.3 Plastic Dissipation

Apart from losses due to intermolecular forces, many other interactions can cause an inelastic collision and thereby cause particles to adhere to a surface. An example of that is plastic dissipation. Thornton and Ning [54] have proposed an extension of the JKR model with the plastic deformation of particles. The theory is that plastic deformation occurs in the contact, given that a limiting contact pressure p_y has been reached. The deformation causes a loss in kinetic energy for a particle, and e_n caused by plastic dissipation for a particle colliding with a massive wall has been derived by Thornton and Ning [54] as

$$e_n = 1.324\Big(\frac{p_y^5}{E^{*4}\rho_p}\Big)^{1/8} V_i^{-1/4}, \tag{2.37}$$

where ρ_p is the particle density.

2.2.4 Forces due to a Liquid Layer

The forces in a particle-particle or particle-wall contact can drastically change when a liquid layer is present in the contact, where both viscous as well as capillary forces can be present [28]. A static contact has two main contributions to the capillary forces: the Laplace pressure contribution and the contribution from the adhesive force inside the liquid annulus. The sum of these forces is [28]

$$F = \frac{4\pi R^* \gamma_{lv}\cos(\theta)}{1 + x/d} + 4\pi R^* \gamma_{sv}, \tag{2.38}$$

where θ is the contact angle. The first term in this sum is the Laplace pressure contribution, and the second term is the adhesive force inside the liquid annulus.

For a dynamic contact, when a particle collides with another particle or a wall, a viscous damping force F_v can be present which is caused by the viscosity μ_f of the liquid. The magnitude of this force is velocity dependent. Matthewson [55] has shown based on Reynolds lubrication theory, that for a particle colliding with a wall, F_v can be related to the particle velocity V as

$$F_v = 6\pi\mu_f R^2 V h(x), \tag{2.39}$$

where $h(x)$ is a function of the separation distance x between the particle and the wall. For an infinite wetted wall, Chan and Horn [56] have shown that

$$h(x) = 1/x, \tag{2.40}$$

which agrees well with their experimental findings, except for very thin layers or small separation distances. This equation diverges when $x \to 0$ and F_v is often limited for $x \leq \varepsilon$, where ε is a certain length scale, often taken as the particle roughness [57].

$h(x)$ is more complex when the particle is wetted and the wall is dry, since it will then depend on the meniscus geometry. For this scenario, Matthewson [55] derived that

$$h(x) = \left(1 - \frac{x}{x + a_w^2/(2R)}\right)^2 \frac{1}{x}, \tag{2.41}$$

where a_w is the wetted radius of contact and Eq. (2.41) reduces to Eq. (2.40) for $a_w \to \infty$. To estimate the associated energy loss E_v for a particle colliding with a wall, F_v can be integrated over the collision path as

$$E_v = \oint F_v dx. \tag{2.42}$$

The resulting energy loss E_v for $h(x)$ using Eq. (2.40) with a limit when $x \leq \varepsilon$ has been estimated by Sutkar et al. [57] to be

$$E_v = \frac{3}{2}\pi\mu_f R^2 V_i \ln(\frac{d}{\varepsilon}). \tag{2.43}$$

To the best of our knowledge no similar integration result has been published for $h(x)$ using Eq. (2.41).

2.3 Computational Fluid Dynamics

When a vehicle is driven on a snow-covered road, the external aerodynamics of the vehicle will have a central role for the transportation of ice particles to surfaces. The aerodynamics can both affect where particles will collide with surfaces and the collisional velocities. Computational Fluid Dynamics CFD, is a sub-field in fluid mechanics where physical phenomena involving fluids are modeled using mathematical models. In this thesis CFD is used to simulate the multiphase flow when the turbulent fluid is air and solid particles are dispersed in the fluid, a type of flow often called a particle-laden flow.

2.3.1 Aerodynamics and Turbulence Modeling

The level of turbulence present for a fluid flow can be quantified by the Reynolds number Re, which is the ratio of inertial forces to viscous forces

$$Re = \frac{\rho_f u L}{\mu_f} = \frac{uL}{\nu_f}, \tag{2.44}$$

where L is a characteristic length scale, ν_f is the kinematic viscosity of the fluid, and u is a characteristic velocity. For high enough values of Re the flow is fully turbulent and the smallest turbulent scales will decrease with increasing Re. For vehicle aerodynamics, which is the relevant fluid flow for this thesis, the flow is expected to be fully turbulent. Compressibility effects on the flow is expected to arise for high velocities exceeding 30% of the speed of sound (≈ 370 km/h), which is significantly higher than what is considered as relevant driving speeds. Air will therefore be modeled as an in-compressible fluid in this thesis. The velocity vector $\mathbf{U}$ and fluid pressure p of the flow will then follow the in-compressible Navier-Stokes equations which are defined by the continuity equation

$$\nabla \cdot \mathbf{U} = 0, \tag{2.45}$$

and the momentum equations:

$$\rho_f \left(\frac{\partial \mathbf{U}}{\partial t} + (\mathbf{U} \cdot \nabla \mathbf{U}) \right) = -\nabla p + \mu_f \nabla^2 \mathbf{U} + \rho_f g, \tag{2.46}$$

where g is the gravitational acceleration. A simulation that solves these equations is called a Direct Numerical Simulation (DNS), unfortunately the equations are so non-linear that they are, in practice only possible to solve for simple flows. To solve more industrially relevant problems, turbulence modeling is needed where the velocity components and pressure are decomposed into resolved and unresolved (modeled) turbulence scales. The decomposition can be done both in space and time. For decomposition in time, the variable of interest x is decomposed into an averaged component $\langle x \rangle$ and a time-fluctuating component x', i.e.

$$x = \langle x \rangle + x'. \tag{2.47}$$

The Reynolds-averaged Navier–Stokes equations (RANS) are obtained when inserting this decomposition in Eq. (2.46) and time averaging the equations. $\langle x \rangle$ can be solved directly in RANS but terms arising from x' when performing the time averaging needs to be modeled and the model used is called a RANS model. For decomposition in space, a variable x is decomposed into a spatial resolved component $\bar{x}$ and a filtered sub grid scale (SGS) x'', i.e.

$$x = \bar{x} + x''. \tag{2.48}$$

Inserting this decomposition in Eq. (2.46) and volume averaging the equations, it can be shown that $\bar{x}$ can be solved directly while terms arising from x'' have to be modeled (using a SGS model). This type of decomposition is referred to as a Large Eddy Simulation (LES). Solving a flow with RANS models is relatively cheap in terms of computational cost and has historically been used for many industrial applications with complex flow problems, however, they also come with reduced accuracy and the results will depend on the RANS model that is used. LES is, on the other hand, the standard in many academic fields due to its higher accuracy, it is an ideal method when resolving turbulent structures, for example behind bluff bodies [58]. The drawback with LES is the associated computational cost when resolving turbulent boundary layers in near wall regions, where the requirements in computational cost for most industrial applications are so large that LES cannot be realistically used. A way to avoid this challenge is to use hybrid LES-RANS models where the decomposition is employed both in time and space. With this approach, different spatial and time scales can be resolved depending on the region. The aim with using a hybrid LES-RANS approach is often to resolve large free stream structures while modeling turbulence in the boundary layer. Detached-Eddy-Simulations (DES) is a type of hybrid LES-RANS models where LES is combined with unsteady RANS and the switch of decomposition is done depending on a calculated turbulent length scale. The chosen RANS model is then also used as a SGS model for the LES. There are multiple versions of DES, and the formulation of the model will depend on the chosen RANS model. Shur et al. [59] proposed the Improved Delayed Detached Eddy Simulation (IDDES) with $k-\omega$ SST turbulence model, which has been employed in various applications [7, 60–62] and has shown improvements compared to RANS [63] when validated with experimental data. The reader is referred to Shur et al. [59] for a detailed explanation of the IDDES $k-\omega$ SST model and to Davidson [58] for a comprehensive summary of different turbulence models.

2.3.2 Grid Resolution

When simulating the turbulence models presented in Section 2.3.1 the simulation domain needs to be discretized and this is usually referred to as a mesh or a computational grid. The user generally must choose a resolution in order to determine how well resolved the fluid flow will be, however, how the turbulence is resolved is not in general known a priori, and therefore the resolution needs to be evaluated afterwards. The grid resolution when using hybrid LES-RANS models such as the IDDES $k-\omega$ SST model can be evaluated by looking at the near-wall resolution as well as the wake-flow resolution. For near-wall requirements a common criterion is that the resolution in normal direction should satisfy

$$y+ = \frac{u_\tau y}{\nu_f} < 1, \tag{2.49}$$

where u_τ is the friction velocity at the wall and y is the distance from the wall. For LES there are also guidelines for the near-wall resolution in spanwise and streamwise directions, where further details about such guidelines can be found in Davidson [58]. However, as pointed out by Ashton and Revell [64] there are not as well defined resolution requirements for hybrid LES-RANS models such as the IDDES $k-\omega$ SST model, and the solution in the near-wall region will, for this model, be dominated by RANS. The grid resolution for a wake-flow can be evaluated using the ratio between resolved k_{res} and total turbulent kinetic energy,

$$M = \frac{k_{res}}{k_{tot}} = \frac{k_{res}}{k_{res} + k_{mod}}, \tag{2.50}$$

where k_{mod} is the modeled turbulent kinetic energy. This ratio can be used as an indication where the model is resolving turbulent structures and a common criterion used for well resolved LES is that $M \geq 80\%$, which origins from an example criterion mentioned by Pope [65]. Davidson [66] showed that M can be close to unity also for simulations that are not well-resolved. Instead he argued that two-point correlation analysis is useful to evaluate grid resolution in a simulation. The idea is that neighboring grid points should be correlated for the turbulence to be well resolved. This analysis is made by sampling velocity components U_j (where j can be in the direction X, Y or Z) over time and then calculate the two-point correlation between the cells of interest; X_A and all cells individually after this cell at a certain direction (for example X,Y or Z axis if the grid is aligned to these axes). The goal with the analysis is to count the correlated number of cells N_{D_i,U_j}, along a direction D_i, where $C_{U_j}(X_A, X_B) >= C_c$ for a chosen threshold C_c.

The normalized (Pearson's) correlation coefficient between the two-points (X_A and X_B) for the velocity U_j is defined as,

$$C_{U_j}(X_A, X_B) = \frac{\overline{U_j'(X_A)U_j'(X_B)}}{\sqrt{\overline{\left(U_j'(X_A)\right)^2} \cdot \overline{\left(U_j'(X_B)\right)^2}}}. \tag{2.51}$$

An example of the analysis for one cell is depicted in Fig. 2.5, where the $C_{U_j}(X_A, X_B)$ has been plotted as a function of the number of cells between X_A and X_B, for a fixed X_A and changing X_B. In this example $C_c = 0.1$, was used which yields $N_{D_x,U_x} = 30$, which then reflects how well the grid resolution in X direction is in this cell for the velocity U_x. To look at this measure for a given D_i, for all U_j, we define the minimum number of correlated cells in direction D_i for all velocities as

$$N_{D_i} = \min\Big(N_{D_i,U_x}, N_{D_i,U_y}, N_{D_i,U_z}\Big). \tag{2.52}$$

This type of analysis was recently used by Törnell [62] to assert the grid resolution for the aerodynamics around two trucks driving in close proximity by performing the analysis as shown in Fig. 2.5, for each cell in a plane and plotting N_{D_i,U_x} for all the cells.

Davidson [66] proposed that it is up to the researcher or engineer to decide how many cells are necessary, which can depend on application, but suggested also that a minimum of $N_{D_i} = 8$ is recommended for a coarse LES and $N_{D_i} = 16$ should be sufficient for a well resolved LES.

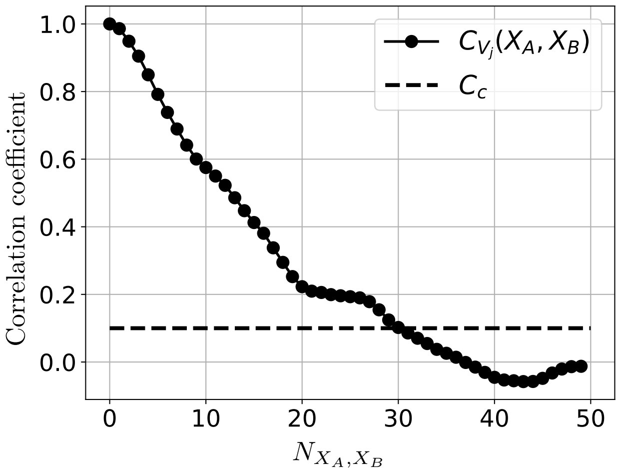

Figure 2.5: Two-point correlation $C_{U_x}(X_A, X_B)$ as a function of the number of cells between the points X_A and X_B for fixed X_A and varied X_B along the X-axis. Dashed line shows example of threshold $C_c = 0.1$.

2.3.3 Particle Concentration and Momentum Coupling

The concentration of particles can affect the overall properties of the particle-air mixture. Depending on how concentrated particles are when present in an air flow, the properties of the flow may change. A dense flow is defined as a flow with so many particles such that the likelihood for particle-particle collisions is large, which then affects the particle transportation. A dilute flow is the opposite, where particles are so dispersed that the particle motions will only be affected by the fluid forces, and particle-particle interactions can be neglected. According to Crowe et al. [67] a flow is to be considered dilute if

$$\frac{\tau_p}{\tau_C} < 1, \tag{2.53}$$

where τ_p is the particle response time and τ_C is the time between collisions. Assuming that a mean velocity fluctuation U' is acting on a particle, for a given ratio $\frac{\tau_p}{\tau_C}$, the particle diameter for this given ratio can be calculated as [67]

$$D_p = \frac{3\sqrt{\pi}\mu_f}{4\rho_p U' \alpha_d}\frac{\tau_p}{\tau_C}, \tag{2.54}$$

where α_p is the volume fraction of particles. Particles present in a fluid flow will be affected by the mean velocity and fluctuations of the flow. Generally, the presence of the particles will also affect the fluid, for example by momentum change of the flow. If both of these interactions are present and important for the physical problem the flow is called two-way coupled. If particles are affected by the air flow but the particle effects on the air is negligible the flow is called one-way coupled. When the particles are small and the flow can be considered as dilute, it is common to regard the flow as one-way coupled [68].

2.3.4 Particles in Turbulence

When driving a vehicle on a snow-covered road the air flow in proximity to the vehicle is turbulent. When an ice particle is transported through this air, the turbulence air cause forces on the particles and affect the trajectory as well as the resulting collisional velocity with a potential vehicle wall. This interaction between particles and a turbulent air flow is therefore important for the present topic. To classify the transportation of particles in a turbulent flow it is useful to use dimensionless numbers. The local turbulence surrounding the particle can be quantified by the particle Reynolds number

$$Re_p = \frac{\rho_f D_p |\mathbf{U_s}|}{\mu_f}, \tag{2.55}$$

where $|\mathbf{U_s}|$ is the magnitude of the particle slip velocity. When modeling particle transportation in a turbulent flow the local detailed turbulence is often not resolved and instead Re_p is used as a quantification of this local turbulence. For $Re_p << 1$ the flow is called a Stokes flow or creeping flow, and analytical solutions predicting the flow field can often be derived. How the particle is responding to a turbulent field can be quantified by the Stokes number

$$St = \frac{\tau_p}{\tau_f}, \tag{2.56}$$

where τ_f is the characteristic time of the fluid flow. The Stokes number is an important parameter since it quantifies the ability of a particle to follow turbulent fluctuations. If $St << 1$, particles respond rapidly to changes in the fluid flow and can therefore be able to follow complex paths such as rotations and sudden directional changes. On the other hand if $St >> 1$ particles generally do not react to fluid flow changes and move in the air flow independent of local turbulent fluctuations. For a Stokes flow it can be shown that [69]

$$\tau_p = \frac{\rho_p D_p^2}{18\mu_f}, \tag{2.57}$$

which highlights that τ_p is sensitive to the particle size. Generally for non-Stokesian flow, the expression for τ_p takes an integral form but the particle size dependency is similar and small particles will still tend to follow fluid motion more than large particles.

For a solid particle present in turbulent air flow, various forces acting on the particle can arise. For heavy particles $(\rho_p >> \rho_f)$ the drag force is likely to be the most dominant force acting on a particle. This force arises from velocity differences between the particle and the fluid. Generally the drag force $\mathbf{F_D}$, is calculated as [70]

$$\mathbf{F_D} = \frac{1}{2}\rho_f C_d A_p |\mathbf{U_s}| \mathbf{U_s}, \tag{2.58}$$

where C_d is the drag coefficient. This coefficient is not a constant and is expected to depend both on Re_p as well as the shape of the particles. Analytical solutions are generally only possible to obtain for small values of Re_p and instead various experimental correlations have been obtained. Two of the most used correlations are the Schiller-Naumann correlation [71] and the Haider-Levenspiel correlation [72]. While the Schiller-Naumann correlation only depends on Re_p, the Haider-Levenspiel correlation is also a function of the particle sphericity ϕ. The ϕ is defined as

$$\phi = \frac{s}{S}, \tag{2.59}$$

where s is the surface area of a sphere with the same volume as the particle and S is the actual surface area of the particle. Fig. 2.6 shows the C_d as a function of Re_p for varying ϕ using the Haider-Levenspiel correlation [72] (see their Eq. (11)). As can be seen the significant variations for different ϕ occur for high $Re_p >> 10$.

When a particle is present near a wall, the $\mathbf{F_D}$ is expected to be anisotropic and can be divided into a wall-normal component $\mathbf{F_{D,\perp}}$ and tangential component $\mathbf{F_{D,||}}$ [70]. O'Neill [73] derived analytically for a Stokes flow that

$$C_{d,||} = f_{d,||} C_d, \tag{2.60}$$

where C_d is the free stream drag coefficient and $f_d = 1.7009$, is a correction term. The same correction term multiplied with the C_d has later also been used for higher Re_p [70]. For the $C_{d,\perp}$ a similar correction term was obtained by Maude [74] for a Stokes flow with $f_{d,\perp} = 3.39$, which means that

$$f_{d,\perp} \approx 2 f_{d,||}. \tag{2.61}$$

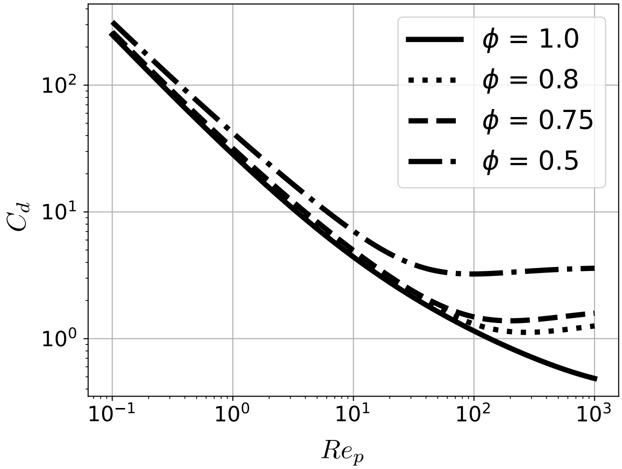

Figure 2.6: Drag coefficient C_d as a function of Re_p for varying ϕ using the Haider-Levenspiel correlation [72].

For a particle in a turbulent flow, lift forces may also arise on the particles caused by a velocity gradient acting perpendicular to the oncoming flow direction. The shear lift force $\mathbf{F_{LS}}$ is defined as

$$\mathbf{F_{LS}} = C_{LS} \frac{\rho_f \pi}{8} D_p^3 (\mathbf{U_s} \times \omega), \tag{2.62}$$

where ω is the fluid vorticity and C_{LS} is the shear lift coefficient. Similar to C_d, empirical correlations for C_{LS} are often used where a common correlation is the one by Sommerfeld [75], which is a function of the Reynolds number for the shear flow

$$Re_S = \frac{\rho_f D_p^2 |\omega|}{\mu_f}. \tag{2.63}$$

If a pressure gradient is present this can also contribute as a force

$$\mathbf{F_P} = -V_p \nabla P_f, \tag{2.64}$$

where V_p is the particle volume and ∇P_f is the pressure gradient for the fluid.

For the studied particles in this thesis it holds that $\rho_p >> \rho_f$. Other forces such as the virtual mass or buoyancy forces are therefore considered negligible. The particles relevant for this thesis are also substantially larger than one micron, which means that diffusion driven by Brownian motion and rarefaction effects can also be neglected.

2.3.5 Particle Simulations

Simulations of particles, where the position of a particle is tracked over time, are usually done by solving Newton's second law of motion as

$$m_p \frac{d^2 \mathbf{U_p}}{dt^2} = \sum_{\forall i} \mathbf{F_i}. \tag{2.65}$$

In this equation, $\mathbf{U_p}$ is the particle velocity, and m_p is the mass of the particle, which is assumed constant, and the sum of all $\mathbf{F_i}$ represents all forces acting on a particle at a specific time step. Theses forces can for example be the forces mentioned in Sec. 2.3.4, or gravity, or contact forces in a collision. If a particle is also allowed to rotate, Newton's law of rotation is also solved

$$I \frac{d\mathbf{\Omega}}{dt} = \sum_{\forall i} \mathbf{M_i}, \tag{2.66}$$

where I is the particle inertia, $\mathbf{\Omega}$ is the angular velocity of the particle, and the sum of all moments $\mathbf{M_i}$ represents all moments acting on the particle. Particle-particle or particle-wall interactions can be modeled with either binary collisions, also called the hard-sphere approach, or by resolving the collision with the soft-sphere approach [69]. The soft sphere approach is commonly called the Discrete Element Method (DEM), which allows particles to overlap, and the force is then expressed as functions of this overlap. δ is equivalent to this overlap in the JKR model as defined by Eq. (2.29) and Eq. (2.30), and thus these equations can be used directly in DEM.

Chapter 3

Observations of the Snow Contamination of Cars

In this chapter, observations of the snow contamination of cars are shown to demonstrate the present research topic, where results from both in-field tests and wind tunnel experiments are shown.

3.1 In-Field Test Approach

In-field snow tests were performed on a test track where two identical variants of a Volvo XC40 Recharge were used as test objects. The two vehicles will henceforth be referred to as vehicle A and B (see Fig. 3.1). The tests were performed in winter conditions in Sweden, where a layer of snow was present on the test track. Two types of tests were performed: self-contamination tests and third-party contamination tests.

Self-contamination was tested by driving a test vehicle without any other vehicles nearby, therefore surface contamination is caused by the vehicle itself when snow is lifted up while driving. These tests were performed for driving speeds 40, 50, 60, and 70 km/h, where 25 km were driven for each driving speed. A test was performed by driving a cleaned vehicle on the test track for 25 km and the deposited snow were then documented by taking photographs of the vehicle. The self-generated cloud of snow from a vehicle was studied by driving along a segment of the test track at varying speeds. Photographs of the generated snow cloud were taken as the vehicle passed the same location, such that photographs of the cloud at different speeds could be compared to each other.

The third-party contamination was tested using both vehicles, where they were driven in close proximity to each other, such that the vehicle behind was driving in a snow cloud. These tests were mainly done for the comparison with the wind tunnel experiments, where snow was sprayed in front of the tested vehicle using a snow cannon.

When performing tests in an outdoor environment the tests are not in general repeatable since the layer of snow on the ground is constantly changing as well as the weather conditions. To manage with these challenges, the results at varying velocities were obtained during the same day when the conditions were similar. The self-contamination tests were mutually performed on both test objects such that variations caused by lack of repeatability could be detected. However, when the tests were performed no distinguishable differences were seen between the results on vehicle A and vehicle B. Results are therefore only shown for vehicle A in this chapter. The self-contamination tests were performed in a speed sequence of 40, 70, 40, 50, and 60 km/h. This was done to monitor and detect if any changes in weather conditions would affect the tests, however no such changes were observed during the testing.

(a) Vehicle A. (b) Vehicle B.

Figure 3.1: Test objects used for in-field tests.

3.2 Wind Tunnel Procedure

Wind tunnel experiments were performed in an open jet climatic wind tunnel with a nozzle cross section of 4.3 m^2 (2.5 m × 1.7 m). Air temperature was kept constant at $-15\,^{\circ}\mathrm{C}$, and the inlet velocity, U_∞, was kept constant at 70 km/h. Snow was produced using a type of snow cannon, often called a snow lancer, which is a long metal pipe equipped with small nozzles at the end. Cold water and pressurized air were mixed in these nozzles to breakup and nucleate small water droplets. The snow cannon was placed upstream in the nozzle of the tunnel and was placed in head-wind direction, such that airflow would disperse the cloud of ice particles. Fig. 3.2 shows a photograph of the snow cannon in the nozzle section of the tunnel.

The test object used (vehicle C) was the same model as for the in-field tests; a Volvo XC40 Recharge, which was placed downstream in the middle of the test section in the wind tunnel. The wheels of vehicle C did not rotate during the test. The test vehicle is shown mounted in the wind tunnel in Fig. 3.3. The results from the wind tunnel were compared to the third-party contamination test results on vehicle A. However, vehicle A and vehicle C are not identical, for example the wheels are different and small design differences exist where vehicle C was equipped with an exterior styling kit. These differences were however considered to be minor, instead deviations between the two measurements are expected to be due to difference in snow type as well as how the tests were performed. While the in-field tests included both the self-contamination as well as the third-party contamination, the wind tunnel tests only include snow coming from the front of the vehicle without any wheels rotating.

Figure 3.2: Snow cannon in wind tunnel where the cannon is placed in head-wind direction.

Figure 3.3: Test object vehicle C, used in wind tunnel experiments.

3.3 Results and Discussion

3.3.1 Self-Contamination

In the self-contamination tests, snow was predominately observed to adhere and accumulate at the rear of the vehicles, while almost no snow deposited on the front and side surfaces of the vehicles. Tests at varying speeds revealed that the amount of snow that accumulated, as well as the area of accumulation, was strongly dependent on the driving speed. Results for vehicle A when driving 25 km on the test track at speeds 40, 50, 60, and 70 km/h are shown in Fig. 3.4 and Fig. 3.5, at a rear view and an isometric rear view, respectively. The figures show that more snow accumulates at lower velocities compared to higher. The highest area of accumulation was obtained at the speed 40 km/h, while the lowest was observed for 70 km/h. These differences in snow accumulation is likely due to changes in the aerodynamic load, which can cause resuspension of particles. The aerodynamic load will increase with increasing driving speed. It is likely that resuspension of ice particles in the rear wake regions affects the accumulation of snow in these tests. To investigate this, tests where done were a vehicle was continued to be driven with increasing velocities while the vehicle was not cleaned of snow between changes in velocity. The results from these resuspension tests are shown in Appendix A, where it can be seen that snow is disappearing from the vehicle while driving at increasing driving speed. The resuspension of ice particles was further analyzed in Chapter 6 where a resuspension criterion was derived.

The generated snow cloud from a vehicle consists of individual ice particles. The results shown in Fig. 3.4-3.5 indicate in two ways how the deposition rate of snow is connected to the expected collisional velocities of ice particles. Firstly, deposition predominately occurred in the rear separation regions, where low collisional velocities are expected since the relative velocity between the fluid flow and surfaces in these regions is low. Secondly, the magnitude of the collisional velocity for the ice particles should be directly connected to the vehicle speed. The results show that decreasing speed increases the snow deposition. The collisional properties of ice particles and adhesive properties in particle-wall collisions are further analyzed in Chapter 4.

With an increase in speed, more snow is lifted by the vehicle, which forms a larger snow cloud behind the vehicle. The magnitude of the self-generated snow cloud when a vehicle is driven on a snow-covered road is depicted in Fig. 3.6, which shows photographs of the snow clouds for various driving speeds. While a speed of 30 km/h generates a barely visible snow cloud, the amount of snow deposited at this speed was significantly higher than at higher speeds, for example 70 km/h. This highlights that the snow cloud seen when driving does not necessarily correlate with the deposition rate of snow, and it is possible that smaller ice particles, which have a large tendency to stick to surfaces, simply are not visible to the naked eye.

Figure 3.4: Snow accumulation at a rear view of Vehicle A after driving for 25 km at the speeds; 40, 50, 60, and 70 km/h at $T = -8 \pm 2\,^{\circ}\mathrm{C}$.

Figure 3.5: Snow accumulation at an isometric rear view of Vehicle A after driving for 25 km at the speeds; 40, 50, 60, and 70 km/h at $T = -8 \pm 2\,^{\circ}\mathrm{C}$.

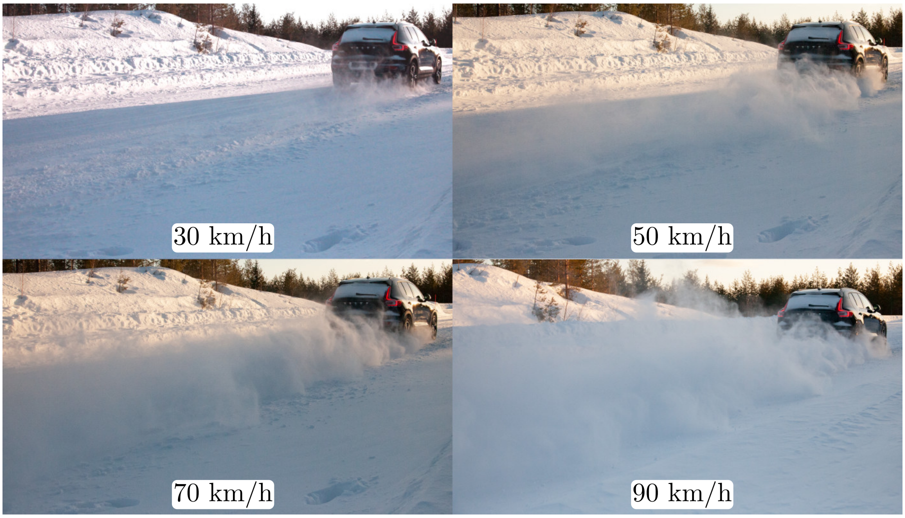

Figure 3.6: The self-generated snow cloud for the driving speeds; 30, 50, 70, and 90 km/h.

3.3.2 In-Field Tests Compared to Wind Tunnel Tests

Fig. 3.7 shows a comparison between results from the wind tunnel with the third-party contamination test procedure. The comparison is restricted to rear surfaces where an isometric rear view is shown to the left, and a rear view is shown to the right. Fig. 3.7a shows a wind tunnel measurement with machine made snow at $T = -15\,°\mathrm{C}$, where the test was performed for 30 min. Fig. 3.7b shows an in-field test using the third-party contamination test where an identical vehicle was driven in front of the test vehicle to generate a snow cloud. Interestingly, almost no snow was observed to adhere to the side or front surfaces, despite the vehicle has been driven in a snow cloud. The results obtained are similar to the self-contamination test at 70 km/h as shown in the previous section. For the wind tunnel test, however, clear snow accumulation can also be seen at the sides in Fig. 3.7a, where snow has deposited behind the A, B, and C-pillar of the vehicle. These results bring attention to deviations that can be observed between the machine made snow and the natural snow. Deviations between these types of snow are further analyzed in Chapter 5 and 6, where not only the angle of repose of machine made snow was significantly higher than natural snow, but the machine made snow also tended to deposit at regions where the natural snow did not deposit.

(a) Wind tunnel measurement of vehicle C for testing in 30 min with $U_\infty = 70$ km/h at $T = -15\,^\circ\mathrm{C}$.

(b) Third-party contamination test of Vehicle A while driving at 70 km/h for 50 km at $T = -8 \pm 2\,^\circ\mathrm{C}$.

Figure 3.7: Snow accumulation results at an isometric rear view to the left and a rear view to the right.

Chapter 4

Single Ice Particles Collisions with Surfaces

Central to the topic of this thesis is the energy dissipation when ice particles collide with massive walls or previously deposited ice particles. As summarized in Section 2.2 there are multiple sources of energy dissipation that can be present when particles collide with an object. In this chapter, a computational framework for the modeling of ice particle collisions with massive walls is summarized. A massive wall is defined such that the mass of the wall is significantly larger than the particle mass, and therefore the effective mass m^* in the collision is equal to the mass of the impacting particle m_p. It also follows that $R^* = R_p = 0.5D_p$, since the walls are modeled as completely flat. Emphasis in this chapter is towards the energy dissipation in the collisions, which is represented by the coefficient of restitution e_n, and the highest velocity of sticking V_s. Two regimes of impact will be presented; a low velocity modeling of adhesive-elastic interactions, and a high velocity modeling based on collisional melting. For the modeling at low velocity, an analytical solution was used to evaluate e_n for ice particles. For the collisional melting model, experiments of millimeter-sized ice particles were carried out to derive unknown model coefficients. Finally, a regime map combining the two modeling approaches is presented.

4.1 Modeling Collisions in the Intermolecular Regime

The JKR model is used to quantify the adhesive-elastic energy loss in ice particle collisions. The model is assumed to be relevant for capturing the main dynamics of the adhesion for low velocity collisions with ice particle contacts. The JKR model is a well-validated model for adhesive particles in general [18] and has been extensively used previously for modeling contacts between ice particles [48, 76]. The model is only modeling adhesive-elastic interactions and is considered relevant under the following assumptions:

- The ice is sufficiently cold $T \lesssim 261$ K, such that the effects of premelting can be neglected.

- The collisional velocities V_i are sufficiently low, such that the energy dissipation is dominated by the adhesive-elastic interactions.
- The ice particles are spherically shaped and adhesive effects caused by irregularities in shape can be neglected.
- The time of contact for both particle-particle contacts as well as particle-wall contact is sufficiently short, such that effects of sintering can be neglected.

Assuming that V_s is the highest velocity for a particle sticking to a wall, this velocity can be related to the stick energy E_s as

$$\frac{1}{2}m_p V_s^2 = E_s, \tag{4.1}$$

where E_s is equal to the shaded area in Fig. 2.2 and can be calculated by integrating Eq. (2.29) and Eq. (2.30) numerically as

$$\begin{aligned} E_s &= F_c\delta_c \int_D^A \frac{F_n}{F_c} d\Big(\frac{\delta}{\delta_c}\Big), \\ &= K_1 F_c \delta_c, \\ &\approx 0.4177\Big(\frac{\pi^5 W^5 D_p^4}{E^{*2}}\Big)^{1/3}, \end{aligned} \tag{4.2}$$

where $K_1 \approx 0.9355$ is an integration constant obtained through the numerical integration. An equivalent result for E_s as shown in Eq. (4.2) was previously obtained by Thornton and Ning [54] (compare with Eq. (52) in Thornton and Ning [54]). When inserting Eq. (4.2) into Eq. (4.1), it follows that

$$V_s = 2.24\sqrt{\frac{1}{\rho_p}}\left(\frac{\pi^2 W^5}{D_p^5 E^{*2}}\right)^{\frac{1}{6}}, \tag{4.3}$$

which relates to how smaller particles tend to stick more than larger particles (since $V_s \propto D_p^{-5/6}$). The coefficient of restitution based on the JKR model e_n, can be formulated using V_s as [54]

$$e_n = \sqrt{1 - \left(\frac{V_s}{\max(V_i, V_s)}\right)^2}, \tag{4.4}$$

where $e_n = 0$ means the particle is predicted to stick (when $V_i \leq V_s$).

4.2 Collisional Melting Model

The JKR model predicts that particles will stick below a certain threshold V_s, while for higher velocities the energy lost due to the intermolecular interactions is constant and quickly becomes insignificant compared to E_i. Previous experiments of ice particles by Higa et al. [42] show that for high V_i the energy dissipation drastically starts to increase for increasing V_i. Nietiadi et al. [77] simulated collisions between nanometer-sized ice particles and found that the JKR model agreed well with their simulations with respect to the contact radius a_0 for low velocity collisions, however deviations increased with increasing V_i. They accredited this deviation to increasing collisional melting at the collision. Eq. (2.18) which originates from Higa et al. [42], agrees well with the experimental data obtained in the same paper. However, the commonly used plastic dissipation model by Thornton and Ning [54] predicts $e_n \propto V_i^{-1/4}$ (Eq. (2.37)), which is a significantly weaker dependency of V_i than Eq. (2.18), which has a proportionality similar to $e_n \propto V_i^{-1}$. This is depicted in Fig. 4.1 which shows e_n as a function of V_i for Eq. (2.18) together with Eq. (2.37) and $e_n \propto V_i^{-1}$. The figure also includes measurement points extracted from Higa et al. [42] for $D_p = 8$ mm at $T = -12\,°\mathrm{C}$. The value of p_y was in this figure arbitrarily chosen to match the used V_c for Eq. (2.18). The figure illustrates that the plastic dissipation model does not capture the rapid increase in energy loss with increasing V_i for ice particles. This can be because the model does not account for melting dynamics and is generally used for low values of the T_H. Ice on the other hand, regarding the frost-free measurements in Higa et al. [42], are all at $T_H \geq 0.9$. Experiments on other materials have shown that $e_n(V_i)$ changes for high values of T_H. Hashemnia [78] showed that the e_n of steel balls colliding with a heated metal wall started to decrease as early as $T_H > 0.6$. Yildirim et al. [79] showed that the e_n of micrometer-sized metal particles stops following $e_n \propto V_i^{-1/4}$ and instead follows $e_n \propto V_i^{-1}$ at sufficiently high V_i.

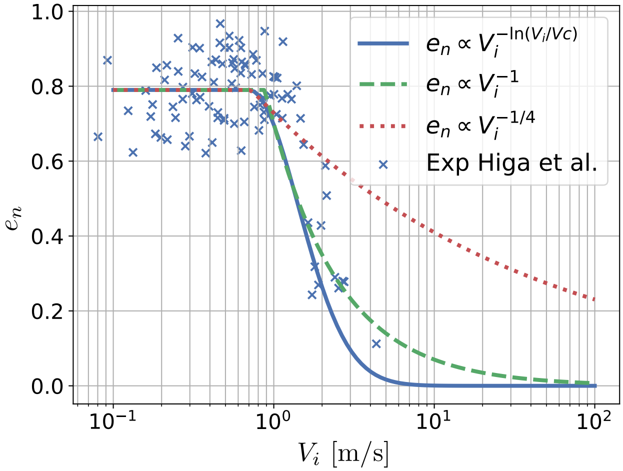

Figure 4.1: The coefficient of restitution e_n as a function of V_i using Higa et al. [42], Thornton and Ning [54] as well as $e_n \propto V_i^{-1}$. Cross markers show measurements from Higa et al. [42] for $D_p = 8$ mm at $T = 261$ K.

Wettlaufer [31] proposed that induced molecular disorder, caused by damage during collisions, generates an increased QLL, which can fuse ice particles together if the time scale for freezing of the QLL is shorter than the collision time scale. Eq. (4.2) predicts thicker QLL with increased T which should result in less fusion for increasing T, however, previous experiments imply more energy losses with increased T. It was therefore argued in Paper II that the associated energy loss can be explained by the presence of the QLL itself, instead of a fusion mechanism, specifically that the QLL causes an extra viscous loss in the collision. Based on the work by Wettlaufer [31] a simplified expression was derived for the premelted thickness caused by collisional damage for an ice particle colliding with a massive wall as

$$d = \left(\frac{16\sqrt{6}E^*}{135\pi}\right)^{2/5} \frac{\xi D_p \rho_s^{3/5} V_i^{6/5}}{2\left(\frac{\rho_l q_m}{T_m}(T_m - T) + \frac{\rho_l - \rho_s}{\rho_s}\left(P_m - \xi\left(\frac{40}{\pi^4}\rho_s V_i^2 E^{*4}\right)^{1/5}\right)\right)}. \tag{4.5}$$

Details of the derivation of this equation are shown in Appendix B. In Paper II there is unfortunately a typo where ρ_l is missing in the temperature term, however, the correct equation was used in the calculations for the results in the paper. In this equation, d is directly proportional to D_p, which means that the ratio d/D_p is independent of particle size. This equation is valid under the assumption that the contribution from μ_{vwd} (in Eq. (2.15)) is negligible compared to μ_D (Eq. (2.14)). Fig. (4.2) depicts when this is not the case by solving Eq. (2.15) using only μ_D as well as $\mu_D + \mu_{vdw}$. The figure shows d/D_p as a function of V_i where the solution is the same with or without μ_{vdw} for sufficiently high $V_i > 0.1$ m/s. For this calculation $\xi = 0.15$ was used based on the estimation in Wettlaufer [31] where they bounded $\xi \in [0.1, 0.2]$.

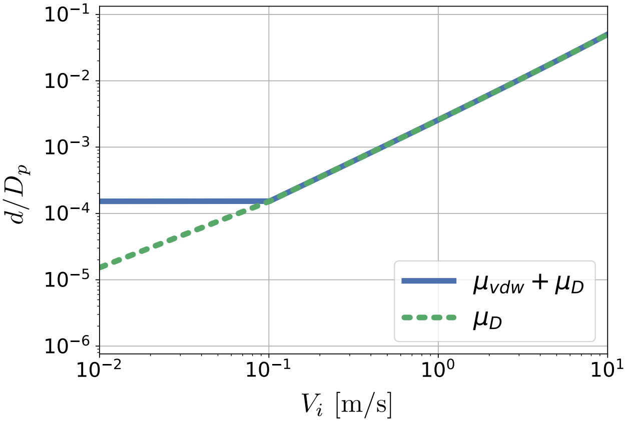

Figure 4.2: Predicted d/D_p as a function of V_i for an ice particle colliding with an ice wall at $T = 262$ K. The green dotted line shows the solution with only μ_D and the blue solid line shows the solution with $\mu_{vdw} + \mu_D$. $\xi = 0.15$ was used in the calculations and the shaded area shows the variation for $\xi = 0.15 \pm 0.05$.

Assuming that forces due to the presence of a liquid layer (Section 2.2.4) cause the observed damping of ice particle-wall collisions, there are multiple contributing factors that can cause energy losses. However, only viscous damping can capture the velocity dependency seen for ice particles since the other static contact contributions are not estimated to be as sensitive to d, and not velocity dependent. Therefore, it was hypothesized that the energy loss caused by viscous damping E_v (Eq. (2.42)) was the main contribution to the observed energy loss of ice particle collisions when collisional melting occured. The resulting e_n for an ice particle colliding with a wall can then be expressed as

$$e_n = \sqrt{\frac{E_i - E_v - \xi E_i}{E_i}}, \tag{4.6}$$

where ξE_i is the amount of damage at the interface. For the QLL of ice, the function $h(x)$ in Eq. (2.39) is unknown, and d is not constant during the collision. It is, however, reasonable to expect that the resulting E_v will be similar to Eq. (2.43), however with another dependency on d/ε. Therefore, it is argued in Paper II that $E_v \propto (d/\varepsilon)^a$ for some constant a, and it was found that $a = 1.5$ best capture $e_n \propto V_i^{-1}$ using Eq. (4.6). The viscosity μ_f of the damage induced QLL is also unknown, however the viscosity of a liquid is generally expected to be dependent on temperature, as [80]

$$\mu_f \propto \exp\left(\frac{G_0^+}{k_b T}\right), \tag{4.7}$$

where G_0^+ is a potential energy barrier often found by experimental fitting to experimental data. Based on this, it is proposed that

$$E_v = C \exp^{\frac{G_0^+}{k_b T}} V_i R^2 (d/\varepsilon)^{1.5}, \tag{4.8}$$

where C is a constant representing all linear constant terms with unit Pa·s.

4.3 Material Properties

A considerable amount of analyses in this thesis depends on the estimation of material properties. In this chapter, analysis is performed with the following wall materials; ABS polymer, hardened glass, stainless steel, and ice. These walls were chosen because they are common on exterior vehicle surfaces. The work of adhesion W and the effective Young modulus E^* are two of the most important interaction properties since they define adhesive-elastic interactions, and E^* also appears in the collisional melting model. W was estimated by using Eq. (2.27) with literature values for surface energies as inputs. Similarly E^* was estimated by finding values of ν and E for each material investigated. The ν for ice was reported by Gold [81] to be independent of temperature and therefore this has been assumed in this work. E for ice was calculated based on the temperature dependency shown in Hobbs [82] (see S_{11} in Eq. (4.17) in Hobbs [82]) where E only has a weak correlation with temperature, for example, $E(263K) = 9.67$ GPa, while $E(253K) = 9.98$ GPa. An ice particle density of $\rho_p = 917\ \text{kg/m}^3$ was used in the calculations.

The particle-wall interaction properties used are shown in Table 4.1, where the calculated values for E^* and W are obtained by using Eq. (2.33) and Eq. (2.27). The reader is referred to Table 2 in Paper I for the details of the material properties used in these calculations.

Table 4.1: Values of the particle-wall interaction properties used for ice particles. Calculated using Eq. (2.33) and Eq. (2.27).

Wall material	W [J/m^2]	E^* [GPa]
Ice	0.218	5.4
ABS polymer	0.117	1.9
Hardened glass	0.166	9.5
Stainless steel	0.131	10.3

4.4 Ice Particle Experiments

The coefficient of restitution (e_n) for millimeter-sized ice particles colliding with massive walls was measured in Paper II and this section describes the used experimental method. Ice particles were created by generating droplets from a mixture of water and food colorant (to enhance visibility) using a syringe. The droplets were released into liquid nitrogen, causing the droplets to freeze on the surface of the liquid nitrogen. This method of creating ice particles has been used previously by Vargas et al. [83]. The syringe needle used was the smallest available, which defined the size of the ice particles. Each particle was picked up gently using a paintbrush, and the particles were released into a vertical metal pipe. The particles then accelerated due to gravity and collided with the massive wall at a certain impact velocity, V_i. The course of the collision was recorded using a high-speed camera at 4000 frames per second, and the recording began when a laser beam detected a particle outside the metal pipe. The experiments were performed in a large cooling chamber where the temperature could be controlled, and a temperature probe located 20 cm from the massive wall was used to monitor the temperature. One standard deviation from the mean was interpreted as temperature uncertainty. The experimental setup is shown in Fig. 4.3.

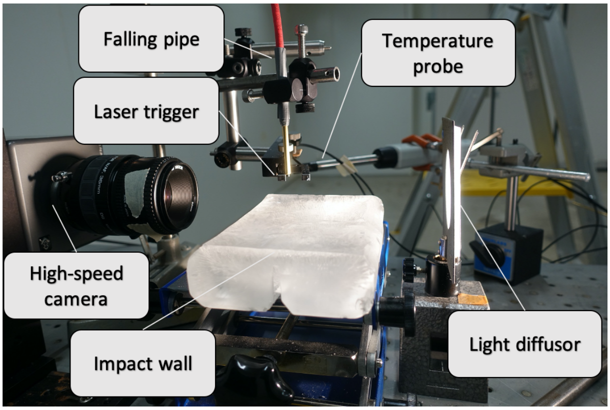

Figure 4.3: Experimental setup for the measurements of the coefficient of restitution e_n, with labels depicting the equipment used.

The recorded sequence of images for a collision was then analyzed using the software Fiji [84] and the particle tracking plugin TrackMate [85]. The images were pre-processed in Fiji, before being analyzed, to improve particle detection by removing gradient backgrounds, image segmentation, and filling holes obtained from the segmentation where holes can occur because of light reflections in particles. The particle radius of each frame in a collision sequence was calculated by adding the pixel area of every pixel in the segmented sphere. The overall particle radius for a collision was then calculated as the median of the obtained radii in a collision. The average diameter of the ice particles was 1.64 ± 0.15 mm. Output for the trajectory points before and after collision was taken from TrackMate. These points were then post-processed to calculate the corresponding velocity before and after collision. The uncertainty of the center position, δx, for a particle was quantified by manually measuring the center points. The average difference between this manual measurement and the output from TrackMate was $\delta x = 26.13\ \mu$m, which propagates to a velocity uncertainty of $\delta V = 4000 \cdot 26.13 \cdot 10^{-6} = 0.105$ m/s. The uncertainty of the coefficient of restitution, δe_n, was then calculated based on the propagation of uncertainties as

$$\delta e_n = \sqrt{\big(\frac{\delta V_i}{V_i}\big)^2 + \big(\frac{\delta V_r}{V_r}\big)^2}\, e_n. \tag{4.9}$$

The study focused on normal collisions, and collisions recorded with a clear tangential impact were removed from the data set.

4.5 Results

The particles studied experimentally in Paper II had a average diameter of 1.64 ± 0.15 mm, which is smaller than the results in Higa et al. [42]. However, the JKR model predicts that $V_s \propto D_p^{-5/6}$, and the particles studied in Paper II are still so large that they yield very low values of V_s ($V_s \approx 4 \cdot 10^{-3}$ m/s). Therefore, it was not experimentally possible to validate the JKR model's predictions using these particles since it was not possible to perform measurements with sufficiently small V_i. For the experiments in Paper II, V_i were significantly larger than V_s. Therefore, the analysis for low velocity collisions in this chapter is purely based on theoretical predictions and no experimental data is available to validate those predictions.

4.5.1 Low Velocity Collisions

Fig. 4.4 shows analytical predictions of the energy loss for single ice particles colliding with a massive wall using the JKR model (Eq. (4.3) and Eq. (4.4)). Fig. 4.4a shows V_s as a function of D_p for the four studied wall materials (ice, ABS polymer, hardened glass, and stainless steel). Generally, it is expected that the cohesion of a material is higher than the adhesion, and it is therefore expected that the ice wall has the highest V_s. However, the ABS polymer has the second highest V_s of the studied wall material, which is not as expected since this wall has the lowest surface energy, which yields the lowest W of the studied wall materials. This occurs because E^* is also lowest and since $V_s \propto W^{5/6} E^{*-1/3}$, this yields higher estimations of V_s than for hardened glass or stainless steel.

Fig. 4.4b shows e_n as a function of V_i for ice particles colliding with a massive wall. The figure shows e_n for the wall material with lowest (stainless steel) and highest (ice) predicted V_s for $D_p = 50$ μm as well as $D_p = 100$ μm. Different particle sizes as well as wall materials are predicted to yield differences in e_n for low values of V_i however for high V_i ($V_i > 0.3$ m/s) the predicted e_n is similar $e_n \approx 1$.

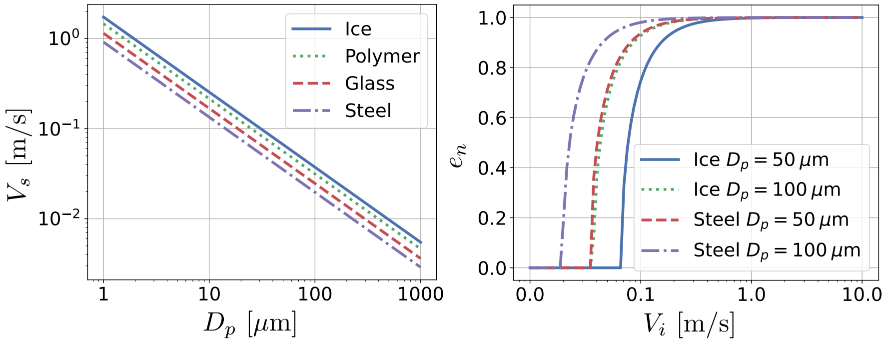

(a) The predicted V_s for massive walls of different materials as a function of D_p.

(b) The predicted e_n as a function of V_i, for $D_p = 50\mu$m and $D_p = 100\mu$m and for a steel and ice wall.

Figure 4.4: Analytical predictions of V_s and e_n for ice particles colliding with massive walls at $T = 261$ K.

4.5.2 High Velocity Collisions

The results from the experiments on millimeter-sized ice particles colliding with massive walls showed that e_n depends both on T and the wall material studied. It was found that the e_n of ice particles decreases for increasing T, and is lowest for the glass wall, while highest for the ABS polymer wall. For more details of the experimental results obtained, the reader is referred to Paper II, where the results are also compared to the previous work by Higa et al. [42]. The obtained expression for E_v in Eq. (4.8) has two unknown constants C and G_0^+. A non-linear least-squares fit was performed using the experimental measurements as input to obtain the values for C and G_0^+. This fit was carried out for ice particles colliding with an ice wall for both T = 267 K and T = 254 K individually, so that the results of the fit could be compared with each other, and remarkably similar values of C and G_0^+ were obtained. The average values of the unknowns were found to be $C = 0.5 \cdot 10^{-10}$ Pa·s and $G_0^+ = 0.5$ eV, and the best fit at different temperatures only varied by 0.6% and 0.5% for C and G_0^+. Fig. 4.5 shows experimental measurements (markers) and the predicted e_n using the collisional melting model (lines) for ice particles colliding with massive walls of ice, polymer, and hardened glass. Since the model is fitted towards the experimental data for the ice wall, it is expected that it will predict the trend well for these. However, as can be seen, the model also captures the differences in wall material, which indicate that the dependency e_n has on E^* is captured by the model. These predictions of e_n deviate from the previous work by Higa et al. [42], where the collisional melting model predicts a higher stick velocity V_{cm}, where particles are predicted to stick caused by the damage induced melting. This is not predicted by Eq. (2.18) where the function $f(x) = x^{-\ln(x)}$ only approaches zero as $x \to \infty$. This higher stick velocity occurs when the incoming kinetic energy is equal to the sum of the dissipated energy and can be expressed as

$$V_{cm} = \frac{3C}{\pi \rho_p (1-\xi)} \exp\left(\frac{G_0^+}{k_b T}\right) \frac{1}{D_p} (d_H/\varepsilon)^{1.5}, \tag{4.10}$$

where d_H is the melted liquid layer thickness when this sticking occurs. Unfortunately this thickness is itself a function of V_{cm} and an analytical solution cannot be obtained for this velocity. In Paper II the same velocity is described by the notation "V_H", but there is a typo in Eq. (18) in Paper II, where the term $1/(\rho_p D_p)$ is missing, however the calculated V_{cm} is correctly including this term in Fig. 13b (Paper II).

The unknown coefficients in the derived collisional melting model were obtained from experiments on ice particles with a fixed particle size. To assert how the model will extrapolate outside this particle size, the experimental results published by Higa et al. [42] were extracted for $D_p = 2.8$ mm and $D_p = 8$ mm at $T = 262$ K. Fig. 4.6 shows the e_n of ice particles colliding with a massive ice wall for these particle sizes combining both the experimental results and the predicted e_n based on the collisional melting model. The figure depicts that the size dependency observed for the e_n of ice particles is well predicted by the collisional melting model, where more damping is predicted for larger particles.

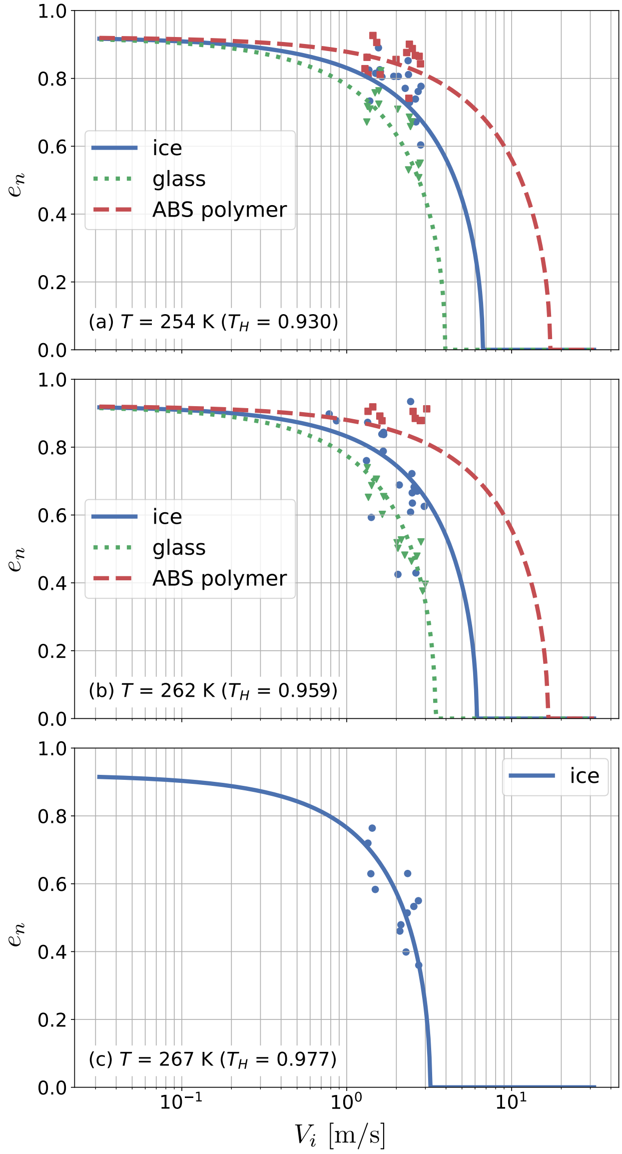

Figure 4.5: The e_n of ice particles (with $D_p = 1.64$ mm) colliding with massive walls as a function of V_i. Solid, dashed, and dotted lines show the predicted e_n using the collisional melting model for ice particles colliding with an ice wall, a polymer wall, and a glass wall, respectively. Marker symbols (circle, square, and triangle) show experimental measurements for ice particles colliding with an ice wall, a polymer wall, and a glass wall.

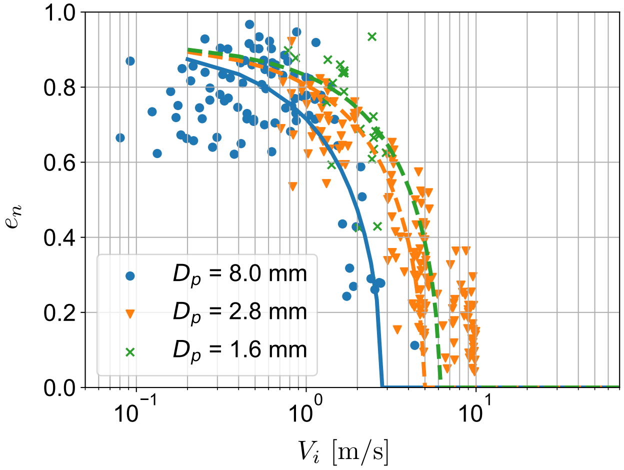

Figure 4.6: The e_n for ice particles colliding with massive walls. Circle and triangle markers show experimental results published in Higa et al. [42] for particle sizes $D_p = 8$ mm and $D_p = 2.8$ mm respectively, both at $T = 261$ K. Cross markers show experimental results published in Paper II for $D_p = 1.6$ mm at $T = 262$ K. Lines depict the predicted e_n using the collisional melting model for ice particles.

4.5.3 Regime Map for Ice Particle Collisions

The combined work of Papers I and II predicts that the velocity of impact has a nonlinear influence on the e_n of ice particles colliding with massive walls. A regime map of e_n can be created by combining the effect of adhesive-elastic interactions e_{jkr} (Eq. (4.4)) with the collisional melting model e_{cm} (Eq. (4.6)). Multiple coefficients of restitution can be combined by addition as [50]

$$(1 - e_n^2) = \sum_i (1 - e_i^2), \tag{4.11}$$

or by taking the product of each contribution [57]

$$e_n = \prod_i e_i. \tag{4.12}$$

Fig. 4.7 shows the combined e_n using Eq. (4.11) and Eq. (4.12) as well as the individual contributions e_{jkr} and e_{cm}. While both approaches yield similar results when using Eq. (4.12), the V_s is not changed and was therefore used in the upcoming analysis in this section. The combined model predicts a horizontal plateau around the point

$$e_n = \sqrt{1 - \xi}, \tag{4.13}$$

where e_n is constant, similar to what has previously been observed by Higa et al. [42], which was then called a quasi-static regime.

The particle sizes studied in Higa et al. [42], as well as in Paper II, are significantly larger than the particle sizes expected in a snow cover. For

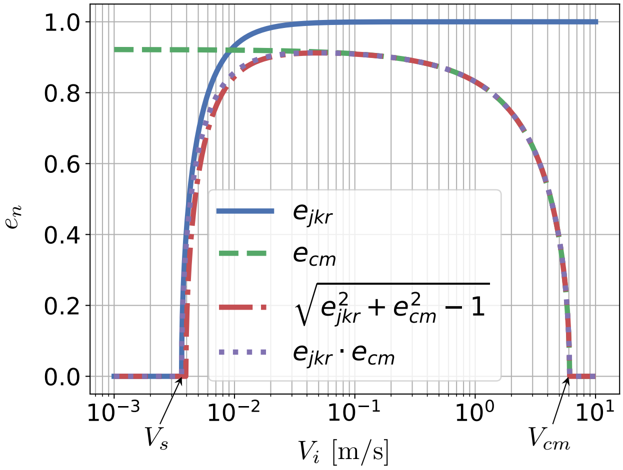

Figure 4.7: The e_n for ice particles colliding with massive walls with $D_p = 1.6$ mm at $T = 261$ K. Blue solid line shows e_n for the JKR model e_{jkr}, and green dashed line shows e_n for the collisional melting model e_{cm}. Dashed red line shows the combined e_n by adding the contributions. Dotted purple line shows the combined e_n by taking the product of the contributions.

decreasing particle sizes, both V_s and V_{cm} are predicted to increase, causing smaller ice particles to stick more at low velocities but less at higher velocities. This is depicted in Fig. 4.8a, which shows the e_n of ice particles colliding with a massive ice wall combining e_{jkr} and e_{cm} at $T = 261$ K. It is predicted that $V_{cm} > 10$ m/s for all these particles except for $D_p = 800\,\mu$m, which has a V_{cm} slightly below 10 m/s. Fig. 4.8b shows the combined e_n as a function of V_i for ice particles colliding with different massive walls. The e_n was calculated for particles with $D_p = 100\,\mu$m at $T = 261$ K. The energy loss associated with low velocity impact in a collision, E_s, is proportional to $W^{5/3}E^{*-2/3}$, therefore, particle-wall interactions with high E^* (e.g. when the wall is glass) will yield low losses in a collision. In contrast, the energy loss E_v of high-velocity impacts is proportional to $E^{*4/5}$, which means that particle-wall interactions with low E^*, such as for a polymer wall, will have lower losses. This gives a complex dependency on the optimal wall material for avoiding snow accumulation, since the dependency changes depending on the regime of impact. These results imply that it might be beneficial to have a sensor cover of different materials, depending on where on the vehicle the sensor is located. For example, for the radar cover at the front of a car, one would expect high-velocity collisions similar to the speed of the vehicle, and thus a material that yields a low E^* might be beneficial. While in the rear wake of the car, a sensor cover should instead have a material with high E that would cause a high E^* for the interaction with ice particles.

The collisional melting model depends on T where greater melting of a liquid layer is expected at higher temperatures. The resulting viscous energy damping is predicted by the model to be higher at higher temperatures because of the increased QLL. Paper I discusses dry snow adhesion at a cold enough

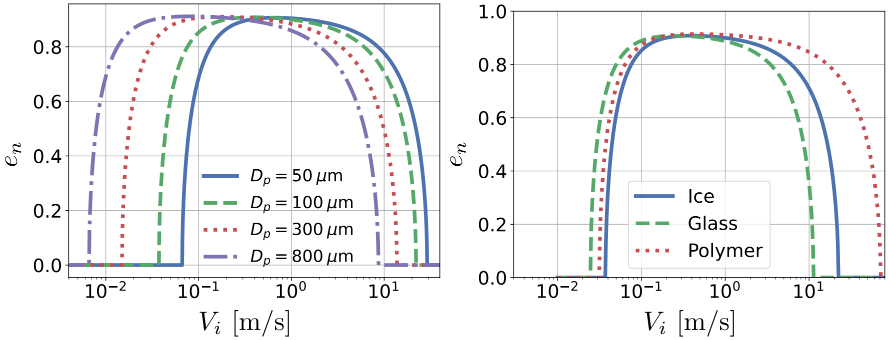

(a) Varying particle sizes colliding with a massive ice wall at $T = 261\,$K. Solid blue line for $D_p = 50\,\mu$m, green dashed line for $D_p = 100\,\mu$m, red dotted line for $D_p = 300\,\mu$m, and purple dashed-dotted line for $D_p = 800\,\mu$m.

(b) Varying massive walls for $D_p = 100\,\mu$m at $T = 261\,$K. Solid blue line for an ice wall, green dashed line for a hardened glass wall, and red dotted line for an ABS polymer wall.

Figure 4.8: The combined coefficient of restitution e_n for ice particles colliding with massive walls as a function of impact velocity V_i at $T = 261$ K.

fixed temperature, where the effects of a liquid layer in equilibrium are assumed to be negligible. For temperatures closer to the melting point of water it is not known what effect this will have on W, but its plausible to assume that W will increase with increasing T, causing V_s to increase with increasing T. Fig. 4.9 shows e_n for ice particles colliding with an ice wall at different temperatures. Since e_{jkr} is established under the assumptions that ice is sufficiently cold, only $T = 262$ K was plotted for this low-velocity regime.

4.6 Discussion

The modeling of collisions in the intermolecular regime in this work is based on the assumption that the collisions are at sufficiently low velocities, such that the energy dissipation is dominated by the adhesive-elastic interactions. While the JKR model has been validated experimentally for other adhesive particles, the predicted energy loss in this work is only based on theoretical estimations and no experimental results have been found to validate the predictions for the collisions in the intermolecular regime. Ideally, experiments with micrometer-sized ice particles, colliding with massive walls, at varying V_i and E^* would be needed to assert the validity of the model, which would be, in-practice, challenging experiments to perform for such small particles. Even though Paper II studied ice particles that were significantly smaller than the previous studies, for example by Higa et al. [42], the particles studied in Paper II were still so large that the predicted V_s would be approximately 4 mm/s, and it would be very hard to perform experiments at such low collisional velocities. There are other studies that measured the pull-off force for ice particles, for example by Bahaloo et al. [86] or Shazbo and Scheebeli [87], however it is not

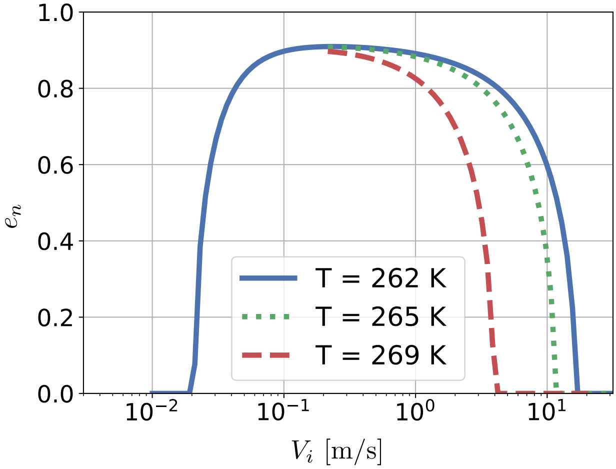

Figure 4.9: The combined coefficient of restitution e_n for ice particles colliding with massive ice walls as a function of impact velocity V_i for varying temperatures. Solid blue line at $T = 262$ K, green dashed line at $T = 265$ K, and red dotted line at $T = 269$ K.

obvious how to translate these static measurements into a collision, since both the contact time and load are significantly larger than what is expected for collisions in the intermolecular regime. The model was also established under the assumption that the ice is sufficiently cold, which is assumed to be the case for ice at $T = 262$ K. For larger T it is possible that the premelted QLL will cause increased adhesion, for example by an increased W, however the exact form of these increases are unknown.

The collisional melting model was derived with the assumption that the increased melting causes viscous damping in the collisions. The model was also shown to capture the dependencies on T, D_p, as well as E^* seen in experiments for ice particles colliding with massive walls. However, the model is derived with coefficients that are fitted to some of the experiments, and it is not possible to prove if it is viscous damping that causes this extra energy damping. It could be caused by a combination of melting, plastic deformation, as well as fragmentation of the particles at impact. The model predicts that for sufficiently high velocities $V_i \geq V_{cm}$, a particle will adhere to the wall on impact. This was however not observed for the experiments in Paper II, since the velocity of impact was $V_i < V_{cm}$, but occurrences when $e_n = 0$ were reported by Higa et al. [42] for sufficiently high velocities. Hauk et al. [88] showed that for sufficiently high velocities of impact the ice particles can have a major fragmentation and in Paper II it was defined a regime of fragmentation for sufficiently high V_i. However, it is not known which velocities will cause fragmentation and since the particles then can break up into smaller pieces, it can be argued that e_n is undefined for these types of collisions. The V_{cm} is predicted to increase for smaller particles, and as can be seen in Fig. 4.8a this velocity becomes larger for ice particles that are $50 - 300\,\mu$m. Since the topic of this thesis is regarding vehicles driving on snow-covered roads it reasonable to assume driving speeds of approximately 50-90 km/h, and particle-wall collisions are expected to be lesser than these speeds. If V_{cm} is larger than the driving speed it is possible that modeling of the collisional melting regime is obsolete and could be omitted to reduce complexity. This will be further discussed in Chapter 6 where fine machine-made snow is studied.

The analysis in this chapter only considered single particle collisions with massive walls. Particles can however also stick together to form agglomerates or aggregates. Here, an aggregate is defined as multiple ice particles that have, at rest, formed strong bonds together over time due to either sintering or melt and freeze cycles. While an agglomerate is referred to as multiple particles weakly bonded together over a shorter time. Agglomerates could potentially form while ice particles are dispersed in air due to particle-particle collisions. In Paper I collisions of agglomerates of ice particles were simulated using DEM, where both small agglomerates (up to five particles), as well as large agglomerates (1000 particles) were studied. For these simulations, adhesive interactions in the tangential direction had to be taken into account, and it was found that the energy dissipation largely increased for the agglomerates compared to single ice particles. This can be explained by the increase in the possible tangential movement of particles and the subsequent increase in energy loss caused by tangential interactions. The increased energy loss was substantial; the largest agglomerate with 1000 particles adhered to a polymer wall at 0.5 m/s, comparably, to a single ice particle with the same size as the individual particles in the agglomerate, would stick at 0.056 m/s. This means that the E_s for this agglomerate is almost 80 000 times higher than for the single ice particle.

Chapter 5

The Angle of Repose of Snow

The angle of repose α (illustrated in Fig. 5.1), is a measure that reflects the internal friction in a granular material and is commonly used for classifications of powders [89]. Various experimental approaches exist to measure the angle of repose and the measured angle is known to be sensitive to which approach is used [90]. For a sintering material such as snow, large differences in angle are to be expected if the material is measured using a static approach where the material has been at rest for a long duration, or using a dynamic approach that involves movement of the particles in the material. Snow at rest for a long time will have strong bonds between ice particles and therefore the internal friction will be different in contrast to ice particles that are colliding and accumulating in a pile. When a vehicle is driving on a snow-covered road, a dispersed cloud of ice particles is generated from the tires that can deposit and accumulate on exterior surfaces. By measuring the α of snow using a dynamic approach this process is imitated where the bonds between ice particles are broken to create a dispersed cloud of ice particles. The α of snow has been previously studied by Kuroiwa et al. [91] and Willibald et al. [92], where the experimental methods used in these studies are similar to the one used in Paper III, and the results obtained in Paper III were compared to these previous studies.

As shown in the result section, α does not only depend on the experimental setup but also on the experimental conditions. It is therefore important to emphasize that a measurement of the α of snow should not be taken without context of how it was measured. For example, at which fall height H measurements were done.

5.1 Experimental Method

The used experimental setup consisted of two metal tables: a small table with a standing solid cylinder and a larger table with an electric sieve shaker holding two sieves. The snow was sieved to separate particles from each-other and pore sizes of 3.15 mm and 2.5 mm were used for sieve 1 and 2 respectively. The setup is depicted in Fig. 5.1.

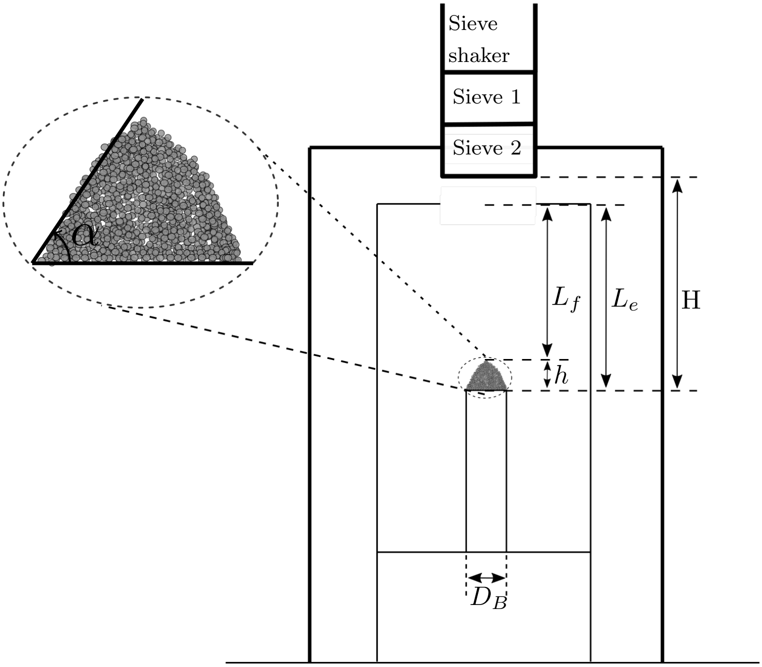

Figure 5.1: Experimental setup for the angle of repose of snow α (highlighted in the inset), important dimensions are labeled.

An experimental trial was conducted by loading a snow sample in the sieve shaker and then activating the shaker. The snow falling through both sieves was then shaken, causing a dispersed cloud of particles that later collided with the spherical base of a cylinder below the sieves and accumulated to a heap formed as a cylindrical cone. The shaking of snow through the sieves was continued until the heap height h stopped changing over time. The α was estimated indirectly by measuring h and then calculated as

$$\alpha = \arctan\Big(\frac{2h}{D_B}\Big), \tag{5.1}$$

where D_B is the diameter of the cylinder base. To estimate h, the distance between the top of the inner table and the top of the snow heap L_f, was measured using a depth gauge that was mounted on top of the smaller metal table. This distance was subtracted from the unloaded distance L_e, when no snow was present on the circular base. Since ideal cones with sharp vertices were not always obtained, a correction factor c was subtracted from the distance L_f, i.e.

$$h = L_e - (L_f - c). \tag{5.2}$$

All experimental trials were photographed, and the correction factor was measured using images from each trial. An example of such a correction is shown in Fig. 5.2.

The resulting h from Eq. (5.2) was estimated to have an uncertainty $\delta h = 2$ mm. This yields an asymmetric confidence interval for α caused by the arctan

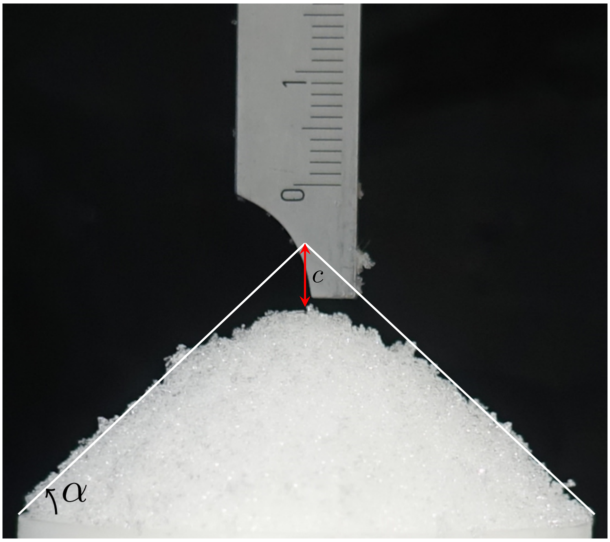

Figure 5.2: Illustration of the correction factor c added to cone height h for imperfect cone vertices.

function (Eq. (5.1)). Since the asymmetry is small and arctan is a monotonically increasing function, the confidence interval was simplified as,

$$\alpha \pm \delta\alpha \approx \alpha \pm \left(\arctan\left(\frac{2(h+\delta h)}{D_B}\right) - \alpha \right). \tag{5.3}$$

For a certain measurement point of interest, the experimental trials were repeated, and averaged values were calculated for α based on the repetitions. The resulting uncertainty quantification for these averages was computed using a conservative error envelope,

$$\delta\alpha = \max(\delta\alpha_{max}, 2\sigma_\alpha), \tag{5.4}$$

where σ_α is the standard deviation of α for the repetitions.

To assert the reliability of the measurements, the repeatability was studied by repeating the same measurement multiple times. It was found that repeated measurements only yielded minor differences in obtained α (see Appendix A in Paper III for further details).

For this experimental setup the α of snow can be measured at varying H and D_B, as well as changing T. In this work, the same sieves were always used and the sensitivity to pore space of the sieves were assumed to be negligible since they were significantly larger than the particles studied. Experimental measurements were performed with varying D_B from 25 to 100 mm and the measurements performed showed no dependency of α on D_B, as previously also observed by Kuroiwa et al. [91] and Willibald et al. [92].

5.1.1 Snow Characterization

Seven different snow samples were studied in this work, and these were characterized using the particle shape classes in the international classification for seasonal snow on the ground [16].

Ice particle statistics for a snow sample were obtained by taking microscope photographs of particles on cover slips that were then analyzed using image analysis. The collection of ice particles on a cover slip is not trivial, and the method used can influence the obtained statistics. As mentioned by Allen [93], direct collection from a heap of powder with different particle sizes should be avoided since there is risk of segregation that can influence the result. In this work the main method used was to place snow in a sieve shaker and the shaker was then run for a short period of time, while a cover slip was placed directly under the sieves. The slide was then photographed using digital microscopes, where most slides were photographed using a magnification of 100x−200x. The microscopes were calibrated before usage with a calibration scale. The particle boundaries from the images were extracted using manual segmentation in the image analysis program Fiji [84]. Two particle properties were calculated based on the particle boundaries: the projected diameter d_A, and the circularity $\hat{\phi}$. These were calculated as

$$d_A = \sqrt{\frac{4A_p}{\pi}}, \tag{5.5}$$

and

$$\hat{\phi} = \frac{4\pi A_p}{P^2}, \tag{5.6}$$

where A_p is the particle cross-section area and P is the length of the particle boundary. Ideally, the three-dimensional measure sphericity ϕ would be more useful to obtain for analysis of the results (see Eq. (2.59) for the definition of ϕ). However, the microscope slides are only two-dimensional data (without depth), and therefore the circularity was used as an approximation for the sphericity i.e., $\hat{\phi} \approx \phi$. To obtain representative values for each snow sample, the volume-weighted average of the projected mean diameter D_v, and the median of the circularity $\hat{\phi}_m$ were calculated for each snow sample. Volume weighting was used for the particle size to account for the volumetric effect a particle has on the overall volume of a snow heap, and the median of the circularity were calculated instead of arithmetic average to exclude outliers from the calculation. The morphological particle shape class of a snow sample was determined by visual inspection of the microscope images, and most of the particles studied in this work were classified as round grains (RG). Microscope photographs of six of the snow samples (all samples except for the SH 1 sample) are shown in Fig. 5.3.

Measurements of d_A and $\hat{\phi}$ were performed for all the snow samples except for the SH 1 and PP 1 samples, where the two samples were excluded due to the observed shape complexities in these samples. Normalized particle size distributions are shown in Fig. 5.4, where particle size distributions for RG 1 and RG 2 are shown in Fig. 5.4a, and particle size distributions for MM 1, RG 3, and RG 4 are shown in Fig. 5.4b. Fig. 5.5 shows $\hat{\phi}$ using a boxplot centered around the median for $\hat{\phi}$. The characterization of the seven different samples measured and the experimental conditions are summarized in Table 5.1.

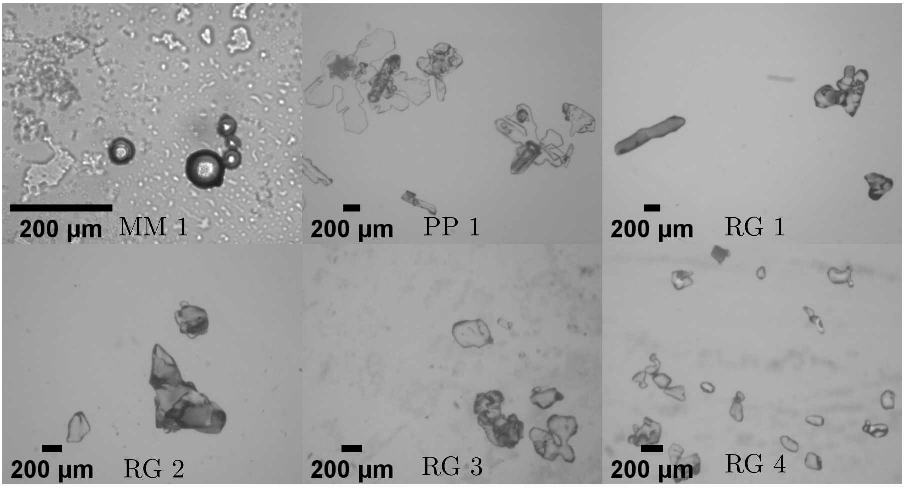

Figure 5.3: Examples of microscope images for six snow samples.

Samples RG 1, RG 2, RG 3, PP 1, and SH 1 were all collected outdoors from snow covers present on the ground in winter conditions, where only the top layer of snow was collected. RG 4 was collected from an underbody panel of an electric vehicle that had been driven 100 km on a snow-covered road at the same geographical location and time as RG 3 was collected. Comparisons between RG 3 and RG 4 are therefore of special interest. The RG 3 sample was collected when snow was present on the ground, and RG 4, where snow accumulated on a vehicle driven on a snow-covered road. Theoretically, RG 4 is a subset of RG 3. The characterization reveals that the particles in RG 3 are larger and less spherical than RG 4. The machine made snow (MM 1) was collected from the ground in a climate wind tunnel using a snow cannon that is described in more detail in Chapter 3. RG 1 and RG 2 were together with PP 1 measured in a cooling chamber where T could be controlled with a high precision (±0.5°C). Measurements of RG 3 were performed in a cooling chamber with lower temperature control (±2 °C). These temperature fluctuations were estimated by monitoring the air temperature over time and taking 2σ, as the precision where σ is the standard deviation of the measurement series. The measurements on the RG 4 and SG 1 samples were performed outdoors at ambient conditions.

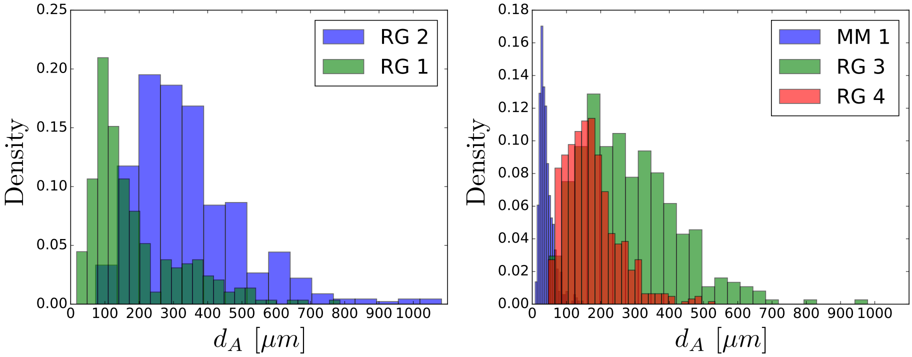

(a) Normalized particle size distributions determined from image analysis for snow samples RG 1 (green) and RG 2 (blue).

(b) Normalized particle size distributions determined from image analysis for snow samples MM 1 (blue), RG 3 (green), and RG 4 (red).

Figure 5.4: Particle size distributions for studied snow samples.

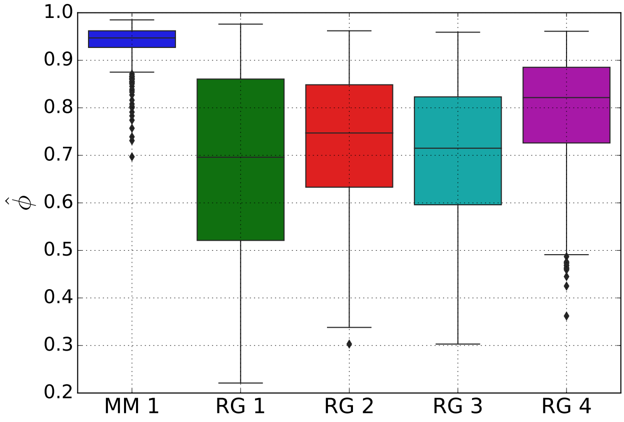

Figure 5.5: Snow particle circularity $\hat{\phi}$ determined from image analysis for the snow samples MM 1, RG 1, RG 2, RG 3, and RG 4.

The measurements of samples RG 1 and RG 2 are the two largest datasets of the α of snow in Paper III, were the number of measurements are significantly larger than any of the other measured samples. While the other samples were studied directly after they were collected, these two samples were first stored in a cooling chamber at $-5\,^{\circ}$C, where RG 1 was stored for 3 weeks, and RG 2 was stored for 4 days before testing. This was done for the particles in each sample to approach an equilibrium shape such that measurements could be performed over consecutive days without further change in particle morphology.

Table 5.1: Snow characterization and experimental conditions for snow samples used for measuring the α of snow. The labels indicate: round grains (RG), machine made snow (MM), precipitation particles (PP), and surface hoar (SH).

Label	$\hat{\phi}_m$	D_v [μm]	T [°C]	H [m]
RG 1	0.70	455	-2 to -14	0.07-0.34
RG 2	0.75	775	-1 to -14	0.07-0.25
RG 3	0.72	492	-16 to -27	0.1-0.25
RG 4	0.82	288	-14	0.1-0.25
MM 1	0.95	80	-9 to -13	0.1-0.34
PP 1	N/A	N/A	-12	0.1
SH 1	N/A	N/A	-14	0.1

5.1.2 Data Interpretation

In-order to quantify the experimental trials performed, the analysis was simplified by theoretically evaluating single ice particles colliding with massive ice walls. An ice particle that is falling a certain H will accelerate according to Eq. (2.65) where the sum of forces is expected to be the difference between the gravitational force and the drag force. As the particle accelerates, this difference between forces will decrease, and therefore the acceleration will decrease. The particle will eventually collide with the massive wall with an impact velocity $V_i \leq V_\infty$, where V_∞ is the terminal velocity which will be reached for a sufficiently large H. All the snow samples in this work are polydisperse where multiple particle sizes are present in the same snow sample. However, to simplify the analysis it is assumed that D_v and $\hat{\phi}_m$, obtained for each snow sample, are relevant representations of the size and shape of the samples. D_v was therefore used to assert effect of the particle size and relate that to α. The two variables D_v and $\hat{\phi}_m$ were used to calculate the samples averaged impact velocity V_a at the spherical base of the cylinder, where $V_a = V(D_v, \hat{\phi}_m, H)$. Calculations of V_a were performed by solving Eq. (2.65) over time using the Haider-Levenspiel correlation [72], where C_d is then a function of D_v, $\hat{\phi}_m$, and V_a. The predicted V_a is plotted as a function of H in Fig. 5.6 for multiple particles sizes ranging from $D_p = 100\,\mu$m to $D_p = 1000\,\mu$m. The figure also depicts the effect of $\phi = 1.0$, as well as $\phi = 0.6$ where the deviations between the α values increase with increased H. The figure depicts that $V_a < 2$ m/s for the studied experiments in this work. The magnitude of velocity can be related to the previous chapter predicting different regimes of the e_n of ice particles colliding with a massive ice wall. As shown in Fig. 4.8a, even for the case of $D_p = 800\,\mu$m, which is relevant for the sample with largest particles (RG 2 sample with $D_v = 775\,\mu$m), a velocity of impact around 2 m/s is significantly lower than the estimated V_{cm}, and thus the velocities can be regarded to be in the regime of either a plateau with constant e_n, or in the regime of adhesive-elastic interactions. To simplify the analysis, effects of collisional melting on the α of snow were therefore neglected for the analysis in this chapter.

For the experimental trials performed on the α of snow, it was observed that particles bounced at initial impact and multiple impacts occur. This means that the particles approach the adhesive-elastic interaction regime of

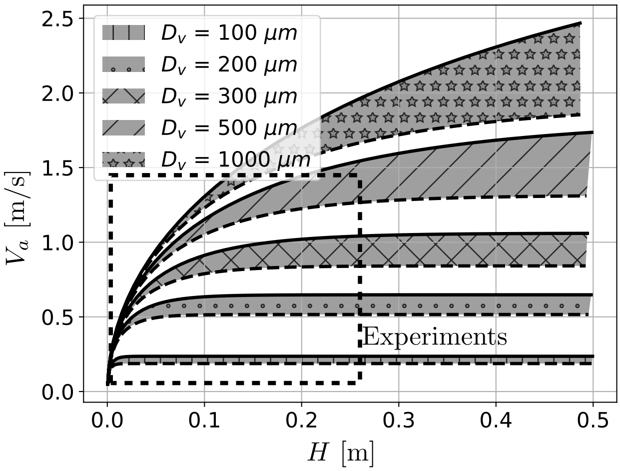

Figure 5.6: Predicted V_a of ice particles as a function of H for different particle sizes. Solid lines show spherical particles ($\phi = 1.0$), and dashed lines shows non-spherical particles ($\phi = 0.6$). The shaded areas show the range between these values of ϕ.

collisions and then eventually adhere to the heap, if it does not bounce outside the spherical base. However, assuming that the initial impact is a relevant measure of the resulting α, a dimensionless number, the cohesion number Co was proposed in Paper III to quantify the ratio between cohesion and impact energy. The number is defined, for a single ice particle colliding with a massive flat wall, as the ratio between the cohesive energy E_s (Eq. (4.2)) and the impacting kinetic energy E_i,

$$Co = \frac{E_s}{E_i} \approx \frac{5}{\rho_p V_i^2}\left(\frac{\pi^2 W^5}{D_p^5 E^{*2}}\right)^{1/3}, \tag{5.7}$$

where for the specific analysis in this work $V_i = V_a$ was used. The proposed Co in Paper III is similar to what was previously proposed by Behjani et al. [94], except that in their work a gravitational potential energy was used, instead of E_i. The Co is also similar to the commonly used Bond number [18], where the main difference is that the Bond number is a ratio of forces instead of energies and will not take into account elasticity. While the dimensionless number in Paper III is relevant for cohesion and therefore called the cohesion number, the same definition could be used for adhesion, for example, regarding interactions of different materials when ice particles collide with a sensor surface that is not made of ice.

In Paper III obtained values of the α of snow was correlated to Co using a polynomial fit. This calculation however assumes that V_a is independent on D_v which is a simplification that could be challenged since $V_\infty = V_\infty(D_p)$. It is therefore argued here that it's more reasonable to assume that V_a has the same proportionality on D_p as V_∞. How V_a then depends on D_p can be divided into two regimes, where for creeping flow ($Re_p < 1$) it is expected that $V_a \propto D_p^2$, while for sub-critical flow ($10^3 < Re_p < 2 \cdot 10^5$) it changes to $V_a \propto D_p^{0.5}$ (see

Thurton and Clark [95] for explicit equations for $V_\infty(D_p)$). In between these regimes the dependency is more complex and can be expressed as a function of both $D_p^{0.5}$ and D_p^2 [95]. For the estimated V_a on the α of snow nearly all measurements are in this transition regime (above the creeping flow regime, but below the sub-critical regime). To simplify the analysis one can assume that $V_a \propto D_p^{C_1}$ for $0.5 \leq C_1 \leq 2$: Using this assumption in Eq. (5.7), it follows that

$$Co \propto D_p^{-(2C_1+5/3)}, \qquad \text{for } 0.5 \leq C_1 \leq 2, \tag{5.8}$$

for the measurements of α of snow in the present work, where C_1 depends on Re_p.

5.2 Results and Discussion

Measurements of α were performed for the seven different snow samples at the experimental conditions as depicted in Table 5.1. Three distinct variables were identified as important for the resulting α: the snow temperature T, the experimental fall height H, and the particle average size D_v.

Fig. 5.7 shows α as a function of snow temperature T, for the studied snow samples with $H = 0.1$ m. The α of snow varies significantly between the snow samples, even for similar T and at the same H. An interesting comparison is the results for the SH 1 and PP 1 sample. Even though the temperature is similar the difference in α is almost 30°. The precipitation particles in the PP 1 sample were collected from snowfall close to 0 °C, where a rich variate of snowflakes such as dendrites, plates, and needles were observed in the microscope slides. Since the particle shape class is similar for these samples, the potential difference is the effective curvature of contact, were as the surface hoar particles in SH 1 consisted of long single crystalline particles, and the precipitation particles have more complex irregular forms that more easily break up into small pieces by the sieves. The observed difference between the PP 1 sample and the SH 1 sample is in line with previous research that has shown that hoar particles have such low cohesive properties that they can cause avalanches when present in depth of a snowpack [39, 96].

For certain snow samples and experimental conditions $\alpha = 90°$ is obtained, which means that the snow heap continued to increase vertically until the heap touched the lower sieve. This phenomenon is referred to as a diverging α, since the α is not well defined for these measurements. This occurs when the cohesive forces are dominating over gravity causing the heap to continuously grow. For all measurements of the MM 1 sample, a diverging α is obtained, indicating that these snow samples are more cohesive and different from the other studied snow samples.

5.2.1 Snow Temperature

In Fig. 5.7 it can be seen that α changes with T, and α increases as T approaches the melting point of water. Previous work on the α of snow by Willibald et al. [92] and Kuroiwa et al. [91] also concluded that α depends on T. Both studies suggested the presence of a QLL might be the reason for this observed

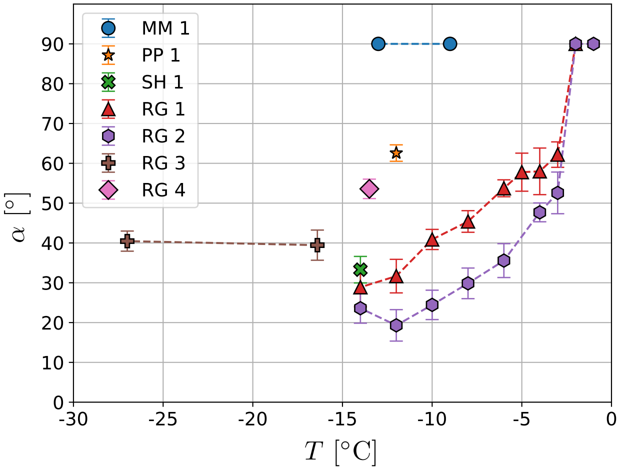

Figure 5.7: The α of snow for the different snow samples as a function of T with $H = 0.1$ m, where the mean values of repeated trials are plotted with the error bars representing $\delta\alpha$.

dependency. Fig. 5.8 illustrates how α changes for increasing T, where as single measurement trials for the RG 1 sample at $H = 0.1$ m are shown for different T. Fig. 5.9 shows the measurements of α for snow samples RG 1 and RG 2 as a function of T for varying H. The figure highlights that α is sensitive to T especially for $T > -12$ °C, and that higher H causes diverging α at lower T. Willibald et al. [92] proposed an empirical model for α that can be written as

$$\alpha = A + B \exp\big(- G^{+}/(k_b T)\big), \tag{5.9}$$

where A and B are constants, G^{+} is the activation energy, and k_b is the Boltzmann constant. From curve fitting of their experimental data they obtained $G^{+} = 1.2$ eV. The experimental results for RG 1 and RG 2 were also fitted to Eq. (5.9) and the results are shown in Table 5.2. Data points with diverging α ($\alpha = 90°$), as well as temperature series with less than four data points were omitted from the fitting. We observed that $G^{+} \approx 1.15$ eV for all the different temperature series, which is almost identical to what was obtained by Willibald et al. [92]. This shows that the α of snow depends on T and seems to follow an Arrhenius relation with $G^{+} \approx 1.15$ eV. Its plausible that, as predicted by Eq. (2.8), this is caused by the presence of a QLL on the surface of the ice, and that the cohesive properties of ice (for example the work of adhesion W) may strongly depend on T.

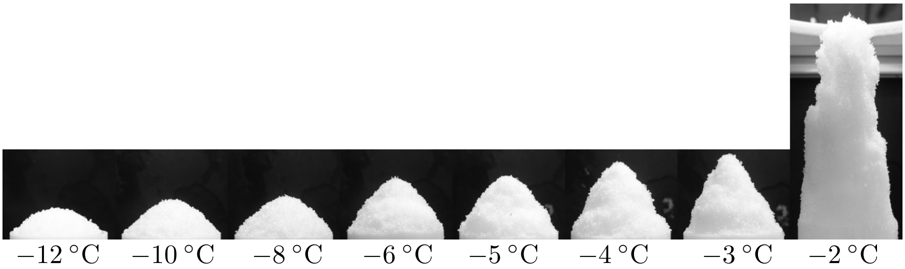

Figure 5.8: Photographs of some of the experimental trials of the α of snow for the RG 1 sample at varying T.

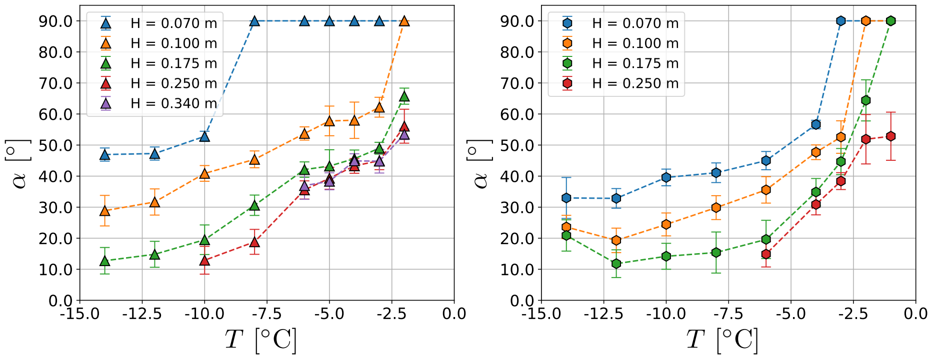

(a) RG 1 snow sample.

(b) RG 2 snow sample.

Figure 5.9: The α of snow as a function of T for varying H, where the mean values of repeated trials are plotted with the error bars representing $\delta\alpha$.

Table 5.2: Least squares fit of Eq. (5.9) for the measured α for the RG 1 and RG 2 samples at varying H.

Sample	H	R^2	A	B	G^+ (eV)
RG 1	0.10	0.93	27.84	$0.92{\cdot}10^{23}$	1.15
	0.17	0.95	9.58	$0.99{\cdot}10^{23}$	1.14
	0.25	0.93	4.64	$0.94{\cdot}10^{23}$	1.14
	0.34	0.93	21.86	$0.99{\cdot}10^{23}$	1.16
RG 2	0.07	0.96	28.51	$0.97{\cdot}10^{23}$	1.15
	0.10	0.97	15.32	$1.00{\cdot}10^{23}$	1.15
	0.17	0.85	6.08	$1.20{\cdot}10^{23}$	1.15
	0.25	0.90	1.00	$1.27{\cdot}10^{23}$	1.15

5.2.2 Particle Size

The studied snow samples consist of particles with a large variation of particle diameters, where D_v varies from 80 μm for MM 1 to 775 μm for RG 2. Previous research has shown that α is generally expected to increase with decreasing particle size [97]. To assert this the α of snow is plotted in Fig. 5.10 as a function of D_v for fixed $H = 0.1$ m, where all measurement values were taken at $T \leq -12\,°$C. Therefore the effect of T is expected to be small between the samples. The figure also includes the least squares fit of the polynomial $\alpha = K_1 D_v^{K_2}$, where $K_1 = 0.05$ and $K_2 = -0.86$ gave the best fit. For this fitting, the MM 1 sample was excluded since this measurement had a diverging α.

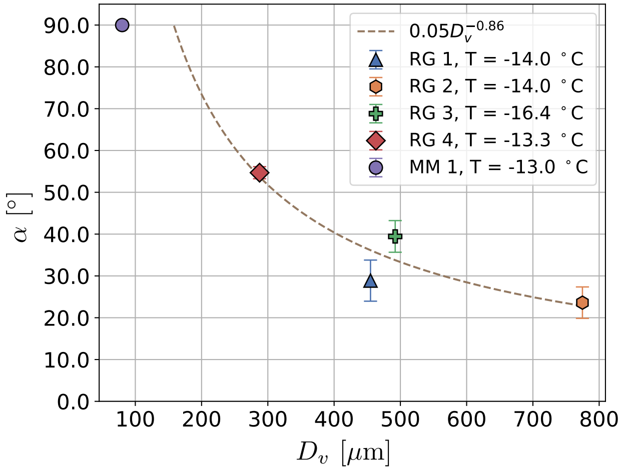

Figure 5.10: The α of snow as a function of D_v for the samples RG 1, RG 2, RG 3, RG 4, and MM 1 with $H = 0.1$, where the mean values of repeated trials are plotted with the error bars representing $\delta\alpha$. The dashed line is the least squares fitting of the RG samples.

5.2.3 Fall Height

Measurements of the α of snow were performed for varying H and as Fig. 5.9 depicts there are clear differences in the obtained α for varying H. Particles accelerate due to gravity, according to Newton's law of motion, when they fall through the sieves and towards the spherical base of the cylinder. This is not a linear acceleration because it is dependent on the drag force, which is a nonlinear function of Re_p, and for sufficiently high H, the particles reach its V_∞. Therefore, it is expected to see a nonlinear dependency of $\alpha(H)$, where changes of H can lead to large changes in α. However for sufficiently large H the α of snow for a given snow sample can appear constant and independent of further increases in H. Fig. 5.11a shows mean values of five measurement series of α as a function of H, which shows that the α of snow is having a nonlinear dependency on H. For example, only small changes between $H = 0.25$ m and $H = 0.34$ m are observed for the RG 1 sample, while significant changes occur for the studied samples when $H = 0.1$ m is either increased or decreased.

Fig. 5.11b shows the α of snow as a function of the predicted V_a for the same measurements as shown in Fig. 5.11a. The figure depicts that the estimated V_a is ranging from $1 - 1.5$ m/s for these measurements and α does not change for minor changes of V_a. For example the $V_\infty \approx 1.4$ m/s was almost reached for $H = 0.25$ for the RG 1 sample. When the H was increased to 0.34 m an almost identical α was measured.

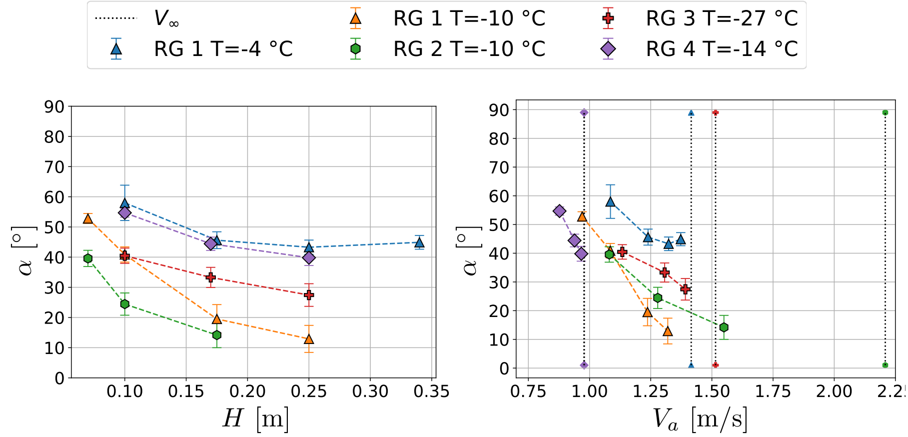

(a) The α of snow as a function of H.

(b) The α of snow as a function of predicted V_a.

Figure 5.11: The α of snow for measurement series at differing H, where the mean values of repeated trials are plotted with the error bars representing $\delta\alpha$.

5.2.4 The Cohesion Number

The experimental results imply that $\alpha = \alpha(D_v, \hat{\phi}_m, T, H)$, where especially strong dependencies on T and H were observed in the measurements. A difference between the snow samples was also observed, which was correlated to the range of D_v values, where a curve fit concluded that $\alpha \propto D_v^{-0.86}$. In Paper III this result was used to calculate that $\alpha \propto D_v^{-0.86} \propto Co^{0.86 \cdot 3/5} = Co^{0.52}$, which was rounded to $Co^{0.5}$. This calculation however assumes that V_a is independent on D_v which is a problematic simplification as highlighted in Section 5.1.2. Instead using that $\alpha \propto D_v^{-0.86}$ with Eq. (5.8) this eventuates that $\alpha \propto Co^K$, where $K = 0.86(2C + 5/3)^{-1}$ i.e., $0.15 \leq K \leq 0.32$, however the exact value of K is not constant and depends on Re_p. By simply fitting the experimental data of the α of snow to $\alpha = ACo^K$, the best fit obtained was $K = 0.32$, which then indicates that $V_a \propto D_v^{0.5}$. The result is heavily dependent on the obtained dependency on particle size shown in Fig. 5.10 and since only four data-points were used to obtain this dependency it is worth highlighting that the estimate is uncertain. In Fig. 5.12 the α of snow as a function of Co for this fit, together with the fit obtained in Paper III, and the experimental values in Paper III for $T < -12\,^\circ$C are depicted. Interestingly the Co for the MM 1 sample is close to $Co \approx 0.1$ and is significantly higher than α

of the other samples, which are in the interval $10^{-5} < Co < 10^{-3}$. Both fits in the figure capture the main trends seen for the experimental measurements, however there is also a spread in values, which potentially could be because the cohesive properties potentially change, depending on the particle shape, where now the same W is used independently on $\hat{\phi}_m$.

The Co was calculated incorrectly in Fig. 16 in Paper III, due to a programming error which caused incorrectly low values of Co. The error also caused the size dependency to be slightly incorrect. In Fig. 5.12 the correct calculation of Co is used where the measurements range between $10^{-5} < Co < 10^{-3}$ instead of $4 \cdot 10^{-6} < Co < 10^{-5}$, as was incorrectly calculated in Paper III. The aforementioned error also changes the fitting of $\alpha = ACo^{0.52}$, where $A \approx 4000$ has now been found using the correct calculation of Co. Despite this error, the conclusions made, and the trends observed for Co in Paper III still hold since the error mainly impacts the magnitude of the Co.

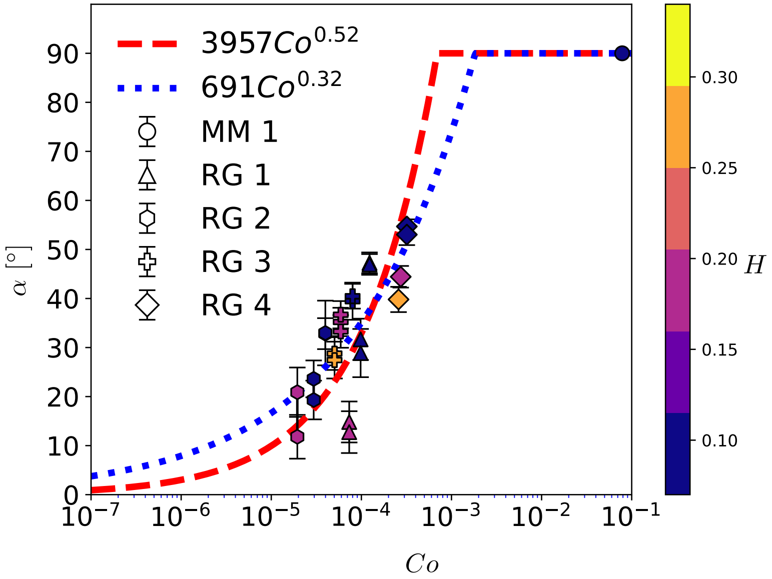

Figure 5.12: The α of snow as a function of Co for different snow samples with filled colors indicating H. The mean values of repeated trials are plotted with the error bars representing $\delta\alpha$. Dotted blue line shows best fit of $\alpha = ACo^K$ and dashed red line shows best fit of $\alpha = ACo^{0.52}$.

Chapter 6

Snow Contamination on Simplified Bluff Bodies

The studies in Paper II and Paper III were designed to measure properties of ice and snow. However these experiments did not account for external aerodynamics, which is expected to be the main mechanism for the transportation of ice particles and should potentially have a large influence on the snow contamination of cars. In Paper IV, ice particles in turbulent flows were studied by performing snow accumulation experiments on simplified bluff bodies. The experiments were performed in a climatic wind tunnel with a snow cannon, and a computational model was formulated to reproduce the experiments. The results in Paper IV highlight that unexpected accumulations of snow occurred in the experiments. In-field tests were therefore performed to test a hypothesis about differences in properties between natural snow and the machine made snow produced in the wind tunnel. Thus, the in-field tests presented in this chapter were performed after the publication of Paper IV.

6.1 Test Objects

A bluff body is, in this work, defined as a body that has large regions of separated boundary layers when subjected to an aerodynamic wind. All automotive vehicles (such as cars, trucks, and buses) are regarded as bluff bodies since they have large re-circulation regions in the rear, as well as behind vehicle wheels. These regions will be referred to as wake regions. For the present research topic, reliable experimental results on an industrial manufactured car are desirable. However, a fully detailed car is a complex system and there are many uncertainties on the aerodynamics surrounding a car. Examples of topics that still today have a lot of uncertainties are wheel aerodynamics [98] and under-hood flow [99]. There is also a great level of customization in the car industry, which increases variations between specimens that can further increase uncertainties. Therefore, simplified automotive bluff bodies were instead studied to reduce complexity and increase repeatability of experiments where a wedge geometry and the, so called, Ahmed body were studied. The bodies were chosen such that their simplicity reduce computational costs but still maintain the most important physics for snow contamination of cars. Fig. 6.1 shows the two bodies including arrows illustrating the wind direction, U_∞, as well as lines and annotations indicating geometrical lengths of the bodies. The wedge was built in stainless steel and the Ahmed body was built with clay, where a surface coating was added on the Ahmed body to yield similar surface properties as for automotive vehicles. The Ahmed body is a bluff body that was developed by Ahmed et al. [100] and the aerodynamics of this body has extensively been studied, both experimentally [100–102] and numerically [63, 101, 103]. Lienhart and Becker [102] performed Laser Doppler Anemometry measurements on the Ahmed body with slant angles β of 25° and 35° (see Fig. 6.1 for definition of β). The body was built with the same dimensions as in Lienhart and Becker [102] with three different rear parts, such that β equals 10°, 25°, and 35°. Previous studies have shown differences in the aerodynamics and the corresponding C_d for the body for these three slant angles [100], where it has also been seen that $\beta = 25°$ has been a hard configuration to simulate accurately. In Paper IV, $\beta = 35°$ was used for both the experiments and the simulations, which is also the focus in this chapter. Experiments on the Ahmed body with $\beta = 10°$ and $\beta = 25°$ are summarized in Appendix C.1.

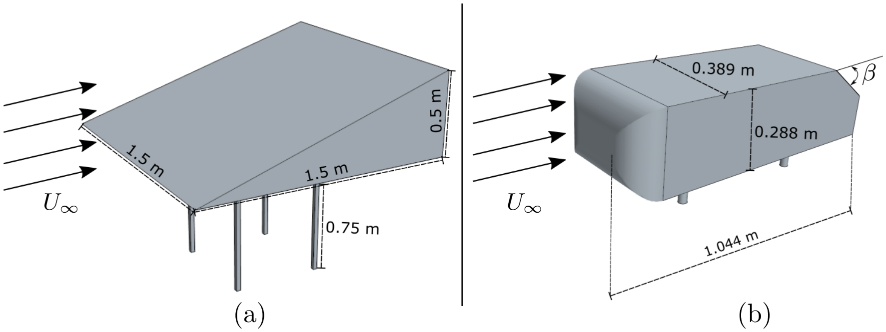

Figure 6.1: The simplified bluff bodies used in snow accumulation experiments. (a) The wedge and (b) the Ahmed body. Arrows illustrating air wind direction of U_∞ and lines depicting geometrical lengths of the bodies.

6.2 Wind Tunnel Experiments

Wind tunnel experiments were performed in the same climatic wind tunnel as described in Section 3.2 using the same snow cannon as shown in Fig. 3.2. Temperature was controlled in the tunnel at a constant air temperature of −15 °C, and the velocity of the air flow could be changed between 0 − 200 km/h.

The test objects were placed downstream in the middle of the test section approximately 2 m from the nozzle inlet. A test was begun by starting the air wind simultaneously as the flow of water and pressurized air to the snow cannon, and a measurement was performed for 30 min. Since the wedge was built with relatively long legs (750 mm) it was placed directly on the floor of the wind tunnel. The Ahmed body was built with shorter legs (50 mm) and was therefore placed on a 3x5 m metal table with height 0.7 m to avoid effects of floor irregularities on the results. Fig. 6.2 shows the Ahmed body with $\beta = 35°$ placed on the metal table in the wind tunnel. The replaceable rear part was taped together with the rest of the body to avoid gaps. The wedge was tested at $U_\infty = 70$ km/h, while the Ahmed body was tested at a range of U_∞ from 12 to 150 km/h. The previous studies on the Ahmed body by Ahmed et al. [100] and Lienhart and Becker [102] used $U_\infty = 144$ km/h at room temperature. This corresponds to a height-based Reynolds number Re_H of 768 000. An equivalent Re_H at an air temperature of $-15\,°\mathrm{C}$ was obtained at $U_\infty = 115$ km/h since ν_f of the air decreases with 20% when going from $T = 20\,°\mathrm{C}$ to $T = -15\,°\mathrm{C}$. Therefore, $U_\infty = 115$ km/h was used for the Ahmed body results shown in this chapter. Experimental results for other values of U_∞ on the Ahmed body are shown in Appendix C.2. The experimental conditions for the two bluff bodies are summarized in Table 6.1.

Figure 6.2: The Ahmed body with slant angle $\beta = 35°$ placed on the metal table in the wind tunnel.

Table 6.1: Experimental conditions for the two simplified automotive bluff bodies in the wind tunnel.

	The wedge	**The Ahmed body**
Size (l, w, h) [m]	1.5, 1.5, 0.5	1.044, 0.389, 0.288
Legs height [m]	0.75	0.05
U_∞ [km/h]	70	12-150
Re_H	810 000	80 000 - 1000 0000
Temperature [°C]	-15	-15
Trial duration [min]	30	30

Repeatability of the experimental trials was investigated by repeating the measurements for the Ahmed body three times. Since identical results were obtained for all three repetitions it was concluded that the testing time of 30 min was sufficiently long to obtain repeatable results. An example of the repeatability can be seen in Appendix C by comparing Fig. C.8 and Fig. C.3 that show two measurements at $U_\infty = 115$ km/h and $\beta = 35°$.

6.3 Computational Model

The experiments performed in the wind tunnel were reproduced using CFD in Simcenter STAR-CCM+ 2021.2. A turbulent flow and particle transportation were modeled using a Eulerian-Lagrangian approach with one-way coupling, where the air flow affects the particles, but the particles do not affect the air flow. This was carried out based on the assumption that the particle laden flow is dilute and therefore the effects particles have on the air flow was considered to be negligible. Particles were simulated as point sources, where particle-wall collisions were treated as binary events and thus was not resolved. Particle-particle collisions were not included in the simulations.

6.3.1 Turbulence Modeling

The IDDES $k-\omega$ SST turbulence model was used to simulate the wedge and the Ahmed body, which is a hybrid LES-RANS model. The model is a compromise between cost and performance, since LES is used for resolving large eddies in wake regions, while RANS is used near the turbulent boundary layer, where LES is too expensive. The domain was discretized using a hexagonal trimmed mesh with prism layers at the bluff body surfaces, where the numerical setup of the air flow was similar to what was used by Hobeika and Sebben [98].

The used time step Δt was chosen such that the Courant–Friedrichs–Lewy condition, $U_\infty \Delta t \leq \Delta x$, was met everywhere except where accelerations of the flow occurred at small regions at the front of the bodies.

Flow fields were averaged throughout the simulations, starting when the fluid flow was considered to be fully developed in time, and the fields were averaged for 5 s. Particles were injected in the domain 0.2 s after averaging started, which means the particles were simulated for 4.8 s. Details of the computational grid and the simulation setup for the wedge and the Ahmed body are summarized in Table 6.2.

6.3.2 Flow Assessment

The grid resolutions for both cases were evaluated in Paper IV by looking at the averaged ratio of resolved to total turbulent energy M, (see Eq. (2.50) for details). Fig. (6.3) shows M in an XY-plane at y=0 for both the wedge and the Ahmed body. M is close to unity in the rear wakes of both geometries. This means that the IDDES solver is dominated by resolving turbulent length scales in these regions, while for the regions close to sides and front surfaces, the solution is solved using a RANS approach.

Fig. 6.3 shows how the solver is resolving, versus modeling the turbulence in the domain, however, it is not necessarily a good indicator of how well resolved

Table 6.2: Computational setup for simulations on the wedge and the Ahmed body.

	The wedge	**The Ahmed body**
Cell count [Million]	23.1	16.5
Domain dimensions [m]	70x40x30	70x40x30
Prism layers	18	18
Maximum Surface Cell Size [mm]	4	4
Near wall prism height [μm]	20	15
U_∞ [km/h]	70	115
Δt [s]	2e-4	7e-5

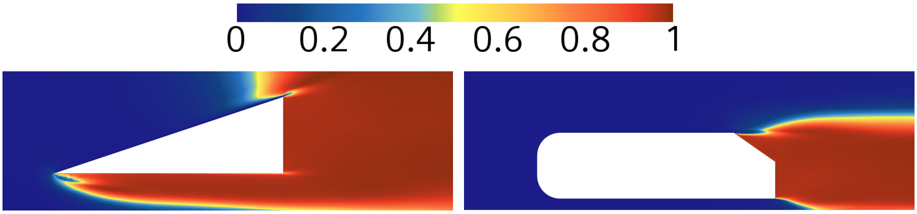

(a) The wedge.

(b) The Ahmed body.

Figure 6.3: Ratio of resolved to total turbulent energy M at XZ-planes for y=0.

the turbulent structures are (pointed out by Davidson [66]). To assert how well the turbulence is resolved, the minimum number of correlated points N_{D_i} for a specified direction D_i (see Eq. (2.52) for definition) was calculated for XY-planes and a XZ-planes on both bodies. Fig. 6.4 and 6.5 shows N_{D_i} for these planes, where the coordinate system is defined such that X, Y, and Z are in the stream-wise, vertical, and lateral directions respectively. In this analysis 150 samples of V_x, V_y, and V_z were taken using an interval of 20 ms, and $C_c = 0.1$ was used. The figures show that the flow is well resolved in X direction, where $N_{D_x} > 8$ for most volume cells. However, for both the Y and Z directions many cells only have an $N_{D_i} \in [3, 6]$, which is to be regarded as coarse. While this certainly can have an influence on the predicted details of the aerodynamics, it is not obvious how the particle trajectories will be affected. A test was performed on the wedge to refine the wake by decreasing the cell size to 50%. While this resulted in a 280% cell count increase, no change was observed in comparison to the particle deposition results shown in Paper IV. Therefore the original case was used for the results in this chapter.

The simulated results for the Ahmed body were further evaluated by comparing them to previous experimental and numerical studies. The reader is referred to Fig. 5 and Fig. 6 in Paper IV for details.

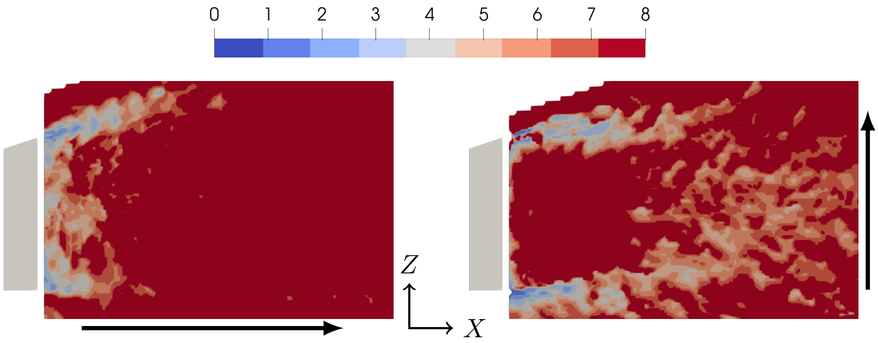

(a) XZ-Plane, N_{D_x} and N_{D_z} to the left and right, respectively.

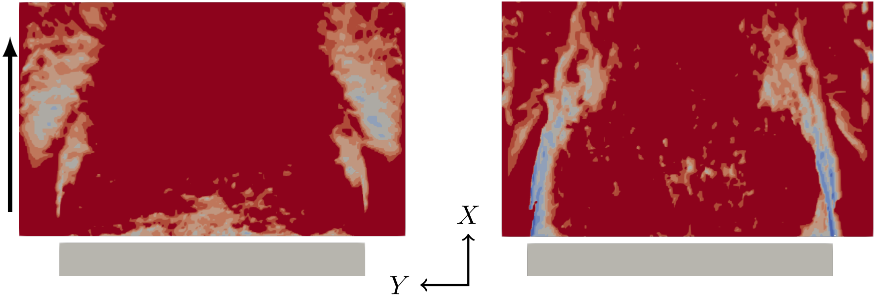

(b) XY-Plane, N_{D_x} and N_{D_y} to the left and right, respectively.

Figure 6.4: 2D Planes in the wake of the wedge colored by N_{D_i} for the directions X, Y, and Z. Thick arrows illustrating the analysis directions D_i.

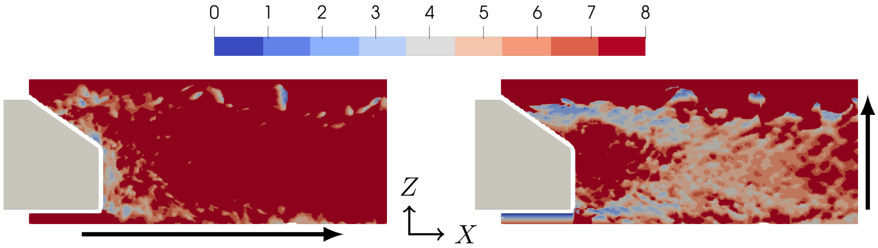

(a) XZ-Plane, N_{D_x} and N_{D_z} to the left and right, respectively.

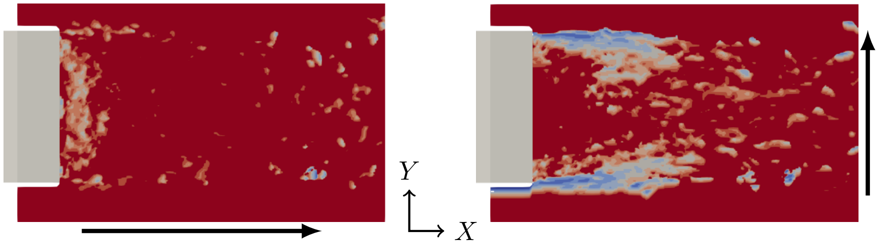

(b) XY-Plane, N_{D_x} and N_{D_y} to the left and right, respectively.

Figure 6.5: 2D Planes in the wake of the Ahmed body colored by N_{D_i} for the directions X, Y, and Z. Thick arrows illustrating the analysis directions D_i.

6.3.3 Particle Forces and Properties

The particle trajectories were calculated by solving Eq. (2.65), where the following forces were accounted for:

- The drag force using Haider and Levenspiel correlation [72] for C_d.
- The shear lift force using Sommerfeld correlation [104] for C_{LS}.
- The gravity force.
- The pressure gradient force.
- Turbulent dispersion modeled by adding fluctuations based on Gosman and loannides [105].

A classification of the machine made snow produced by the snow lancer has been shown in Section 5.1.1 (see MM 1 sample), where it was seen that the snow consisted of small spherical ice particles. A range of particle sizes were simulated by fitting the particle size distribution shown in Fig. 5.4a to a Rosin-Rammler distribution, where D_p ranged from $9 - 150\,\mu$m. The density of ice was used as the particle density in the simulations, i.e., $\rho_p = 917\ kg/m^3$. The median circularity $\hat{\phi}$ from the snow classification was used as a value for ϕ when calculating C_d, where $\phi = 0.95$ was used in the simulations, which only causes a minor effect of non-sphericity.

6.3.4 Modeling of Ice Particle Collisions with Walls

Particle-wall collisions were modeled as illustrated by the flow chart shown in Fig. 6.6. When a particle-wall collision was detected, a resuspension criterion was checked, causing the particle to bounce directly, if predicted to be resuspended. If a particle was not predicted to be resuspended it was checked if the particle had been predicted to stick or bounce, depending on the impact velocity in the normal direction $V_{i,n}$. If a particle bounced, a virtual wall model was used to model roughness at the impact, causing the re-bounce angle to be randomly rotated towards the normal direction. The rebound velocity was damped according to the coefficient of restitution in normal and tangential direction e_n, e_t depending on D_p, $V_{i,n}$, and the impact velocity in tangential direction $V_{i,t}$.

Resuspension of particles can occur due to multiple different aerodynamic forces present at proximity to a wall. A particle can re-enter the fluid flow by either direct detachment in normal direction, or due to initial rolling or sliding (further details can be found in Henry and Minier [70]). Resuspension of micron-sized adhesive particles is most likely to be caused by a rolling mechanism [106]. The resuspension criterion used in the simulations were derived based on the assumption that rolling is the main mechanism for resuspension. A particle is predicted to be resuspended if the acting torque on the particle from the aerodynamic flow M_f and the torque caused by gravity M_g, is greater or equal to the adhesive resistance torque for rolling M_a,

$$M_f + M_g \geq M_a, \tag{6.1}$$

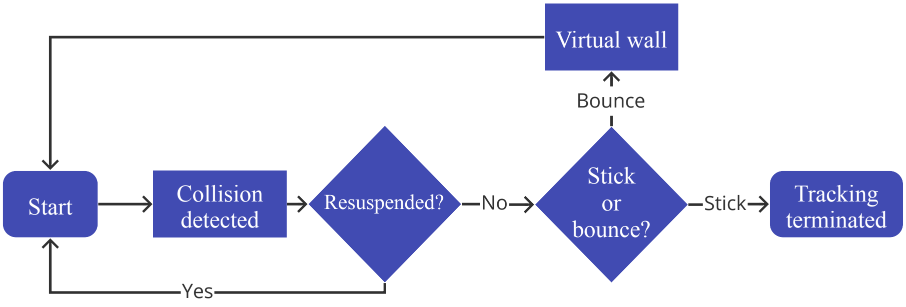

Figure 6.6: Flow chart for the modeling of particle-wall collision.

where M_a is defined in Eq. (2.35). Assuming that the particle at the wall is at equilibrium contact ($R^* = 0.5D_p$ and $a \approx a_0$), this equation can be combined with Eq. (2.24), Eq. (2.36) which simplifies as

$$M_a = \frac{1}{4}\pi W D_p a_o \frac{\Delta\gamma}{\gamma}, \tag{6.2}$$

The torques caused by the near wall drag force in the parallel direction to the wall ($F_{D,||}\frac{D_p}{2}$) and the torque caused by asymmetry of the flow $M_{||}$ are estimated to be the main contributions for M_f. These were calculated as,

$$M_f = F_{D,||}\frac{D_p}{2} + 1.4F_{D,||}\frac{D_p}{2} = 2.4F_{D,||}\frac{D_p}{2}, \tag{6.3}$$

where $M_{||} = 1.4F_{D,||}\frac{D_p}{2}$ was used based on the work by O'Neill [73] (see Eq. (21) in Henry and Minier [70]). Using boundary layer theory, the velocity at the center of the particle, which determines the magnitude of $F_{D,||}$, was calculated based on the friction velocity at the impact point of the wall u_τ using the Reichardt near wall velocity profile for $u^+(y^+)$ [107]. To determine if a particle will be resuspended, it is sufficient to find the smallest particle diameter when resuspension will occur D_c, for a given u_τ. This was done by numerically searching for D_c such that $(M_f + M_g) - M_a \leq \epsilon$, where ϵ is a small threshold value. Fig. 6.7 shows the found D_c as a function of u_τ, both when the acting torque is M_f as well as the sum $M_f + M_g$. M_g was calculated for the case when a particle is adhered to a vertical wall. Only for large diameters ($D_c > 200\,\mu$m), effects of gravity were seen and since the largest simulated D_p was 150 μm, the contribution of gravity was omitted. The figure also includes a curve fit for

$$D_c = a u_\tau^b, \tag{6.4}$$

where $a = 77.7\,\mu$m and $b = -1.34$ was the best found fit when searching for D_c, such that $M_f - M_a \leq \epsilon$. Since it is sufficient to know $D_c(u_\tau)$, this simplified equation was used as resuspension criterion instead of solving Eq. (6.1).

Effects of collisional melting was neglected in the simulations when calculating e_n and e_t, since the machine made snow consists of such fine ice particles. As can be seen in Fig. 4.8a, extrapolations down to $D_p \lessapprox 150\,\mu$m predicts that effects of collisional melting should only take place for $V_i > 20 - 30$ m/s. The removal of the collisional melting regime is further motivated by the experimental results where no snow is observed to accumulate at surfaces where V_i is expected to be highest (for example front surface). The e_n and e_t were defined as

$$e_n = e_{qe}\sqrt{1 - \left(\frac{V_s}{\max(V_{i,n}, V_s)}\right)^2}, \tag{6.5}$$

and

$$e_t = e_{qe}\sqrt{1 - \left(\frac{V_{c,t}}{\max(V_{i,t}, V_{c,t})}\right)^2}, \tag{6.6}$$

where V_s is the same as in Eq. (4.1), $V_{c,t}$ is the critical velocity in tangential direction, and e_{qe} is the coefficient of restitution due to quasi-static damping in the collisions. $V_{c,t}$ is defined as the highest velocity at which all tangential components in a collision will be lost and was related to V_s in Appendix D under the assumption that rolling is the main mechanism for adhesive losses in tangential direction. $e_{qe} = \sqrt{1-\xi} = \sqrt{1-0.15} \approx 0.92$ was used based on Eq. (4.13). The material properties W and E^* defined the adhesive interactions for this modeling. These properties depend on the wall material of the bluff bodies as well as local properties at contacts such as humidity, roughness, or potential icing at the surface. To simplify the analysis a conservative modeling approach was chosen such that the modeling was performed using high adhesive interactions by using interaction properties for ice-ice contacts with $W = 0.218$ J/m^2 and $E^* = 5.4$ GPa.

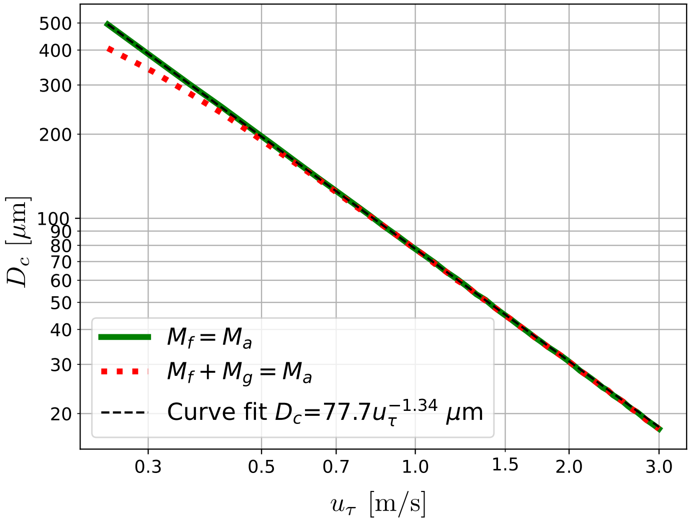

Figure 6.7: The critical particle size for resuspension D_c, as a function of friction velocity u_τ. Green solid line showing resuspension criterion solved for $M_f = M_a$, and red dotted line showing the criterion solved for $M_f + M_g = M_a$. Black dashed line showing curve fit to the green line.

6.4 Data Averaging and Interpretation

The computational model is transient which means that the particle trajectories and the air flow are evolving over time. The results from the simulations are therefore time-averaged and analysis is based on these time averages. For the particle simulations two results are of interest; the time-averaged impact rate per area J_i, and the time-averaged deposition rate per area J_a. The difference is that J_i includes all particle-wall collisions, while J_a only includes particles predicted to stick, which means that $J_a \leq J_i$. From these quantities the collision efficiency was defined as,

$$\kappa = \frac{J_a}{J_i}. \tag{6.7}$$

Since u_τ can also vary while the simulations are running a maximum time-average was calculated as

$$\hat{u}_\tau = \overline{u_\tau} + 3\sigma_\tau, \tag{6.8}$$

where $\overline{u_\tau}$ is the time-averaged u_τ and σ_τ is the standard deviation of u_τ. However, since the turbulence model solves the near wall flow using an unsteady RANS model, $\hat{u}_\tau \approx \overline{u_\tau}$ and σ_τ is expected to be close to zero.

All the averages above were calculated for each timestep, but properties for particle-wall collisions were only saved by sampling at 250 Hz, in order to save computational resources. This chapter shows statistics from D_p of this sampling for the different surfaces.

6.5 In-Field Test Procedure

In-field tests on the wedge and the Ahmed body were performed to assert how the snow type affects the accumulation pattern. The bluff bodies were placed on a car trailer that was pulled by an electric compact sport utility vehicle (Volvo XC40 Recharge) to mimic a situation where the bluff bodies are exposed to a cloud of natural snow. Another vehicle of the same model was driven in front of the pulling vehicle (within proximity) to increase the generated snow cloud present near the surfaces of a bluff body. The wedge was mounted directly onto the trailer floor, similar as in the wind tunnel. However, for the in-field tests, legs with a height of 400 mm instead of 750 mm were used to ensure that the wedge was in the wake of the pulling vehicle. The Ahmed body was placed on a metal table with dimensions 1x3 m. The bluff bodies were positioned such that the front of the bodies were 3.5 m behind the rear of the pulling vehicle. Fig. 6.8 shows photographs of the test setup for the two bluff bodies.

The tests were performed on a test track in Sweden at ambient conditions by driving both vehicles in close proximity for 100 km. Since the ambient conditions changed between days, multiple tests were performed on each body, where the experimental conditions such as driving speed and distance also were varied between tests.

(a) The wedge placed on a car trailer.

(b) The Ahmed body placed on a car trailer including a 1x3 m metal table.

Figure 6.8: Photographs of the bluff bodies placed on a car trailer during the in-field tests on the two bodies.

6.6 Results and Discussion

The wind tunnel results are compared here to the CFD simulations, where each test object is compared separately. In-field observations of both test objects using a car trailer are shown followed by an overall discussion of the results. Emphasis in this section is on the depositions observed on side and rear surfaces of the two bluff bodies. More details about the simulation results can be seen in Paper IV, where it is also highlighted that snow is predicted to deposit at areas of the front surfaces on both bodies. This is not observed in the experiments, potential reasons for this are also discussed in Paper IV. Since simulations were only performed for the Ahmed body with $\beta = 35°$ at $U_\infty = 115\,\text{km/h}$, the experimental results from the wind tunnel for the same conditions are shown in this section. Wind tunnel results for the other slant angles can be found in Appendix C.1 and results for $\beta = 35°$ at varying velocities are included in Appendix C.2.

6.6.1 The Wedge: Machine Made Snow

In the experiments, most of the snow was depositing and accumulating at the rear surface of the wedge where three distinct regions of snow accumulation have been observed; to the left, right, and at the center. The regions are rather distinct where almost no deposition occurs between the regions. The CFD simulations aimed to reproduce the results from these experiments show a similar trend where 75% of the total deposition occurs on the rear surface. Fig. 6.9 shows the rear surface of the wedge with a photograph from a wind tunnel trial (a), together with the predicted J_a from the CFD simulation (b). Red dashed lines were included in the photograph to highlight regions of higher snow deposition. While the simulations do predict this trend, that most snow is depositing in the rear, deviations can be seen in the figure between the experiments and the simulations. Specifically, the simulations predict a more dispersed deposition. There are regions of higher J_a to the left, right, and center, similar to the experiments, however not as distinct as in the experiments. Most of the tracked particles that did collide with the rear surface, did so in the center of the surface, similar to the obtained experimental result, which can be seen by looking at the averaged impact rate J_i on the rear surface (shown in Fig. 6.10).

The aerodynamic result from the wedge reveals an interesting flow phe-

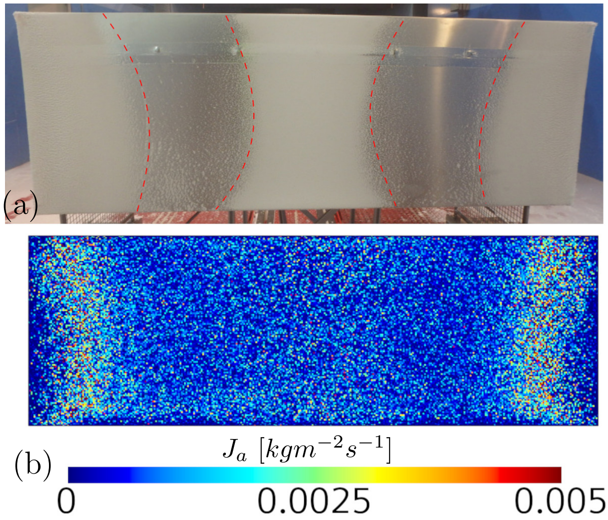

Figure 6.9: Deposited snow on the rear surface of the wedge. (a) shows the wind tunnel results including dashed red lines that highlight regions of increased snow deposition and (b) shows the averaged deposition rate of ice particles J_a from the CFD simulation of the wedge.

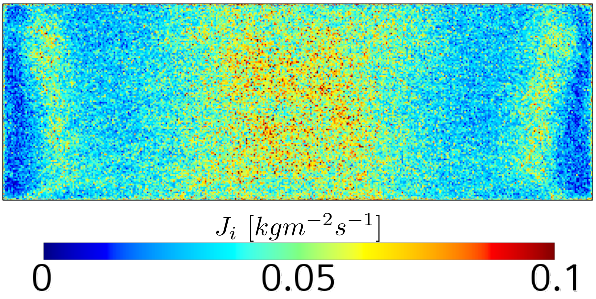

Figure 6.10: The averaged impact rate of ice particles J_i at the rear surface of the wedge.

nomenon where trailing vortices are present in proximity to each side surface of the wedge. These vortices start at the front tip of the wedge and move diagonally upwards as they travel towards the rear. Fig. 6.11 shows an isometric front view of the wedge where estimations of the left vortex core line [108] is depicted as a tube in the figure. Arrows indicate the rotation of the vortex, and three constrained planes show the contours of the mean velocity in each plane. Surfaces of the wedge were shown with $\hat{u}_\tau$, where a region with low values of $\hat{u}_\tau$ can be seen at the surface just above the vortex core. In this region $\hat{u}_\tau$ is so low that $D_c \geq 150\,\mu$m, where any of the simulated particles that adhere on this surface are not expected to be resuspended. In practice however, the vortex rotation might be so strong that only particles with low values of St (small particles) might be able to be transported to the region of low D_c. In the experiments, snow was seen to deposit in this region of low values of $\hat{u}_\tau$ and the simulations also predicted deposition at the same region. Fig. 6.12 shows an image from the wind tunnel experiment depicting the left side surface of the wedge (a), and the predicted J_a from the simulations of the left side surface (b).

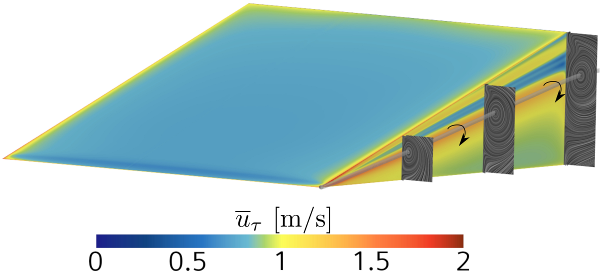

Figure 6.11: Illustration of trailing vortex alongside the left side of the wedge with three constrained planes showing mean velocity contours in each plane. The surfaces are colored with the time-averaged friction velocity $\hat{u}_\tau$. Arrows show the rotational direction of the vortex.

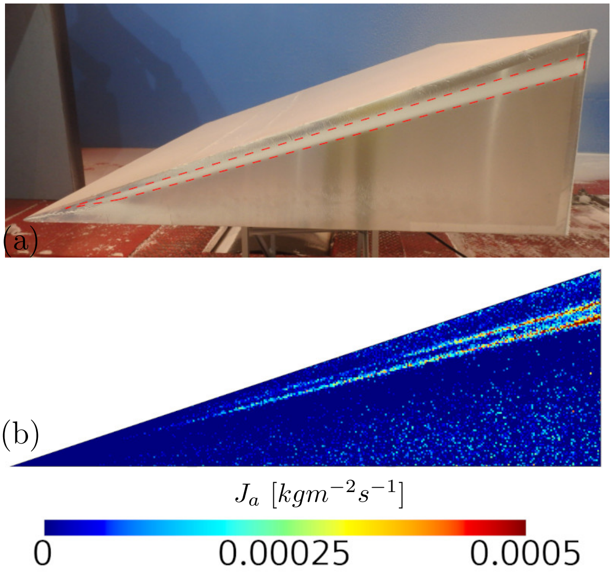

Figure 6.12: Deposited snow on the left side surface of the wedge. (a) shows the wind tunnel results including dashed red lines that highlight regions of increased snow deposition and (b) shows the averaged deposition rate of ice particles J_a from the CFD simulation of the wedge.

6.6.2 The Ahmed Body: Machine Made Snow

While the snow deposition and accumulation on the wedge was restricted to certain distinct surface regions, snow accumulated on the Ahmed body over a large area, where in practice all surfaces except the front surface received snow deposition. Fig. 6.13 shows front and rear surfaces of the Ahmed body, where a photograph of a wind tunnel trial is shown in (a) and the predicted J_a from the CFD simulation is shown in (b). Here it can be seen that the simulation predicts deposition in the front, which is not occurring in the experiments, however the maximum value of $\kappa = 3 \cdot 10^{-4}$ at this surface means that sticking is a rare event compared to the amount of colliding particles. In the experiments there are differences in magnitude of accumulated snow, even though the rear is completely covered in snow, a similar pattern as for the wedge is obtained where more snow accumulates on the left, right, as well as the center of the straight rear surface. A curved line of higher snow accumulation can also be seen in Fig. 6.13, which occurs in the same place as the simulation predicts a reattachment line. Fig. 6.14 shows an isometric rear view of the Ahmed body where a calculation of the reattachment line is shown in white at the rear surface. The figure also includes two constrained planes displaying the mean velocity contours near the surface and the surfaces are colored with $\hat{u}_\tau$.

Fig. 6.15 shows the left side surface of the Ahmed body where a photograph from an experimental trial is shown in (a) and the predicted J_a from the CFD simulation is shown in (b). In the experiments, snow began to deposit on the Ahmed body directly after the front curvature surface, where almost the entire surfaces were covered in snow. An exception is a rear triangular area behind

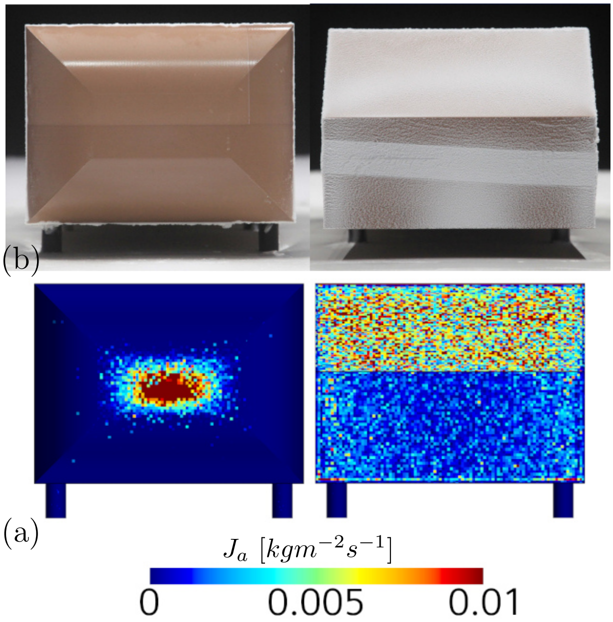

Figure 6.13: Accumulated snow on the front surface (to the left) and rear surface (to the right) of the Ahmed body for $U_\infty = 115$ km/h.

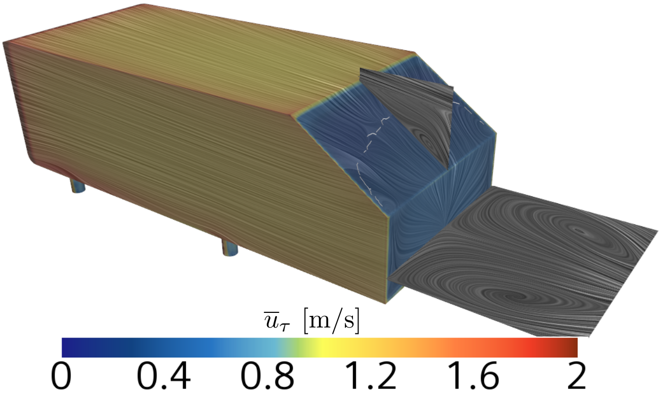

Figure 6.14: Isometric rear view of the Ahmed body with two constrained planes showing mean velocity contours. The surfaces are colored with the time-averaged friction velocity $\hat{u}_\tau$. White lines on rear slant surface show calculated reattachment lines.

the rear legs that did not receive snow deposition.

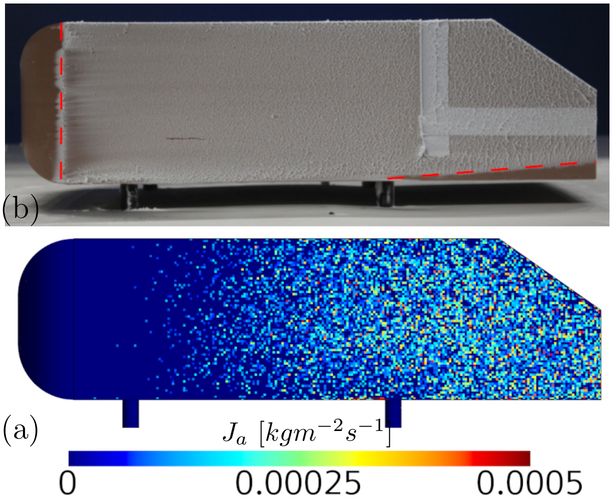

Figure 6.15: Deposited snow on the left side surface of the Ahmed body. (a) shows a photograph of a wind tunnel trial with dashed red lines indicating regions of increased snow deposition and (b) shows J_a from the CFD simulation on the Ahmed body.

6.6.3 Statistics of Particle Sizes

Fig. 6.16 shows statistics of median and spread of the sampled D_p for different surfaces for both the wedge and the Ahmed body. The boxes show the spread of one quartile, the bars show spread of two quartiles, and points depict outliers outside the bars. For both test objects almost all particle sizes tended to collide at front surfaces, while only smaller particles tended to collide with side and rear surfaces. For the wedge, only particles with $D_p \lesssim 30$ μm tended to collide with the side surfaces of the wedge, possibly because only these sizes of particles can follow the rotation of the trailing vortices on each side surface, and a smaller subset of these stuck on the sides. For the Ahmed body larger particles tended to collide with the side surfaces however only a small subset of these stuck to the sides where $D_p < 20$ μm, which is significantly smaller than D_c on this surface.

The statistics depict that only a subset of particles is predicted to adhere on surfaces and implies that the size of the smallest particles in a snow sample should have a large influence on the resulting snow deposition pattern. Since the results in Chapter 5 show that the wind tunnel snow is significantly finer than natural snow it is reasonable to assume that natural snow should not yield the same snow patterns as obtained in the wind tunnel. This reasoning led to the hypothesis that snow should not accumulate on side surfaces of either of the bluff bodies if experiments would be repeated by changing to natural snow instead of machine made snow. The hypothesis was tested using the in-field tests since it's not possible to perform the same wind tunnel tests with natural snow.

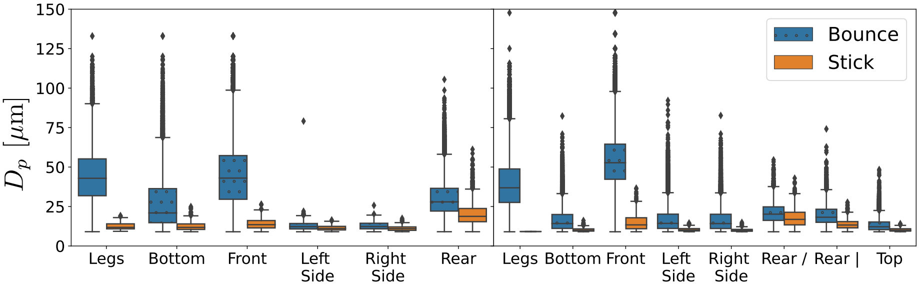

(a) The wedge (b) The Ahmed body

Figure 6.16: Statistics of particle diameters D_p for particle-wall collisions on different surfaces in the simulations. Blue boxes show statistics for particles both sticking and bouncing, and green boxes show statistics for particles sticking.

6.6.4 In-Field Observations

The in-field tests were performed over several consecutive days were the ambient conditions varied (from $T = -5\,^\circ$C to $T = -25\,^\circ$C), as well as the properties and depth of the snow layer on the test track. As described in Section 6.5 multiple tests were performed over the testing days, however, this section does not aim to report all results obtained from these tests. Instead, characteristic observations made from the tests that are considered relevant in comparison to the wind tunnel results will be focused on here. For all the in-field tests on the bluff bodies, no snow was observed to deposit on neither front, side, or top surfaces. Snow was only observed to accumulate at rear surfaces for all the performed tests.

Fig. 6.17 shows two tests with the wedge at driving speeds 40 km/h and 70 km/h. The general difference between the tests is that more snow is observed to accumulate at 40 km/h compared to 70 km/h, while the overall snow pattern obtained was similar. This effect of higher snow accumulation at lower speeds was also observed on a vehicle driving on a snowy road, which was shown in Chapter 3. Snow deposited at the left and right-side surface in a similar way as in the wind tunnel, while less snow deposited on the rear center of the two objects. For the 70 km/h case only small amounts of snow deposited at the rear center, both at the top part of the surface as well as the bottom part. For the 40 km/h more snow deposited overall on the rear surface and a larger area of snow deposited at the center.

Fig. 6.18 shows photographs of the snow deposition from three in-field tests with the Ahmed body where an isometric rear view is shown to the left and a rear view is shown to the right. These tests were performed at a driving speed of 70 km/h for a distance of 100 km. Similar as for the wedge, snow was only observed to deposit on the rear surface where most snow deposited on the rear straight surface. Since the tests were performed at 70 km/h they should be compared to the wind tunnel results for the same velocity, however only small deviations were observed in the wind tunnel between 115 km/h and 70 km/h (see Fig. C.7- C.8 in Appendix C.2). The results shown in Fig. 6.18

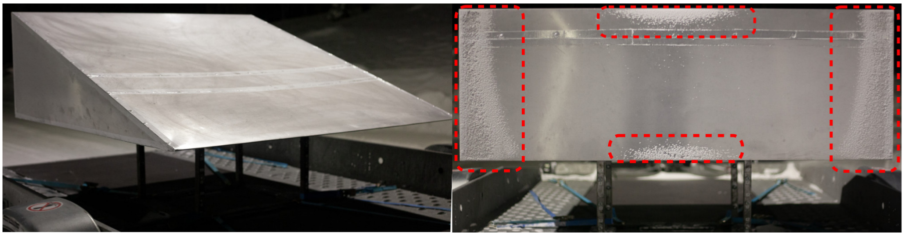

(a) Test 1 with driving speed 40 km/h for 50 km at $T = -25\,^{\circ}\mathrm{C}$.

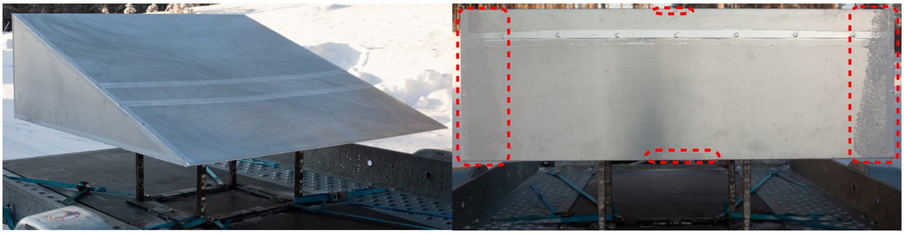

(b) Test 2 with driving speed 70 km/h for 100 km at $T = -20\,^{\circ}\mathrm{C}$.

Figure 6.17: Photographs of in-field tests for the wedge showing two different tests. Figures to the left shows isometric front view and to the right is shown a rear view.

highlight some of the challenges when performing in-field tests. For Test 2 (Fig. 6.18b), some of the deposited snow in the rear fell off while driving, causing the observed irregular snow pattern. In Test 3, snowfall occurred at the end of the tests while parking to take photographs. Therefore, some of that snowfall can be seen on the top surface of the Ahmed body in Fig. 6.18c, however no snow was observed to have deposited during the test on this surface. Some irregularities can also be seen in Fig. 6.18c at the rear straight surface, where the rear surface was not cleaned properly due to fat present on a snow brush. The observed accumulation pattern on the rear slant angle was different than what was observed in wind tunnel experiments for $\beta = 35°$. The obtained v-shaped patterns have some similarities to what was observed for $\beta = 25°$ (see C.2 in Appendix C.1).

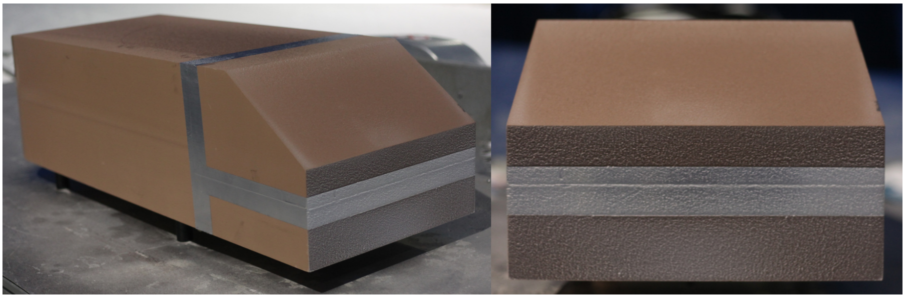

(a) Test 1, $T = -8\,^{\circ}\mathrm{C}$.

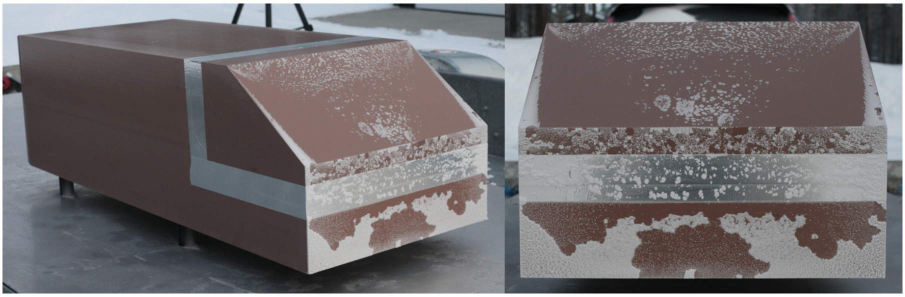

(b) Test 2, $T = -25\,^{\circ}\mathrm{C}$.

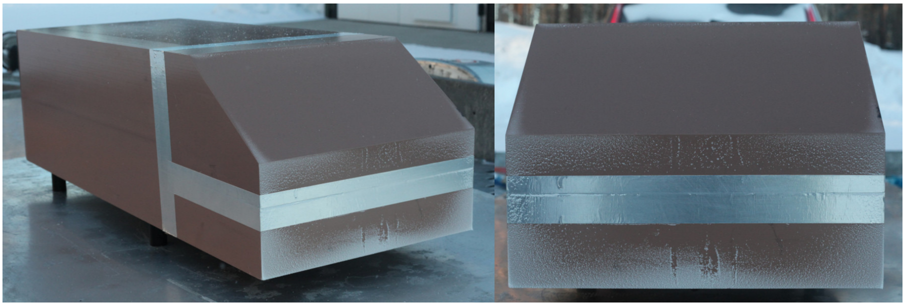

(c) Test 3, $T = -8\,^{\circ}\mathrm{C}$.

Figure 6.18: Photographs of in-field tests for the Ahmed body showing three different tests driving 100 km at 70 km/h. Figures to the left show isometric rear view, and to the right a rear view is shown.

6.6.5 Discussion and Conclusions

The wind tunnel results depict how snow accumulation is affected by aerodynamics of bluff bodies. Specifically, snow is observed to deposit and accumulate near rear wake regions and reattachment regions where air flow velocities are expected to be low, causing low velocities of impact for ice particles.

The computational model captures the main snow deposition patterns seen in the experiments, however deviations are observed. Specifically, snow is predicted to stick at front surfaces in the simulations, which is not occurring in the experiments, which implies that some parts of the transport mechanism of the particles might be missing in the modeling. There are several possibilities for these which is also discussed in Paper IV.

Both the wedge and the Ahmed body had snow accumulating on their side surfaces, a result that can be viewed as unexpected given that this type of snow deposition is generally never obtained on a car when driving on a snow-covered road. The statistics from the simulations revealed that only a subset of the smallest particles had been predicted to stick on these side surfaces. These particles are to be viewed as extremely fine and when comparing to the snow characterization in Chapter 5, they are not expected to be present for natural snow outdoors, which imply that the machine made snow produces an unnatural snow pattern. This motivated the performed in-field tests of the simplified bluff bodies where no snow was observed to adhere on any of the side surfaces, neither for the wedge nor the Ahmed body. Those tests confirm the hypothesis that the machine made snow is causing an unnatural snow pattern in the wind tunnel. Concerns can however be raised for the comparison between the wind tunnel experiments and the in-field tests since not only the snow type is different but also the experimental setup and conditions. The bluff bodies were positioned in the rear wake of an SUV (3.5 m behind), which affected the airflow, and potentially also the particle trajectories, as well as the collisional velocities. Future tests using a different experimental setup would therefore be interesting to further assert the hypothesis regarding the machine made snow.

Chapter 7

Summary of Papers

7.1 Paper I

Modeling of dry snow adhesion during normal impact with surfaces

Aim: Examine at which velocities dry ice particles and agglomerates of ice particles are theoretically expected to stick during a normal collision with a massive wall.

Summary: A computational framework was used combining three contact models; the JKR model in the normal direction, the adhesive sliding model as used by Marshall [51], and a novel rolling model, where the resistance of rolling was assumed to be due to adhesion. The paper reports on an analytical solution to single-particle collisions combined with simulations of small and large agglomerates. The analysis predicts that single-ice particles are more likely to adhere to a polymer wall than a glass or steel wall. For the adhesion models used, the effective Young modulus, E^*, is predicted to be an important interaction property. It was also found that the maximum obtained stick velocity increased with increased coordination numbers in an agglomerate. This was explained by the higher amount of energy losses caused by sliding and rolling at the impact, and the increase in energy loss for increasing agglomerate size is significantly larger than the increased kinetic energy.

7.2 Paper II

Collisional damping of spherical ice particles

Aim: Experimentally quantify the coefficient of restitution, e_n, of millimeter-sized ice particles and propose a novel collisional damping model.

Summary: Experiments on millimeter-sized ice particles colliding with massive walls were performed. Different temperatures and wall materials were tested. It was found that the obtained velocity-dependency was similar to what was obtained for larger particles in the experimental study by Higa et al [42]. It was also found that the different wall materials yielded different e_n, where experiments with the hardened glass wall caused the lowest values of e_n and experiments with a polymer wall had the highest e_n.

Based on the experimental results, the previous experimental study by Higa et al [42], and a study proposing a model for collisional fusion [31], a novel model for e_n of ice particles was proposed, where the damping in a collision was explained by the collisional premelting of a liquid layer, and viscous damping caused by this premelted liquid layer. This model was found to capture the temperature and material dependencies obtained in the experiments. The size dependency of e_n presented by Higa et al. [42] was also captured by the novel model.

7.3 Paper III

Angle of Repose of Snow: An experimental study on cohesive properties

Aim: Develop an experimental procedure to measure the angle of repose of snow α and quantify the variables affecting this angle.

Summary: A wide set of experimental results measuring α were produced for seven different snow samples. The results show that α depends on the fall height, the temperature, and the particle size. Analysis of the temperature dependency shows that it follows an Arrhenius relation and confirms previous work studying α of snow. For low temperatures, $T \leq -12\,^{\circ}\mathrm{C}$, α appears to be independent of T. With increasing fall height the angle decreases, but the dependency is found to be nonlinear. When ice particles are predicted to have reached terminal velocities, no change of α is observed with increasing fall height. It is also found that α increases with decreasing particle size, where the machine made snow has the finest particles, and $\alpha = 90^{\circ}$ for all measurements. A dimensionless number, the cohesion number Co, was proposed in the paper and it was found that this number reflects most of the dependencies observed.

7.4 Paper IV

Snow Contamination of Simplified Automotive Bluff Bodies: A comparison between wind tunnel experiments and numerical modeling

Aim: Investigate snow contamination on simplified automotive bluff bodies by performing wind tunnel experiments and formulate a computational model that reproduces these experiments.

Summary: Experimental results from wind tunnel experiments at −15 °C on two different bluff bodies were presented together with a computational model aiming to reproduce the experiments. The computational model consists of an adhesion model and a resuspension criterion, and particles were tracked by applying forces on the particles from an aerodynamic simulation. The experimental results show that snow deposited on surfaces in wake regions of the two bodies. The aerodynamic simulations indicate that the deposition seems to increase at re-circulation regions on both bodies. The experimental results were compared to the predicted deposition rate from the adhesion model where both similarities and deviations were observed. Specifically, it was seen that the simulations manage to predict characteristic snow patterns obtained on side surfaces of the bluff bodies, as well as the overall rear accumulation. The simulations do however deviate from the experiments by predicting a more scattered deposition at the rear surfaces than what is seen in the experiments on both bodies.

Chapter 8

Concluding Remarks

This thesis addressed snow contamination of cars, motivated by an increased need for sensor availability in the automotive industry. The aim was to investigate adhesive properties of ice particles, in order to increase the understanding of how snow adheres on exterior vehicle surfaces. To achieve this, mechanistic models for particle collisions were formulated and then used in a complete numerical approach to predict snow contamination of aerodynamic bluff bodies.

Single ice particle collisions were studied in Paper I and II, where two models for ice particle collisions with massive walls were combined into a regime map; a low velocity model based on the JKR theory, modeling intermolecular interactions, as presented in Paper I; and a high velocity model, predicting the damping due to collisional melting, which was developed in Paper II. With this regime map, analysis of dependent variables such as wall material, particle size, and temperature were performed. The size dependency predicts that collisional melting might not be a major mechanism for the snow contamination of cars since the estimated critical velocity for these ice particles are higher than the expected driving speed of a vehicle. In both the wind tunnel and in-field experiments it was found that deposition of snow is only observed at regions where the collisional velocities are expected to be low. This further indicates that collisional melting might not be a major mechanism for the snow contamination of cars at least for sufficiently low temperatures.

The experimental results for the angle of repose of snow in Paper III were interpreted using the cohesion number, which was defined based on the single ice particle collision model at low velocities. With this dimensionless number, observed dependencies on the angle of repose of snow could be explained. However, the model fails to acknowledge how the cohesive properties of snow change with temperature. The work in Paper III highlights some of the complex properties of snow and ice that coming from the fact that the studied material is in proximity to its melting point. It was shown that for significantly low temperatures, the cohesion is constant and independent on temperature, while for elevated temperatures there is a clear relationship between the angle of repose and the temperature that follow an Arrhenius relation. The experimental results in Paper III highlight that the angle of repose of snow can vary greatly even for the same snow sample and is a complex buildup phenomenon. The angle should be interpreted as a representation of a certain accumulation scenario rather than a fixed material property. The study also highlights that the effects of drag force and particle size are crucial and should not be neglected when simulating buildup of snow, for example using a particle simulation software.

The final part of this thesis is addresses snow contamination of simplified bluff bodies. In Paper IV results from wind tunnel experiments on the simplified bodies were compared to simulations that replicate the experiments using a computational model. The comparison shows that certain deposition phenomena are well captured by the computational model, where it is seen that snow is predominately accumulating in the rear of both the studied bodies. Deviations were also highlighted between the experiments and simulations, where the simulations in general predict more dispersed snow depositions than what is seen in the experiments.

The combined results of experiments and numerical simulations on the simplified bluff bodies show that the unexpected snow accumulation on the Ahmed body could be caused by the fact that machine made snow was used. The machine made snow from the used climatic wind tunnel was already in Paper III shown to have unique cohesive properties where a diverging angle of repose was obtained for all measurements. The simplified bluff bodies were therefore tested in an in-field environment where it was shown that different snow accumulation patterns are indeed obtained for natural snow compared to the machine made snow. This was already substantiated when comparing in-field tests of a car to wind tunnel results for the same car model, where the machine made snow were also seen to deposit on side surfaces, which does not occur for natural snow. This stresses how important the particle size is when manufacturing snow and the results can be used in future development of machine made snow.

This work has been addressing collisional properties and transport mechanisms of adhesive particles when the material is ice. However, much of the results are expected to be relevant for any adhesive material. For example, the conclusions that the angle of repose of snow depends on fall height and particle size, should be valid for any granular material consisting of adhesive particles. Also, a similar resuspension criterion as the one proposed in Paper IV can be derived for other types of contaminants when studying surface contamination, for example when studying dust particles or water droplets.

Nomenclature

Latin symbols

A_H – Hamaker coefficient (J)
A_p – particle cross-section area (m^2)
a – contact radius [m]
a_0 – equilibrium contact radius [m]
a_d – maximum contact radius [m]
A_H – hamaker coefficient [J]
Co – cohesion number
d – liquid layer thickness
d_A – projected area diameter [m]
D_c – critical particle diameter for resuspension [m]
D_v – volume-weighted mean projected area diameter [m]
D_p – particle diameter [m]
e_n – coefficient of restitution in normal direction
e_{qe} – quasi-static coefficient of restitution
e_t – coefficient of restitution in tangential direction
E^* – effective Young modulus [Pa]
E_i – impacting kinetic energy [J]
E_v – energy loss due to viscous damping [J]
E_s – energy to stick at collision [J]
F_n – normal contact force [N]
F_t – tangential contact force [N]
F_c – pull-off force [N]
F_v – viscous damping force [N]
f_t – sliding friction coefficient
f_r – rolling friction coefficient
g – gravitational acceleration [$\mathrm{m}^3/\mathrm{kg}\cdot\mathrm{s}^2$]
G – interaction energy [J/m^2]
G_0^+ – potential energy barrier [eV]
G^+ – activation energy [eV]
H – fall height [m]
J_i – time-averaged impact rate per area [$\mathrm{kg}/\mathrm{m}^2\cdot\mathrm{s}$]
J_a – time-averaged deposition rate per area [$\mathrm{kg}/\mathrm{m}^2\cdot\mathrm{s}$]
k_b – boltzmann constant [eV/K]
l – separation distance [m]
m^* – effective mass in contact [kg]
m_p – mass of particle [kg]

M – ratio of resolved to total turbulent kinetic energy
M_c – critical torque [Nm]
N_{D_i} – minimum number of correlated cells in direction D_i
P_m – bulk melting pressure [Pa]
q_m – latent heat of fusion [J/kg]
R – particle radius [m)]
R_0 – ideal gas constant [J/(K·mol)]
R^* – effective particle radius [m]
Re_H – height-based Reynolds number
Re_p – particle Reynolds number
St – Stokes number
T – temperature [K]
T_H – homologous temperature
T_m – bulk melting temperature [K]
V_r – rebound velocity [m/s]
V_c – critical impact velocity [m/s]
V_i – impact velocity [m/s]
V_s – stick velocity [m/s]
V_t – tangential velocity [m/s]
V_∞ – particle terminal velocity [m/s]
U_∞ – inlet velocity [m/s]
W – work of adhesion [J/m^2]

Greek symbols

α – angle of repose [°]
β – slant angle [°]
ε – particle roughness [m]
δ – normal overlap [m]
δa – uncertainty of quantity a
δ_c – critical normal overlap [m]
δ_r – rolling displacement [m]
$\delta_{r,c}$ – critical rolling displacement [m]
δ_t – tangential displacement [m]
ϵ – dielectric constant
$\Delta\gamma/\gamma$ – adhesion hysteresis for rolling
γ – surface energy [J/m^2]
ϕ – sphericity
$\hat{\phi}$ – circularity
κ – collisional efficiency
μ_q – chemical potential of quantity q [J/kg]
μ_f – dynamic viscosity [Pa·s]
ν_f – kinematic viscosity [m^2/s]
ν – Poisson's ratio
ρ_f – fluid density [kg/m^3]
ρ_p – particle density [kg/m^3]
ρ_l – liquid phase density [kg/m^3]
ρ_s – solid phase density [kg/m^3]
θ – contact angle [rad]
σ_x – standard deviation of sample series x
ξ – fraction of kinetic energy converted to damage

Acronyms

ABS – Acrylonitrile Butadiene Styrene
CFD – Computational Fluid Dynamics
DEM – Discrete Element Method
EWM – Exterior Water Management
LPM – Lagrangian Particle Model
CFL – Courant–Friedrichs–Lewy
IDDES – Improved Delayed Detached Eddy Simulation
JKR – Johnson-Kendall-Roberts
LES – Large Eddy Simulation
MM – Machine Made
PP – Precipitation Particles
QLL – Quasi-Liquid Layer
RANS – Reynolds Averaged Navier Stokes
RG – Round Grains
SGS – Subgrid-Scale
SH – Surface Hoar

Bibliography

[1] I. Isaksson-Hellman and M. Lindman, "Using insurance claims data to evaluate the collision-avoidance and crash-mitigating effects of Collision Warning and Brake Support Combined with Adaptive Cruise Control," *IEEE Intelligent Vehicles Symposium, Proceedings*, vol. 2016-Augus, no. Iv, pp. 1173–1178, 2016. doi.org/10.1109/IVS.2016.7535538

[2] R. Hussain and S. Zeadally, "Autonomous Cars: Research Results, Issues, and Future Challenges," *IEEE Communications Surveys and Tutorials*, vol. 21, no. 2, pp. 1275–1313, 2019. doi.org/10.1109/COMST.2018.2869360

[3] A. P. Gaylard, K. Kirwan, and D. A. Lockerby, "Surface contamination of cars: A review," *Proceedings of the Institution of Mechanical Engineers, Part D: Journal of Automobile Engineering*, vol. 231, no. 9, pp. 1160–1176, 2017. doi.org/10.1177/0954407017695141

[4] T. Hagemeier, M. Hartmann, and D. Thévenin, "Practice of vehicle soiling investigations: A review," *International Journal of Multiphase Flow*, vol. 37, no. 8, pp. 860–875, 2011. doi.org/10.1016/j.ijmultiphaseflow.2011.05.002

[5] F. Schilling, T. Kuthada, A. Gaylard, J. Wiedemann, and A. Wagner, "Advances in Experimental Vehicle Soiling Tests," *SAE Technical Papers*, vol. 2020-April, no. April, pp. 2596–2603, 2020. doi.org/10.4271/2020-01-0681

[6] A. Godfrey, P. Altmann, M. Johannesson, F. Ross, and T. Virdung, "Automated Design Optimization of Side View Mirror Geometries for Improved Autonomous Sensor and Vehicle Soiling Performance," *SAE Technical Papers*, no. 2021, pp. 1–10, 2021. doi.org/10.4271/2021-01-0951

[7] A. Kabanovs, A. Garmory, M. Passmore, and A. Gaylard, "Investigation into the dynamics of wheel spray released from a rotating tyre of a simplified vehicle model," *Journal of Wind Engineering and Industrial Aerodynamics*, vol. 184, no. September 2018, pp. 228–246, 2019. doi.org/10.1016/j.jweia.2018.11.024

[8] T. Bartels-Rausch, "Ten things we need to know about ice and snow," *Nature*, vol. 494, no. 7435, pp. 27–29, 2013. doi.org/10.1038/494027a

[9] U. department of Transporation, “FHWA Road Weather Management,” 2020. [Online]. Available: https://ops.fhwa.dot.gov/weather/weather_events/snow_ice.htm

[10] M. Jokela, M. Kutila, and P. Pyykönen, “Testing and validation of automotive point-cloud sensors in adverse weather conditions,” *Applied Sciences (Switzerland)*, vol. 9, no. 11, 2019. doi.org/10.3390/app9112341

[11] P. Abrahamsson, M. Eng, and A. Rasmuson, “An infield study of road snow properties related to snow-car adhesion and snow smoke,” *Cold Regions Science and Technology*, vol. 145, pp. 32–39, 2018. doi.org/10.1016/j.coldregions.2017.09.008

[12] Y. Li, J. Jin, T. Chen, L. Han, and Q. Cong, “Effect of an elastic surface on snow and ice accumulation on vehicles,” *Cold Regions Science and Technology*, vol. 180, no. 5988, p. 103154, 2020. doi.org/10.1016/j.coldregions.2020.103154

[13] B. R. Mcauliffe, “Potential for the Accumulation of Ice and Snow for a Boat-Tail Equipped Heavy-Duty Vehicle,” *SAE Technical Paper*, no. 2016-01-8141, 2016. doi.org/10.4271/2016-01-8141

[14] H. Hong, M. R. Bathusha, S. Patil, B. Mohammadian, V. Krishnan, M. Fountain, and H. Sojoudi, “Numerical Investigation of Snow Accumulation on a Sensor Surface of Autonomous Vehicle,” *SAE Technical Paper*, no. 2020-01-0953, 2020. doi.org/10.4271/2020-01-0953

[15] J. Wang, Y. Zhang, J. Zhang, X. Liang, S. Krajnović, and G. Gao, “A numerical investigation on the improvement of anti-snow performance of the bogies of a high-speed train,” *Proceedings of the Institution of Mechanical Engineers, Part F: Journal of Rail and Rapid Transit*, vol. 234, no. 10, pp. 1319–1334, 2020. doi.org/10.1177/0954409719893494

[16] C. Fierz, R. Armstrong, Y. Durand, P. Etchevers, E. Greene, D. McClung, K. Nishimura, P. Satyawali, and S. Sokratov, “The international classification for seasonal snow on the ground,” *IHP-VII Technical Documents in Hydrology*, vol. 83, no. 1, p. 90, 2009.

[17] S. C. Colbeck, “An overview of seasonal snow metamorphism,” *Reviews of Geophysics and Space Physics*, vol. 20, no. 1, pp. 45–61, 1982. doi.org/10.1029/RG020i001p00045

[18] J. C. Berg, *An introduction to interfaces and colloids: The bridge to nanoscience.* World Scientific Publishing Co., jan 2009. doi.org/10.1142/7579

[19] J. G. Dash, Haiying Fu, and J. S. Wettlaufer, “The premelting of ice and its environmental consequences,” *Reports on Progress in Physics*, vol. 58, no. 1, pp. 115–167, 1995. doi.org/10.1088/0034-4885/58/1/003

[20] J. G. Dash, A. W. Rempel, and J. S. Wettlaufer, “The physics of premelted ice and its geophysical consequences,” *Reviews of Modern Physics*, vol. 78, no. 3, pp. 695–741, 2006. doi.org/10.1103/RevModPhys.78.695

[21] T. Bartels-Rausch, H. W. Jacobi, T. F. Kahan, J. L. Thomas, E. S. Thomson, J. P. Abbatt, M. Ammann, J. R. Blackford, H. Bluhm, C. Boxe, F. Domine, M. M. Frey, I. Gladich, M. I. Guzmán, D. Heger, T. Huthwelker, P. Klán, W. F. Kuhs, M. H. Kuo, S. Maus, S. G. Moussa, V. F. McNeill, J. T. Newberg, J. B. Pettersson, M. Roeselová, and J. R. Sodeau, "A review of air-ice chemical and physical interactions (AICI): Liquids, quasi-liquids, and solids in snow," *Atmospheric Chemistry and Physics*, vol. 14, no. 3, pp. 1587–1633, 2014. doi.org/10.5194/acp-14-1587-2014

[22] N. Maeno, *Ice and Snow for Winter Sports.* Springer, 2016. doi.org/10.1007/978-1-4939-3020-3_1

[23] J. Luo and Y.-M. Chiang, "Wetting and Prewetting on Ceramic Surfaces," *Annual Review of Materials Research*, vol. 38, no. 1, pp. 227–249, 2008. doi.org/10.1146/annurev.matsci.38.060407.132431

[24] R. Rosenberg, "Why is ice slippery?" *Physics Today, American Institute of Physics*, pp. 50–55, 2005. doi.org/10.1063/1.2169444

[25] H. H. Jellinek, "Liquid-like (transition) layer on ice," *Journal of Colloid And Interface Science*, vol. 25, no. 2, pp. 192–205, 1967. doi.org/10.1016/0021-9797(67)90022-7

[26] J. G. Dash, B. L. Mason, and J. S. Wettlaufer, "Theory of charge and mass transfer in ice-ice collisions," *Journal of Geophysical Research*, vol. 106, no. D17, pp. 395–415, 2001. doi.org/10.1029/2001JD900109

[27] E. S. Thomson, "An Optical Study of Ice Grain Boundaries," Ph.D. dissertation, Yale University, 2010.

[28] J. N. Israelachvili, *Intermolecular and Surface Forces.* New York: Academic Press, 1992. doi.org/10.1016/C2009-0-21560-1

[29] D. Beaglehole and D. Nason, "Transition layer on the surface on ice," *Surface Science*, vol. 96, no. 1-3, pp. 357–363, 1980. doi.org/10.1016/0039-6028(80)90313-1

[30] J. Wåhlin and A. Klein-Paste, "Chemical melting of ice: Effect of solution freezing point on the melting rate," *Transportation Research Record*, vol. 2551, pp. 111–117, 2016. doi.org/10.3141/2551-13

[31] J. S. Wettlaufer, "Accretion in protoplanetary disks by collisional fusion," *Astrophysical Journal*, vol. 719, no. 1, pp. 540–549, 2010. doi.org/10.1088/0004-637X/719/1/540

[32] B. J. Murray, D. O'Sullivan, J. D. Atkinson, and M. E. Webb, "Ice nucleation by particles immersed in supercooled cloud droplets," *Chemical Society Reviews*, vol. 41, no. 19, pp. 6519–6554, 2012. doi.org/10.1039/c2cs35200a

[33] U. Nakaya, *Snow Crystals: Natural and Artificial.* Hardvard University Press, 1954. doi.org/10.4159/harvard.9780674182769

[34] J. R. Blackford, “Sintering and microstructure of ice: A review,” *Journal of Physics D: Applied Physics*, vol. 40, no. 21, 2007. doi.org/10.1088/0022-3727/40/21/R02

[35] L. K. Eppanapelli, J. Casselgren, J. Wåhlin, and M. Sjödahl, “Investigation of snow single scattering properties based on first order Legendre phase function,” *Optics and Lasers in Engineering*, vol. 91, no. July 2016, pp. 151–159, 2017. doi.org/10.1016/j.optlaseng.2016.11.013

[36] D. H. Male, *The seasonal snowcover.* Academic Press, Inc., 1980. doi.org/10.1016/b978-0-12-179450-7.50011-5

[37] A. Langlois, A. Royer, B. Montpetit, A. Roy, and M. Durocher, “Presenting Snow Grain Size and Shape Distributions in Northern Canada Using a New Photographic Device Allowing 2D and 3D Representation of Snow Grains,” *Frontiers in Earth Science*, vol. 7, no. January, 2020. doi.org/10.3389/feart.2019.00347

[38] R. M. German, “History of sintering: empirical phase,” *Powder Metallurgy*, vol. 56, no. 2, pp. 117–123, 2013. doi.org/10.1179/1743290112Y.0000000025

[39] S. C. Colbeck, “A review of sintering in seasonal snow,” *CRREL Report*, no. 97-10, p. 12, 1997.

[40] S. Li, J. Marshall, G. Liu, and Q. Yao, “Adhesive particulate flow: The discrete-element method and its application in energy and environmental engineering,” *Progress in Energy and Combustion Science*, vol. 37, pp. 633–668, 2011. doi.org/10.1016/j.pecs.2011.02.001

[41] M. Higa, M. Arakawa, and N. Maeno, “Measurements of restitution coefficients of ice at low temperatures,” *Planetary and Space Science*, vol. 44, no. 9, pp. 917–925, 1996. doi.org/10.1016/0032-0633(95)00133-6

[42] M. Higa, M. Arakawa, and N. Maeno, “Size Dependence of Restitution Coefficients of Ice in Relation to Collision Strength,” *Icarus*, vol. 133, no. 2, pp. 310–320, 1998. doi.org/10.1006/icar.1998.5938

[43] R. H. French, V. A. Parsegian, R. Podgornik, R. F. Rajter, A. Jagota, J. Luo, D. Asthagiri, M. K. Chaudhury, Y. M. Chiang, S. Granick, S. Kalinin, M. Kardar, R. Kjellander, D. C. Langreth, J. Lewis, S. Lustig, D. Wesolowski, J. S. Wettlaufer, W. Y. Ching, M. Finnis, F. Houlihan, O. A. Von Lilienfeld, C. J. Van Oss, and T. Zemb, “Long range interactions in nanoscale science,” *Reviews of Modern Physics*, vol. 82, no. 2, pp. 1887–1944, 2010. doi.org/10.1103/RevModPhys.82.1887

[44] V. Adrian Parsegian, *Van der Waals forces: A handbook for biologists, chemists, engineers, and physicists.* Cambridge University Press, jan 2005. doi.org/10.1017/CBO9780511614606

[45] K. L. Johnson, K. Kendall, and A. D. Roberts, “Surface Energy and the Contact of Elastic Solids,” *Proceedings of the Royal Society A: Mathematical, Physical and Engineering Sciences*, vol. 324, no. 1558, pp. 301–313, 1971. doi.org/10.1098/rspa.1971.0141

[46] F. M. Fowkes, "Attractive Forces At Interfaces," *Industrial & Engineering Chemistry*, vol. 56, no. 12, pp. 40–52, dec 1964. doi.org/10.1021/ie50660a008

[47] D. van Krevelen. and K. te Nijenhuis, *Properties of polymers : their correlation with chemical structure ; their numerical estimation and prediction from additive group contributions*, 4th ed. Elsevier, 2009.

[48] A. Chokshi, A. G. G. M. Tielens, and D. Hollenbach, "Dust Coagulation," *The Astrophysical Journal*, vol. 407, no. 2, pp. 806–819, 1993. doi.org/10.1086/172562

[49] R. Moreno-Atanasio, "Energy dissipation in agglomerates during normal impact," *Powder Technology*, vol. 223, pp. 12–18, 2012. doi.org/10.1016/j.powtec.2011.05.016

[50] C. Thornton, *Granular Dynamics, Contact Mechanics and Particle System Simulations: A DEM study.* Springer International Publishing, 2015, vol. 24. doi.org/10.1007/978-3-319-18711-2

[51] J. Marshall, "Discrete-element modeling of particulate aerosol flow," *Journal of Computational Physics*, vol. 228, no. 5, pp. 1541–1561, 2009. doi.org/10.1016/j.jcp.2008.10.035

[52] C. Dominik and A. G. Tielens, "Resistance to rolling in the adhesive contact of two elastic spheres," *Philosophical Magazine A*, vol. 72, no. 3, pp. 783–803, 1995. doi.org/10.1080/01418619508243800

[53] S. Krijt, C. Dominik, and G. M. Tielens, "Rolling friction of adhesive microspheres," *Journal of Physics D: Applied Physics J. Phys. D: Appl. Phys*, vol. 47, p. 9, 2014. doi.org/10.1088/0022-3727/47/17/175302

[54] C. Thornton and Z. Ning, "A theoretical model for the stick/bounce behaviour of adhesive, elastic- plastic spheres," *Powder Technology*, vol. 99, no. 2, pp. 154–162, 1998. doi.org/10.1016/S0032-5910(98)00099-0

[55] M. J. Matthewson, "Adhesion of spheres by thin liquid films," *Philosophical Magazine A: Physics of Condensed Matter, Structure, Defects and Mechanical Properties*, vol. 57, no. 2, pp. 207–216, 1988. doi.org/10.1080/01418618808204510

[56] D. Y. Chan and R. G. Horn, "The drainage of thin liquid films between solid surfaces," *The Journal of Chemical Physics*, vol. 83, no. 10, pp. 5311–5324, 1985. doi.org/10.1063/1.449693

[57] V. S. Sutkar, N. G. Deen, J. T. Padding, J. A. Kuipers, V. Salikov, B. Crüger, S. Antonyuk, and S. Heinrich, "A novel approach to determine wet restitution coefficients through a unified correlation and energy analysis," *AIChE Journal*, vol. 61, no. 3, pp. 769–779, 2015. doi.org/10.1002/aic.14693

[58] L. Davidson, *Fluid mechanics, turbulent flow and turbulence modeling*, 2021. [Online]. Available: http://www.tfd.chalmers.se/~lada/postscript_files/solids-and-fluids_turbulent-flow_turbulence-modelling.pdf

[59] M. L. Shur, P. R. Spalart, M. K. Strelets, and A. K. Travin, “A hybrid RANS-LES approach with delayed-DES and wall-modelled LES capabilities,” *International Journal of Heat and Fluid Flow*, vol. 29, no. 6, pp. 1638–1649, 2008. doi.org/10.1016/j.ijheatfluidflow.2008.07.001

[60] M. Faizan, S. Badshah, M. Badshah, and B. A. Haider, “Performance and wake analysis of horizontal axis tidal current turbine using Improved Delayed Detached Eddy Simulation,” *Renewable Energy*, vol. 184, pp. 740–752, 2022. doi.org/10.1016/j.renene.2021.11.107

[61] T. Hobeika and S. Sebben, “Tyre Pattern Features and Their Effects on Passenger Vehicle Drag,” *SAE International Journal of Passenger Cars - Mechanical Systems*, vol. 11, no. 5, pp. 401–413, 2018. doi.org/10.4271/2018-01-0710

[62] J. Törnell, S. Sebben, and D. Söderblom, “Influence of Inter-Vehicle Distance on the Aerodynamics of a Two-Truck Platoon,” *International Journal of Automotive Technology*, vol. 22, no. 3, pp. 747–760, jun 2021. doi.org/10.1007/S12239-021-0068-5

[63] E. Guilmineau, G. B. Deng, A. Leroyer, P. Queutey, M. Visonneau, and J. Wackers, “Assessment of hybrid RANS-LES formulations for flow simulation around the Ahmed body,” *Computers and Fluids*, vol. 176, pp. 302–319, 2018. doi.org/10.1016/j.compfluid.2017.01.005

[64] N. Ashton and A. Revell, “Key factors in the use of DDES for the flow around a simplified car,” *International Journal of Heat and Fluid Flow*, vol. 54, pp. 236–249, 2015. doi.org/10.1016/j.ijheatfluidflow.2015.06.002

[65] S. B. Pope, “Ten questions concerning the large-eddy simulation of turbulent flows,” *New Journal of Physics*, vol. 6, 2004. doi.org/10.1088/1367-2630/6/1/035

[66] L. Davidson, “Large Eddy Simulations: How to evaluate resolution,” *International Journal of Heat and Fluid Flow*, vol. 30, no. 5, pp. 1016–1025, 2009. doi.org/10.1016/j.ijheatfluidflow.2009.06.006

[67] Y. Tsuji, T. Tanaka, and T. Ishida, “Lagrangian numerical simulation of plug flow of cohesionless particles in a horizontal pipe,” *Powder Technology*, vol. 71, no. 3, pp. 239–250, 1992. doi.org/10.1016/0032-5910(92)88030-L

[68] C. Marchioli, “Large-eddy simulation of turbulent dispersed flows: a review of modelling approaches,” *Acta Mechanica*, vol. 228, no. 3, pp. 741–771, 2017. doi.org/10.1007/s00707-017-1803-x

[69] C. T. Corwe, J. D. Schwarzkopf, M. Sommerfeld, and T. Yutaka, *Multiphase Flows with Droplets and Particles*, 2nd ed. Taylor & Francis, 2012. doi.org/10.1201/b11103

[70] C. Henry and J. P. Minier, “Progress in particle resuspension from rough surfaces by turbulent flows,” *Progress in Energy and Combustion Science*, vol. 45, no. C, pp. 1–53, 2014. doi.org/10.1016/j.pecs.2014.06.001

[71] L. Schiller and A. Naumann, “Uber die grundlegenden Berechnungen bei der Schwerkraftaufbereitung,” *VDI Zeits*, vol. 77(12), pp. 318–320, 1933.

[72] A. Haider and O. Levenspiel, “Drag coefficient and terminal velocity of spherical and nonspherical particles,” *Powder Technology*, vol. 58, no. 1, pp. 63–70, may 1989. doi.org/10.1016/0032-5910(89)80008-7

[73] M. E. O’Neill, “A sphere in contact with a plane wall in a slow linear shear flow,” *Chemical Engineering Science*, vol. 23, no. 11, pp. 1293–1298, 1968. doi.org/10.1016/0009-2509(68)89039-6

[74] A. D. Maude, “The movement of a sphere in front of a plane at low Reynolds number,” *British Journal of Applied Physics*, vol. 14, no. 12, pp. 894–898, 1963. doi.org/10.1088/0508-3443/14/12/316

[75] M. Sommerfeld, “Theoretical and Experimental Modelling of Particulate Flows,” in *Technical Report Lecture Series 2000-06.* von Karman Institute for Fluid Dynamics, 2000.

[76] C. Dominik and A. G. G. M. Tielens, “The Physics of Dust Coagulation and the Structure of Dust Aggregates in Space,” *The Astrophysical Journal*, vol. 480, no. 2, pp. 647–673, 1997. doi.org/10.1086/303996

[77] M. L. Nietiadi, P. Umstätter, I. Alabd Alhafez, Y. Rosandi, E. M. Bringa, and H. M. Urbassek, “Collision-Induced Melting in Collisions of Water Ice Nanograins: Strong Deformations and Prevention of Bouncing,” *Geophysical Research Letters*, vol. 44, no. 21, pp. 10,822–10,828, 2017. doi.org/10.1002/2017GL075395

[78] K. Hashemnia, “Experimental study of the effect of temperature on the coefficient of restitution of steel balls impact to some industrial metal sheets at elevated temperatures,” *Powder Technology*, vol. 368, pp. 170–177, 2020. doi.org/10.1016/j.powtec.2020.04.053

[79] B. Yildirim, H. Yang, A. Gouldstone, and S. Müftü, “Rebound mechanics of micrometre-scale, spherical particles in high-velocity impacts,” *Proceedings of the Royal Society A: Mathematical, Physical and Engineering Sciences*, vol. 473, no. 2204, 2017. doi.org/10.1098/rspa.2016.0936

[80] R. B. Bird, W. E. Stewart, and E. N. Lightfoot, *Transport Phenomena.* John Wiley & Sons Inc, 2006.

[81] L. W. Gold, “Some observations on the dependence of strain on stress for ice,” *Canadian Journal of Physics*, vol. 36, no. 1, p. 1265, 1958.

[82] P. V. Hobbs, *Ice Physics.* Oxford University Press, 1974.

[83] M. Vargas, P. M. Struk, R. E. Kreeger, J. Palacios, K. A. Iyer, and R. E. Gold, “Ice particle impacts on a moving wedge,” 2013. doi.org/10.2514/6.2014-3045

[84] J. Schindelin, I. Arganda-Carreras, E. Frise, V. Kaynig, M. Longair, T. Pietzsch, S. Preibisch, C. Rueden, S. Saalfeld, B. Schmid, J. Y. Tinevez, D. J. White, V. Hartenstein, K. Eliceiri, P. Tomancak, and A. Cardona,

"Fiji: An open-source platform for biological-image analysis," *Nature Methods*, vol. 9, no. 7, pp. 676–682, 2012. doi.org/10.1038/nmeth.2019

[85] J. Y. Tinevez, N. Perry, J. Schindelin, G. M. Hoopes, G. D. Reynolds, E. Laplantine, S. Y. Bednarek, S. L. Shorte, and K. W. Eliceiri, "TrackMate: An open and extensible platform for single-particle tracking," *Methods*, vol. 115, pp. 80–90, 2017. doi.org/10.1016/j.ymeth.2016.09.016

[86] H. Bahaloo, T. Eidevåg, P. Gren, J. Casselgren, F. Forsberg, P. Abrahamsson, and M. Sjödahl, "Ice sintering: Dependence of sintering force on temperature, load, duration, and particle size," *Journal of Applied Physics*, vol. 131, no. 2, p. 025109, jan 2022. doi.org/10.1063/5.0073824

[87] D. Szabo and M. Schneebeli, "Subsecond sintering of ice," *Applied Physics Letters*, vol. 90, no. 15, pp. 2005–2008, 2007. doi.org/10.1063/1.2721391

[88] T. Hauk, I. Roisman, and C. Tropea, "Investigation of the Impact Behaviour of Ice Particles," in *6th AIAA Atmospheric and Space Environments Conference*, Atlanta, 2014. doi.org/10.2514/6.2014-3046

[89] G. E. Amidon, P. J. Meyer, and D. M. Mudie, "Particle, Powder, and Compact Characterization," *Developing Solid Oral Dosage Forms: Pharmaceutical Theory and Practice*, pp. 271–293, jan 2017. doi.org/10.1016/B978-0-12-802447-8.00010-8

[90] C. R. Woodcock and J. S. Mason, *Bulk Solids Handling.* Dordrecht: Springer Netherlands, 1988. doi.org/10.1007/978-94-009-2635-6

[91] D. Kuroiwa, Y. Mizuno, and M. Takeuchi, "Micromeritical Porperties of Snow," in *International Conference on Low Temperature Science. I. Conference on Physics of Snow and Ice, II. Conference on Cryobiology*, 1967, pp. 751–772. [Online]. Available: http://hdl.handle.net/2115/20340

[92] C. Willibald, H. Löwe, T. Theile, J. Dual, and M. Schneebeli, "Angle of repose experiments with snow: role of grain shape and cohesion," *Journal of Glaciology*, pp. 1–9, 2020. doi.org/10.1017/jog.2020.36

[93] T. Allen, *Particle Size Measurement*, 2nd ed. London: Chapman and Hall Ltd, 1975. doi.org/10.1007/978-94-009-0417-0

[94] M. A. Behjani, N. Rahmanian, N. Fardina bt Abdul Ghani, and A. Hassanpour, "An investigation on process of seeded granulation in a continuous drum granulator using DEM," *Advanced Powder Technology*, vol. 28, no. 10, pp. 2456–2464, 2017. doi.org/10.1016/j.apt.2017.02.011

[95] R. Turton and N. N. Clark, "An explicit relationship to predict spherical particle terminal velocity," *Powder Technology*, vol. 53, no. 2, pp. 127–129, 1987. doi.org/10.1016/0032-5910(87)85007-6

[96] J. Schweizer and J. B. Jamieson, "Snow cover properties for skier triggering of avalanches," *Cold Regions Science and Technology*, vol. 33, no. 2-3, pp. 207–221, 2001. doi.org/10.1016/S0165-232X(01)00039-8

[97] R. D. Cadle, *Particle size - Theory and industrial applications.* Reinhold Publishing Corporation, 1965.

[98] T. Hobeika and S. Sebben, “CFD investigation on wheel rotation modelling,” *Journal of Wind Engineering and Industrial Aerodynamics*, vol. 174, no. December 2017, pp. 241–251, 2018. doi.org/10.1016/j.jweia.2018.01.005

[99] R. Franzke, S. Sebben, and E. Willeson, “Experimental investigation of the air flow in a simplified underhood environment,” *Proceedings of the Institution of Mechanical Engineers, Part D: Journal of Automobile Engineering*, 2021. doi.org/10.1177/09544070211059786

[100] S. R. Ahmed, G. Ramm, and G. Faltin, “Some Salient Features of the Time -Averaged Ground,” *SAE Technical Paper*, no. 840300, 1984. doi.org/10.4271/840300

[101] W. Meile, G. Brenn, A. Reppenhagen, B. Lechner, and A. Fuchs, “Experiments and numerical simulations on the aerodynamics of the ahmed body,” *CFD Letters*, vol. 3, no. 1, pp. 32–38, 2011.

[102] H. Lienhart and S. Becker, “Flow and turbulence structure in the wake of a simplified car model,” *SAE Technical Paper*, no. 2003-01-0656, 2003. doi.org/https://doi.org/10.4271/2003-01-0656

[103] E. Serre, M. Minguez, R. Pasquetti, E. Guilmineau, G. B. Deng, M. Kornhaas, M. Schäfer, J. Fröhlich, C. Hinterberger, and W. Rodi, “On simulating the turbulent flow around the Ahmed body: A French-German collaborative evaluation of LES and DES,” *Computers and Fluids*, vol. 78, pp. 10–23, 2013. doi.org/10.1016/j.compfluid.2011.05.017

[104] M. Sommerfeld, “Modelling of particle-wall collisions in confined gas-particle flows,” *International Journal of Multiphase Flow*, vol. 18, no. 6, pp. 905–926, 1992. doi.org/10.1016/0301-9322(92)90067-Q

[105] A. D. Gosman and E. Ioannides, “Aspects of Computer Simulation of Liquid-Fuelled Combustors.” *AIAA Paper*, vol. 7, no. 6, pp. 482–490, 1981. doi.org/10.2514/6.1981-323

[106] B. Nasr, G. Ahmadi, A. R. Ferro, and S. Dhaniyala, “Overview of mechanistic particle resuspension models: comparison with compilation of experimental data,” *Journal of Adhesion Science and Technology*, vol. 33, no. 24, pp. 2631–2660, 2019. doi.org/10.1080/01694243.2019.1650989

[107] H. Reichardt, “Vollständige Darstellung der turbulenten Geschwindigkeitsverteilung in glatten Leitungen,” *Journal of Applied Mathematics and Mechanics / Zeitschrift für Angewandte Mathematik und Mechanik*, vol. 31, no. 7, pp. 208–219, 1951.

[108] M. Roth and R. Peikert, “Higher-order method for finding vortex core lines,” *Proceedings of the IEEE Visualization Conference*, pp. 143–150, 1998. doi.org/10.1109/visual.1998.745296

Appendices

Appendix A

Resuspension Test for the Self-Contamination of Cars

The results for the self-contamination tests in Chapter 3 showed that more snow accumulates in the rear of a vehicle when driven at lower speed compared to higher. To quantify the effect of aerodynamic load and resuspension of snow at different velocities a resuspension test was done where multiple tests were performed without cleaning the vehicle between the tests. The tests were labelled alphabetically from a to d. Test a was performed by driving the test vehicles (as introduced in Section 3) in 40 km/h for 12.5 km. Test b and c were performed by driving at 70 km/h for 12.5 km, where test c was a repetition of test b. Test d was performed by driving at alternating speeds of 70 km/h and 90 km/h (when possible on the test track). The results for the four tests on Vehicle A are shown in Fig. 3.4 and Fig. 3.5 for a rear view and a isometric rear view respectively. The results indicate that resuspension of snow is occurring where largest amount of snow accumulates for test a when driven at 40 km/h. When continuing driving at 70 km/h (test b and c), less snow is deposited on the vehicle even though the vehicle was not cleaned prior to these tests. Largest differences between test a and b can be seen below the rear side lamps in Fig. A.2.

As can be seen in the figures, the test was performed when sunlight was present. This caused some melting of snow on the vehicle, when the vehicle was photographed, however this was not considered to alter the findings from these tests.

Figure A.1: Snow accumulation during resuspension test at rear view of Vehicle A at T = $-12 \pm 3\,^{\circ}$C: (a) 40 km/h for 12.5 km; (b) 40 km/h for 12.5 km and 70 km/h for 12.5 km; (c) 40 km/h for 12.5 km and 70 km/h for 25 km; (d) 40 km/h for 12.5 km, 70 km/h for 25 km and 70/90 km/h for 12.5 km.

Figure A.2: Snow accumulation during resuspension test at isometric side rear view of Vehicle A at T = $-12 \pm 3\,^{\circ}$C: (a) 40 km/h for 12.5 km; (b) 40 km/h for 12.5 km and 70 km/h for 12.5 km; (c) 40 km/h for 12.5 km and 70 km/h for 25 km; (d) 40 km/h for 12.5 km, 70 km/h for 25 km and 70/90 km/h for 12.5 km.

Appendix B

Premelting due to Collisional Damage

In Wettlaufer [31] an equation for the predicted liquid layer thickness, d, caused by collisional melting was derived(see Eq. (3) in Wettlaufer [31]). This equation was used to predict d for particle-particle collisions and was simplified in Paper II for single ice particles colliding with a massive wall by inserting expressions for E_i, a_d and P. The mass of a spherical ice particle is calculated as

$$m_p = \rho_s \frac{4}{3} \pi R^3. \tag{B.1}$$

The E_i for a sphere colliding with a stationary wall is

$$E_i = \frac{1}{2} m_p V_i^2 = \rho_s \frac{2}{3} \pi R^3 V_i^2, \tag{B.2}$$

and according to the Hertz contact theory, the maximum contact radius, a_d, is [50]

$$a_d = \Big(\frac{15 m_p R^2 V_i^2}{16 E^*}\Big)^{1/5} = \Big(\frac{5 \pi \rho_s V_i^2}{4 E^*}\Big)^{1/5} R. \tag{B.3}$$

The contact pressure that causes the damage can be expressed in terms of the maximum contact pressure from Hertz by [31]

$$P = \xi P_d, \tag{B.4}$$

where P_d is the maximum contact pressure from the Hertz contact theory, which is [31]

$$P_d = \frac{3}{2\pi} \big(\frac{4}{3}\big)^{4/5} \Big(\frac{5 m_p V_i^2 E^{*4}}{4 R^3}\Big)^{1/5}, = \Big(\frac{40}{\pi^4} \rho_s V_i^2 E^{*4}\Big)^{1/5}. \tag{B.5}$$

The liquid layer thickness, d, caused by the damage when an ice particle collides with a massive wall can then be expressed as

$$d = \frac{\xi E_i}{\pi a_d^2} \frac{1}{\left(\frac{\rho_l q_m}{T_m}(T_m - T) + \frac{\rho_l - \rho_s}{\rho_s}(P_m - P)\right)}, \tag{B.6}$$

$$= \frac{\xi \rho_s \frac{2}{3}\pi R^3 V_i^2}{\pi \left(\frac{5\pi\rho_s V_i^2}{4E^*}\right)^{2/5} R^2 \left(\frac{\rho_l q_m}{T_m}(T_m - T) + \frac{\rho_l - \rho_s}{\rho_s}\left(P_m - \xi\left(\frac{40}{\pi^4}\rho_s V_i^2 E^{*4}\right)^{1/5}\right)\right)}, \tag{B.7}$$

$$= \left(\frac{16\sqrt{6}E^*}{135\pi}\right)^{2/5} \frac{\xi R \rho_s^{3/5} V_i^{6/5}}{\left(\frac{\rho_l q_m}{T_m}(T_m - T) + \frac{\rho_l - \rho_s}{\rho_s}\left(P_m - \xi\left(\frac{40}{\pi^4}\rho_s V_i^2 E^{*4}\right)^{1/5}\right)\right)}, \tag{B.8}$$

$$= \left(\frac{16\sqrt{6}E^*}{135\pi}\right)^{2/5} \frac{\xi D_p \rho_s^{3/5} V_i^{6/5}}{2\left(\frac{\rho_l q_m}{T_m}(T_m - T) + \frac{\rho_l - \rho_s}{\rho_s}\left(P_m - \xi\left(\frac{40}{\pi^4}\rho_s V_i^2 E^{*4}\right)^{1/5}\right)\right)}. \tag{B.9}$$

Appendix C

Wind Tunnel Results for the Ahmed body

C.1 Different Slant Angles at 115 km/h

Fig. C.1- C.3 show photographs from wind tunnel experiments on the Ahmed body for $\beta = 10°$, $\beta = 25°$, and $\beta = 35°$, where differences in accumulation patterns can be seen on the rear surface of the Ahmed body.

Figure C.1: Experimental trial on the Ahmed body at $U_\infty = 115$ km/h for $\beta = 10°$ showing front, side, and rear surfaces.

Figure C.2: Experimental trial on the Ahmed body at $U_\infty = 115$ km/h for $\beta = 25°$ showing front, side, and rear surfaces.

Figure C.3: Experimental trial on the Ahmed body at $U_\infty = 115$ km/h for $\beta = 35°$ showing front, side, and rear surfaces.

C.2 Varying Velocities for 35 Degree Slant Angle

Fig. C.4-C.9 show photographs from the wind tunnel experiments on the Ahmed body for the velocities 12 - 150 km/h. For the trials at 20 km/h and 150 km/h there were initial problems with the snow cannon causing droplets not nucleating, and therefore a small amount of icing occurred at the front surface.

The figures show that the distance between the front surface and the start of the snow deposition line on the side decreases with increasing U_∞. This distance was defined as ΔL_s and is illustrated in Fig. C.8. ΔL_s was measured through image analysis based on the taken photographs. The images were first calibrated using known distances in the figure and the uncertainty of the measurements was estimated by repeating the measurements multiple times and then taking 3σ as an error envelope for the estimated ΔL_s, where σ is the calculated standard deviation of each measurement series. Fig. C.10 shows mean values with the error envelope of ΔL_s as a function U_∞.

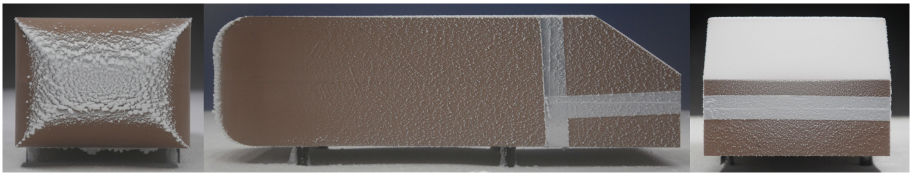

Figure C.4: Experimental trial on the Ahmed body at 12 km/h showing front, side, and rear surfaces.

Figure C.5: Experimental trial on the Ahmed body at 20 km/h showing front, side, and rear surfaces.

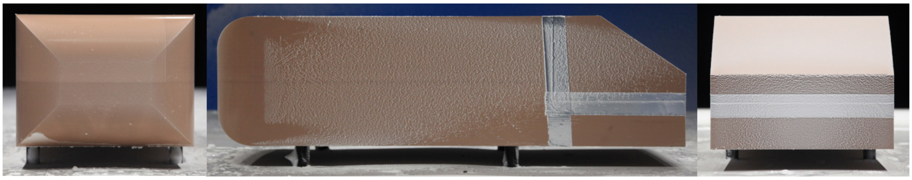

Figure C.6: Experimental trial on the Ahmed body at 30 km/h showing front, side, and rear surfaces.

Figure C.7: Experimental trial on the Ahmed body at 70 km/h showing front, side, and rear surfaces.

Figure C.8: Experimental trial on the Ahmed body at 115 km/h showing front, side, and rear surfaces.

Figure C.9: Experimental trial on the Ahmed body at 150 km/h showing front, side, and rear surfaces.

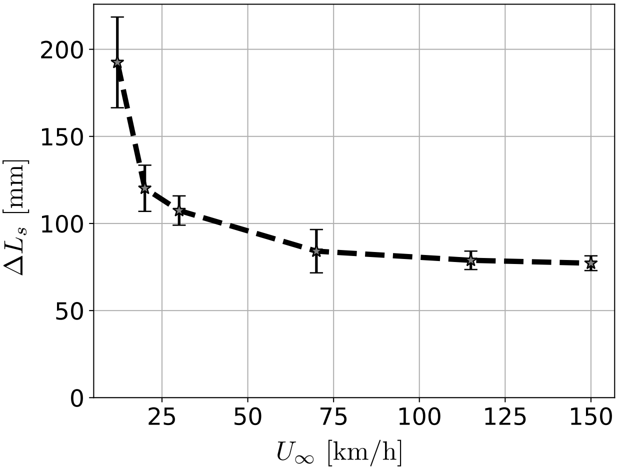

Figure C.10: The distance between the front face and the start of the snow accumulation line, ΔL_s on the Ahmed body as a function of U_∞. Error bars representing the uncertainty estimation from the image analysis.

Appendix D

Critical Adhesion Velocity in Tangential Direction

For tangential interaction previous research has shown that adhesive particles are more likely to roll than slide and therefore we assume that the tangential energy dissipation is dominated by adhesive rolling [51]. The energy for onset of rolling was shown by Dominik and Tielens [76] to be

$$E_t = 3\pi W \delta_{r,c}^2. \tag{D.1}$$

Using the expression for $\delta_{r,c}$ derived by Krijt et al. [53] (Eq. (2.36)), E_t can be written as

$$E_t = \frac{\pi W a_0^2}{48}\Big(\frac{\Delta\gamma}{\gamma}\Big)^2. \tag{D.2}$$

Dividing Eq. (D.2) with Eq. (4.2) it follows that

$$\frac{E_t}{E_s} \approx 0.054\Big(\frac{\Delta\gamma}{\gamma}\Big)^2, \tag{D.3}$$

now relating the critical velocity in tangential direction $V_{c,t}$ to E_t as

$$\frac{1}{2} m_p V_{c,t}^2 = E_t, \tag{D.4}$$

it follows that

$$V_{c,t} \approx 0.23\Big(\frac{\Delta\gamma}{\gamma}\Big)V_s. \tag{D.5}$$

It is therefore sufficient, in the implementation of an adhesion model that predicts particle stick or bounce, to calculate V_s for a particle, and using that to calculate $V_{c,t}$ with Eq. (D.5).

Papers

PAPER I

Modeling of dry snow adhesion during normal impact with surfaces

PAPER II

Collisional damping of spherical ice particles

Powder Technology 383 (2021) 318–327

Contents lists available at ScienceDirect

Powder Technology

journal homepage: www.elsevier.com/locate/powtec

Collisional damping of spherical ice particles

Tobias Eidevåg [a,b,*], Erik S. Thomson [c], Sofia Sollén [d], Johan Casselgren [d], Anders Rasmuson [a]

[a] Department of Chemistry and Chemical Engineering, Chalmers University of Technology, SE-41296 Gothenburg, Sweden
[b] Contamination and Core CFD, Volvo Car Corporation, SE-40531 Gothenburg, Sweden
[c] Department of Chemistry & Molecular Biology, Atmospheric Science, University of Gothenburg, SE-41296 Gothenburg, Sweden
[d] Division of Fluid and Experimental Mechanics, Luleå University of Technology, SE-97187 Luleå, Sweden

ARTICLE INFO

Article history:
Received 5 November 2020
Received in revised form 10 December 2020
Accepted 16 January 2021
Available online 22 January 2021

Keywords:
Ice adhesion
Particle impact
coefficient of restitution
Icing premelting
Surface melting

ABSTRACT

This paper presents experimental values for the coefficient of restitution (e_n) for millimeter-sized ice particles colliding with massive walls at different temperatures. Three different wall materials are tested: hardened glass, ice and Acrylonitrile butadiene styrene (ABS) polymer. The results show a high sensitivity to impact velocity V_i, where e_n decreases rapidly with increasing V_i. The results also show a decrease in e_n with increasing temperature T. A novel model that predicts e_n based on the assumption of collisional melting and viscous damping caused by an increased premelted liquid-layer, is proposed. The model predicts both the velocity and the temperature trends seen in the experiments. The difference obtained in experiments between wall materials is also captured by the new model. A generalized regime map for ice particle collisions is proposed to combine the new model with previous work.

1. Introduction

Collisions of ice particles are important in many physical systems. A deep understanding of these collisions is important to model and predict how systems of ice particles will develop in time. Examples of such systems are ice particles in space that agglomerate, which is an important part of planet formation [1]; and ice particles in the atmosphere that transfer charge through collisions, thereby triggering thunderstorms [2] or grow and precipitate from the sky as snow and/or rain [3]. Snow and ice tend to accumulate on surfaces, such as buildings [4], infrastructure [5], and vehicles [6]. Significant research focuses on preventing snow sticking and accumulating. A fundamental understanding of the energy dissipation in collisions between ice particles and massive walls, is thus an important part of understanding how snow or ice accumulates on surfaces.

The energy dissipation for a particle colliding with a wall is an important subject in the field of particle technology [7–10]. A well-established measure to characterize the energy dissipation for particle collisions is the coefficient of restitution e_n, which is the ratio between normal rebound velocity V_r and normal impact velocity V_i,

$$e_n = \frac{V_r}{V_i}, \tag{2}$$

where by definition it is expected that $e_n \in [0,1]$. A variety of different damping mechanisms affect the dependencies and trends of e_n, and consequently, there are many different models for e_n [11]. Examples of mechanisms that have commonly been studied are viscoelastic damping [12,13], adhesion (typically due to van der Waals forces) [14,15], plastic dissipation [16], and liquid layer damping [17–21]. The e_n has also been extensively studied for ice particles and a wide range of studies examine ice particle impacts [22–25], and Güttler et al. [26] have compiled an excellent literature survey. They summarize experimental data of particles in general and for ice particles in particular. One of the most extensive works that examines the e_n specifically for ice particles is by Higa et al. [27]. Those authors studied spherical ice particles with diameters from 2.8 to 72 mm for a variety of temperatures and impact velocities. A key finding from that study is that below a certain critical velocity, e_n is constant and independent of V_i, while above this velocity, e_n rapidly decreases with increasing V_i.

Although many studies have examined ice particle collisions, to the best of our knowledge, no data has been published on the e_n for ice particles smaller than 2.8 mm. Snow grains on the ground typically, transform from snowflakes into spherical-shaped particles through metamorphism [28], and this grains range from hundreds of microns to a few millimeters in diameter [29].

---

* Corresponding author at: Department of Chemistry and Chemical Engineering, Chalmers University of Technology, SE-41296 Gothenburg, Sweden.
E-mail address: tobias.eidevag@chalmers.se (T. Eidevåg).

https://doi.org/10.1016/j.powtec.2021.01.025
0032-5910/

In this paper, we present experimental results that extend the knowledge of ice particle collisions by examining collisions of millimeter-sized ice particles with an ice wall, a hardened glass wall and an ABS polymer wall. These walls are interesting because they represent large variations in Young's modulus, and they are common surfaces on vehicles in the automotive industry. Icing of external automobile surfaces is becoming a key obstacle for automated cold-weather driving. We relate observations to previous experimental work by Higa et al. [27], and utilize a collisional melting model based on a framework proposed by Wettlaufer [30] to model collisional melting for collisions between ice particles. We arrive at a novel model for e_n that predicts a viscous loss caused by a premelted liquid layer, and we show that the model captures experimental observations. Finally, we present a regime map of the e_n for ice particles where we combine our previous work on damping due to van der Waals forces [31] with the expanded collisional model.

2. Measurements

Experiments were performed to measure the e_n for ice particles colliding with massive walls of different materials. To validate the setup, collisions of glass particles against a glass wall were also measured at the same temperatures used in the ice particle experiments and at room temperature.

2.1. Experimental setup

Ice particles were created using a previously established method whereby a mixture of distilled water and food colorant is dropped into liquid nitrogen using a syringe [32]. The syringe allowed the size of the droplets to be uniform, and the smallest available syringe needle was used to create the smallest ice particles possible. Previous studies of millimeter-sized spherical glass particles colliding with glass walls [19,33], led us to use spherical glass particles to validate the experimental setup. Glass particles with 0.5 mm, 1 mm, and 2 mm in diameter were used. Particles were picked up using a paintbrush and released into a vertical metal pipe. The particles were then accelerated to a certain impact speed V_i by gravity and collided with the massive wall placed under the pipe. The impact speed was varied by changing the length of the pipe. Ice, hardened glass, and ABS polymer were used as the massive wall materials where the ice wall was created by freezing distilled water in a silicone mold. A high-speed camera recorded each particle before and after impact and a laser connected to the camera triggered image acquisition when a particle crossed the laser beam prior to impact (Fig. 1). The experiments were recorded at 4000 frames per second. In order to focus this work on normal collisions between particles and walls, massive walls with low surface roughness were chosen to avoid tangential velocity components after impact and experimental samples with a clear tangential velocity component were removed from the data set. The experiments were conducted in a large cooling chamber with temperature control. A temperature probe used to monitor the temperature was located 20 cm from the massive wall and was used to monitor the temperature T with the mean and 1σ standard deviation to indicate uncertainty (Table 1). Recordings from the high-speed camera were analyzed to extract particle trajectories, velocities, and particle size. The image analysis was done using Fiji and the single-particle tracking tool TrackMate [34]. Before using TrackMate, images were pre-processed to improve particle detection by removing the background and masking the images. For each recorded frame, the particle diameter was calculated from the sum of the pixel area. The median of all calculated diameters were then taken to estimate the particle sizes, where median were used to eliminate outliers caused by edge effects. The trajectories resulting from the image analysis were post-processed to determine the velocity before and after each collision. The uncertainty in position was quantified by manually measuring the center positions of particles and averaging the deviation between these measurements and the output of the tracking tool. The obtained average positional uncertainty $\delta x = 2.613 \cdot 10^{-5}$ m results in an velocity uncertainty $\delta V = 0.105$ m/s. The uncertainty in the coefficient of restitution, δe_n, is then calculated by further propagation of uncertainties as

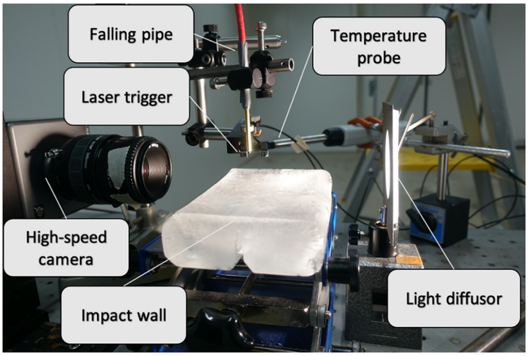

Fig. 1. Experimental setup.

$$\delta e_n = \sqrt{\left(\frac{\delta V_i}{V_i}\right)^2 + \left(\frac{\delta V_r}{V_r}\right)^2}\, e_n. \tag{2}$$

Fig. 2 illustrates an ice particle colliding with a glass wall with the particle's center point trajectory extracted from the image analysis overlayed as circles.

For particle impacts that occur close to the bulk material melting temperature there is the potential that proximity to the melting temperature T_m plays an important role in the collisions. Thus the homologous temperature $T_H = T/T_m$, where T is the experimental temperature, is often used to depict how close to the melting point the experiments come.

2.2. Experimental observations

The e_n obtained for glass particles colliding with glass walls is shown in Fig. 3 as a function of V_i. A melting temperature of $T_m = 1300$K is used for glass particles to calculate T_H and these measurements detected no difference for the e_n at different temperatures, or for varying V_i. The mean e_n was found to be 0.94 ± 0.05 at the 2σ level.

An empirical function for e_n proposed by Higa et al. [27] for ice particles impacting an ice wall is,

$$e_n = \begin{cases} e_{qe}\left(\dfrac{V_i}{V_c}\right)^{-\ln(V_i/V_c)} & V_i \geq V_c, \\ e_{qe} & V_i < V_c, \end{cases} \tag{3}$$

Table 1
Experimental parameters, wall material, T and T_H; and the resulting e_{qe} and V_c extracted from fitting experimental data.

Impact wall	T [K]	T_H [−]	e_{qe}	V_c [m/s]
glass	254 ± 1	0.930	0.74 ± 0.02	1.60 ± 0.07
	262 ± 1	0.959	0.67 ± 0.03	1.38 ± 0.07
ice	254 ± 1	0.930	0.82 ± 0.02	1.90 ± 0.10
	262 ± 1	0.959	0.79 ± 0.04	1.62 ± 0.16
	267 ± 1	0.977	0.66 ± 0.05	1.39 ± 0.13
abs polymer	254 ± 1	0.930	0.86 ± 0.05	>2.8
	262 ± 1	0.959	0.89 ± 0.02	>3.1

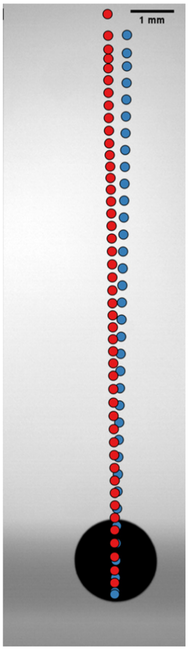

Fig. 2. Snapshot of an ice particle colliding with a glass wall with extracted trajectories from the image analysis. Blue circles show the approaching path, with red circles illustrating the path of the rebounding particle.

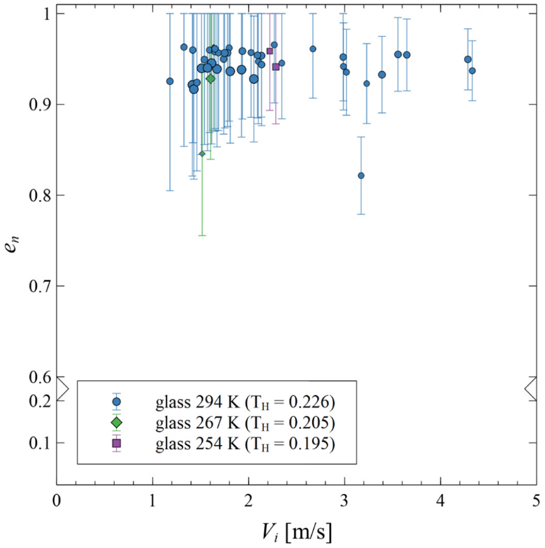

Fig. 3. The e_n of glass particles colliding with a glass wall as a function of impact velocity at three different temperatures. The error bars represent the propagated uncertainty δe_n.

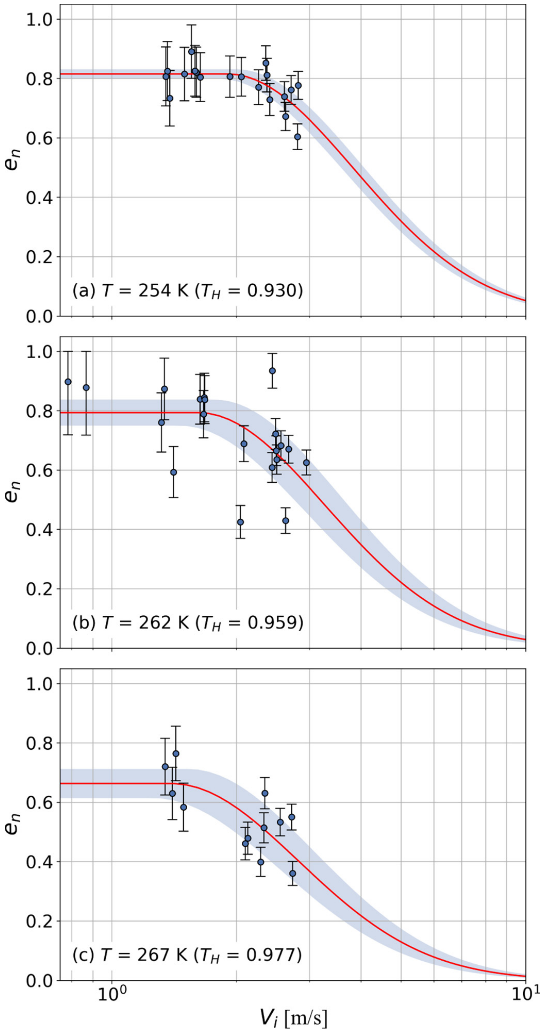

Fig. 4. The e_n for ice particles colliding with an ice wall as a function of V_i. The error bars represent δe_n. The line shows the non-linear least square fit of e_n as a function of V_i. The shaded area shows the propagated uncertainty of e_n based on the matrix square root of the covariance matrix from the non-linear fit of V_c and e_{qe}.

where e_{qe} is the coefficient of restitution in the quasi-elastic regime, and V_c is the critical velocity and suggests e_n varies only above V_c. Measurements of ice particles colliding with an ice wall were conducted at three temperatures: 267 K, 262 K, and 254 K, which correspond to T_H of 0.977, 0.959 and 0.930 respectively. The ice particles had an average diameter of 1.64 ± 0.15 mm. Fig. 4 shows the measured e_n values with a non-linear least square fit of Eq. (3) superimposed. The uncertainties of the fitted V_c and e_{qe} are quantified as the matrix square roots of the covariance matrix from the non-linear fit.

Collisions of ice particles with a glass wall were measured at two temperatures: 254 K and 262 K. The resulting measurements of e_n are shown in Fig. 5.

Similar to the experiments with a glass wall, measurements of ice particles colliding with an ABS polymer wall were conducted at two temperatures: 254 K and 262 K. The extracted e_n are shown in Fig. 6, where it appears that for all observations that $V_i < V_c$.

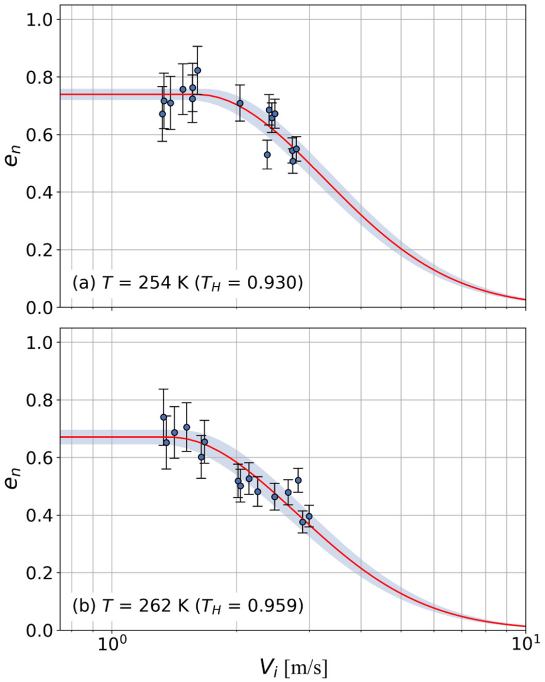

Fig. 5. The e_n for ice particles colliding with a glass wall as a function of V_i. The error bars represent δe_n. The line shows the non-linear least square fit of e_n as a function of V_i. The shaded area shows the propagated uncertainty of e_n based on the matrix square root of the covariance matrix from the non-linear fit of V_c and e_{qe}.

A summary of the fitted parameters e_{qe} and V_c are shown in Table 1 in addition to the uncertainties estimated from the coviarance matrix.

The confidence interval for both e_{qe} and V_c in our experimental observations for ice particles colliding with an ice wall at $T = 262$ K are either very close to or overlap with the confidence intervals for the two parameters at $T = 254$ K and $T = 267$ K. A comparison of results for the experiments involving massive walls of ice and glass shows that the e_n is lower for the glass wall than the ice wall. This is also reflected in the obtained parameters V_c and e_{qe}. For all experiments except those with the ABS polymer, a clear trend was obtained where e_n decreased with increasing T_H. This is maybe not surprising given the fact that T_H is greater than 0.9, which are temperatures that are very close to the melting point of water.

2.3. Comparison with previous experimental results

The values of e_n obtained for glass particles colliding with a glass wall shown in Fig. 3 are similar to previous findings [19,33] that found e_n to range from 0.92 to 0.98. Since the experimental conditions were far from the melting temperature of the glass particles, with $T_H \approx 0.2$, we did not expect to see a difference between temperatures, and the values obtained imply that the experimental equipment was not affected operating in cold temperatures. Ice particles colliding with both glass and ice surfaces behave differently, which is also expected given that $T_H > 0.9$ in our observations.

Fig. 4 shows that Eq. (3) captures the rapid trend of a decrease in e_n with increasing V_i above the critical velocity V_c. An empirical equation for the critical velocity V_c was derived in Higa et al. [27] as a function of temperature and particle radius R. If we simplify this equation it can be re-expressed as,

$$V_c = K_1 \exp\left(\frac{K_2}{k_b T}\right) R^{-0.5}, \tag{4}$$

where k_b is the Boltzmann constant, and K_1 and K_2 are constants extracted from the Higa et al. [27] results ($K_1 = 7.0055 \cdot 10^{-7}$ and $K_2 = 0.25$).

Fig. 7 shows the V_c predicted by Eq. (4) for the three temperatures used in the ice particle collision experiments with an ice wall. The figure also shows the values obtained for V_c from Table 1 and the values from Higa et al. [27] obtained at $T = 261$ K.

3. Collisional damping of ice particles

3.1. Collisional melting - Premelting due to an impact

The present work and the previous Higa et al. [27] experiments show that the e_n, for ice particles colliding with massive walls, significantly decreases with increasing V_i above certain velocities. For obtained values of $V_c \approx 1$ m/s, the velocity dependency of e_n is close to V_i^{-1}, which is significantly more rapid than plastic dissipation models predict for e_n, which are typically proportional to $V_i^{-1/4}$ [35]. Interestingly, this strong dependency has been seen before. A study of micrometer-sized metal particles colliding with a metal surface [36] found that the metal particles follow the plastic dissipation dependency of $V_i^{-1/4}$ for low velocities ($V_i \leq 10$ m/s). At high velocities (100–1000 m/s), however, e_n begins to follow V_i^{-1}, the same dependency found in this work for ice particles. However, those experiments were performed at room temperature meaning at low T_H for the metal. Given that the T_H in these ice particle experiments is close to unity it is not surprising that e_n for ice particles begins to fall at lower velocities since the material will be more sensitive to melting. Sensitivity to T_H has been observed for other materials, for example, in a recent study where steel balls collide with heated metal walls, Hashemnia [37] shows that e_n begins to decrease rapidly for $T_H > 0.6$. Another study of glass particles colliding with a PEG (Poly Ethylene Glycol) substrate reported that e_n fell to zero as the substrate approached its melting temperature [38].

As shown in Fig. 7 the empirical equation for V_c (Eq. (4)) predicts that V_c decreases with increasing T_H. However, physical reasoning suggest that V_c should approach 0 m/s as $T_H \rightarrow 1$, which implies that something fundamental is missing in Eq. (4). We propose that the damping observed for ice particles can be explained by collisional melting and specifically an increase in premelting of a liquid layer on the ice surface due to the collision. The existence of equilibrium liquid-like layers on ice surfaces is well documented [39–44], and here we expect the collision to enhance the existence of that layer. Such films are often referred to as premelted layers, quasi-liquid layers (QLL) or distorted liquid-like materials, and the material properties of the liquid layers are not necessarily expected to be those of the bulk liquid.

Models have been proposed for ice particle collisions that predict an increased premelting due to a collision [2]. Wettlaufer [30] proposed a theoretical model for collisional fusion as an explanation for the rapid damping of ice particles observed by Higa et al. [27]. That model assumes that a fraction ξ of the kinetic energy will damage the interface, and the resulting disorder causes an enhanced premelted liquid layer. This liquid layer can subsequently freeze during impact, causing the particle to fuse with the colliding object at certain velocities. The model is intended to predict fusion between ice grains at astrophysically relevant temperatures and pressures.

While fusion is relevant for astrophysical conditions with short freezing times, for our operating conditions with temperatures

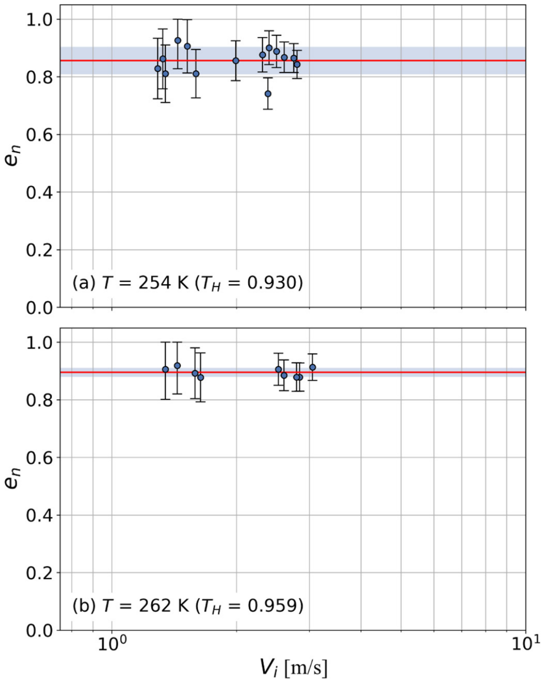

Fig. 6. The e_n for ice particles colliding with an ABS polymer wall as a function of V_i. The error bars represent δe_n. The line shows the non-linear least square fit of e_n as a function of V_i. The shaded area shows the propagated uncertainty of e_n based on the matrix square root of the covariance matrix from the non-linear fit of V_c and e_{qe}.

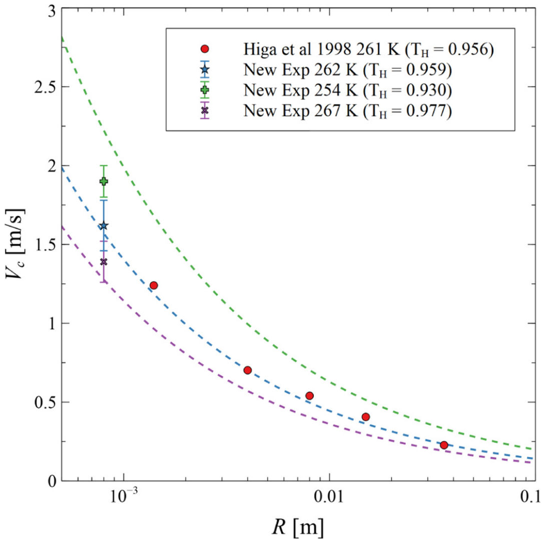

Fig. 7. Critical velocity V_c for ice particles colliding with a massive ice wall, results in this work together with previous experiments by Higa et al. [27], and the predicted V_c as a function of size for 262, 254, and 267 K. Dashed lines from Eq. (4) where the constants K_1 and K_2 are extracted from Higa et al. [27].

significantly closer to the melting point of water, fusion cannot explain the observed temperature trend. Specifically, with increasing T_H, the time scale for freezing by heat conduction is decreasing and at the same time the predicted d is increasing. This means that with increasing T_H the rate of freezing is reduced while the amount of liquid to freeze is increasing. The experimental measurements show that the damping consistently increases with increasing temperature for both the ice walls and the glass walls. We therefore argue that the associated energy loss instead can be explained by the presence of an increased liquid-layer and the associated energy loss this layer causes.

An equation for the liquid layer thickness d caused by ice particles colliding with other ice particles was derived by Wettlaufer [30]. By simplifying Eq. (3) in Wettlaufer [30] for ice particles colliding with walls we obtain,

$$d = \left(\frac{16\sqrt{6}E^*}{135\pi}\right)^{2/5} \frac{\xi\rho_s^{3/5}V_i^{6/5}R}{\left(\frac{q}{T_m}(T_m - T) + \frac{(\rho_l - \rho_s)}{\rho_s}\left(P_m(T) - \xi\left(\frac{40\rho_s V_i^2 E^{*4}}{\pi^4}\right)^{1/5}\right)\right)}. \quad (5)$$

Here ρ_s and ρ_f are the density of solid and liquid water. T_m and P_m are the bulk melting temperature and pressure for water. E^* is the effective Young's modulus in the collision defined as,

$$\frac{1}{E^*} = \frac{1-\nu_1^2}{E_1} + \frac{1-\nu_2^2}{E_2}, \quad (6)$$

where E_i and ν_i are the Young's modulus and Poisson's ratio for material i. The damage term ξ is used to describe how microscopic and mesoscopic changes lead to the deterioration of macroscopic material properties [45]. With this new formulation for d we make two interesting observations: 1) d is predicted to be linearly proportional to R, which means that the ratio, d/R, is independent of particle size. 2) d is proportional to $E^{*2/5}$, which means that increased melting should be observed with increasing Young's modulus of the material walls. To illustrate how the liquid layer changes with V_i, Fig. 8 shows the predicted d for ice particles upon impact with an ice wall as a function of V_i for the temperatures 267 K, 262 K, and 254 K. The critical velocities found in this work are highlighted in the figure. The figure shows a rapid increase in d for velocities above V_c and d is predicted to be a few microns. The secondary y-axis in the figure shows d/R, and we can see that the liquid layer thickness ranged from 0.2% to 0.4% of particle radius R around V_c. In these predictions $\xi = 0.15$ is used based on the work by Wettlaufer [30]. The uncertainty of ξ will be discussed later in this section. The energy loss for a particle-wall collision with the presence of a liquid layer has been the subject of many studies. In Crüger et al. [33], the authors observed that the e_n decreases for glass particles colliding with a wetted glass wall with increased liquid layer thickness. Matthewson [46] studied the adhesion of spheres due to a thin

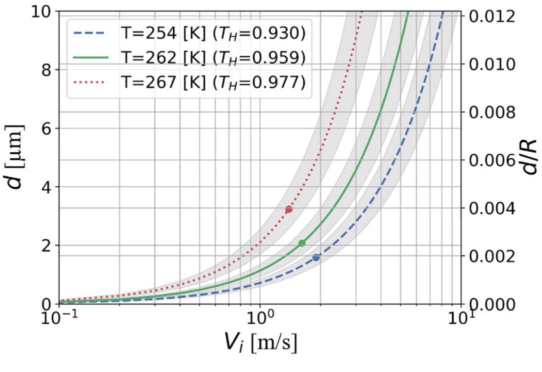

Fig. 8. Predicted d for ice particles colliding with an ice wall. The points show the critical velocities V_c obtained from the experiments in this work. The lines show d and d/R for $\xi = 0.15$, with the shaded areas showing how d and d/R vary for $\xi = 0.15 \pm 0.025$.

liquid film, and show that the adhesive force can be divided into two components: a meniscus force and a viscous damping force. While the resulting energy loss for the meniscus force is expected to be constant for a specific particle size and independent of V_i, the viscous damping loss depends on d, V_i, and the viscosity η of the fluid. We, therefore, argue that the viscous damping force will dominate for the case of damping caused by an increased premelted liquid layer. Based on Reynolds lubrication theory it has been shown by Chan and Horn [47] and Matthewson [46] that the viscous force F_v can be expressed as a function of the particles approaching velocity V and the separation distance x between the particle and the wall as,

$$F_v = 6\pi\eta R^2 h(x) V, \tag{7}$$

where $h(x)$ is a function that depends on the wetting conditions in the collision. For a particle colliding with an infinite wetted wall with constant d, Chan and Horn [47] showed that,

$$h(x) = \frac{1}{x}, \tag{8}$$

which is valid except for very thin films or when x tends to zero (when the two solid surfaces come closer to contact). The resulting energy loss E_v, for a particle colliding with an infinite wetted wall was estimated by Sutkar et al. [20] to be

$$E_v = \oint F_v dx = \frac{3}{2}\pi\eta R^2 V_i \ln\left(\frac{d}{\varepsilon}\right), \tag{9}$$

where the path integral is defined as the collision trajectory and ε is the particle roughness. In our situation the wetting area is finite and the thickness d is increasing during the course of collision (due to melting). This means that we expect $h(x)$ to be more complex than for an infinite wetted wall with constant d. It is however reasonable to expect that the resulting E_v would take a similar form as Eq. (9) and therefore we propose

$$E_v \propto \eta(T) R^2 V_i (d/\varepsilon)^a, \tag{10}$$

where the constant a can be empirically determined. The total energy loss E_t is then

$$E_t = E_v + \xi E_i, \tag{11}$$

where E_i is the initial kinetic energy and thus ξE_i is the amount of energy that causes damage to the ice particle surface. The E_t can also be expressed as a function of e_n as

$$E_t = E_i(1 - e_n^2). \tag{12}$$

We determine a using nonlinear curve fitting of the observed energy loss represented by Eq. (3). For our experimental values we find an average best fit of $a = 1.46$ for ice particles colliding with an ice wall, and therefore propose that $a = 1.5$ (or $a = 3/2$).

The premelted liquid layer is a distorted region with properties between solid and bulk liquid water [41], therefore, η is unknown but likely temperature dependent. The temperature dependent viscosity of a liquid can be expressed as,

$$\eta \propto \exp\left(\frac{G_0^+}{k_b T}\right), \tag{13}$$

where G_0^+ is a potential energy barrier empirically determined by fitting experimental data [48]. Using this we can express the viscous energy loss E_v for an ice particle colliding with a massive wall as,

$$E_v = C\exp\left(\frac{G_0^+}{k_b T}\right) V_i R^2 (d/\varepsilon)^{1.5}, \tag{14}$$

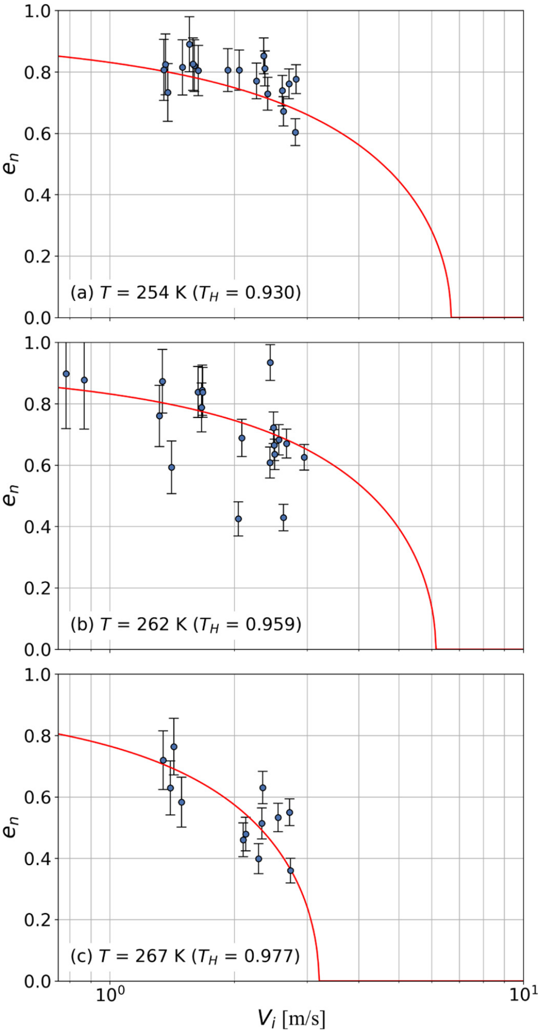

Fig. 9. Predicted e_n according to liquid layer damping together with experimental results for ice particles colliding with an ice wall as a function of V_i. The error bars represent the propagation of uncertainty for measured e_n.

where C and G_0^+ are coefficients with units Pa·s and eV, respectively. Here C represents the combined value of all constants in Eq. (10). The resulting coefficient of restitution can then be expressed as,

$$e_n = \sqrt{\frac{E_i - E_v - \xi E_i}{E_i}}. \tag{15}$$

Fitting the coefficients C and G_0^+ to the experimental data from ice particles colliding with an ice wall at $T = 267$ K and $T = 254$ K we obtained average values for $C = 0.5 \cdot 10^{-10}$ Pa·s and $G_0^+ = 0.5$ eV. The best fit gives remarkably similar results for the experiments at $T = 267$ K and $T = 254$ K with only a difference of 0.6% and 0.5% for

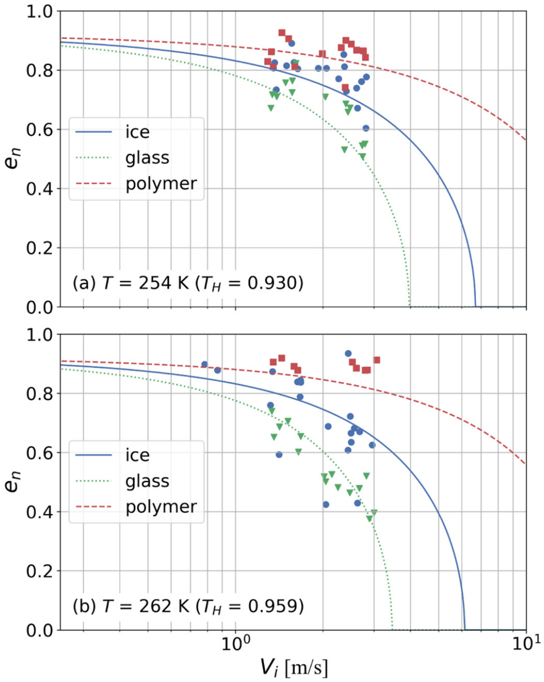

Fig. 10. The e_n for ice particles colliding with different massive walls as a function of V_i. Solid, dashed and dotted lines show predicted e_n caused by collisional melting for ice particles colliding with an ice wall, a polymer wall and a glass wall respectively. Marker symbols (Circle, square and triangle) show experimental measurements for ice particles colliding with an ice wall, a polymer wall and a glass wall respectively.

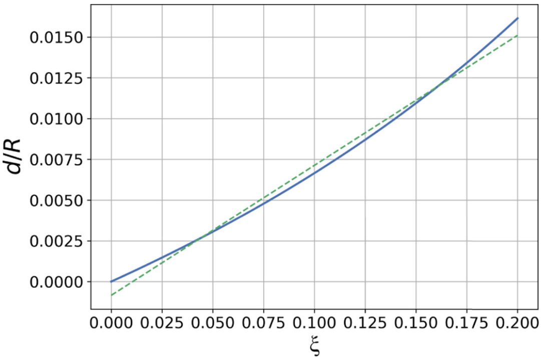

Fig. 11. Liquid layer thickness ratio d/R as a function of ξ. The blue solid line shows the predicted values of d/R for $V_i = 5$ with the straight green dashed line used to illustrate the linearity.

C and G_0^+, respectively. Fig. 9 shows the predicted coefficient of restitution for ice particles colliding with an ice wall together with the experimental measurements from the present work. As shown in the figure, the new formulation for the energy loss captures the rapid increase of energy dissipation with increasing V_i, and also captures the difference between temperatures. The new model predicts that e_n approaches zero for a finite value of V_i which is different from Eq. (3) where e_n only approaches zero as $V_i \rightarrow \infty$.

In Fig. 10 the model predictions of e_n for different wall materials and the experimental measurements for these wall materials are presented. The different wall materials are represented by different values of E^* where the material properties for the different walls are the same as used in a previous study [31] except that the Young modulus for ice is calculated as the function of temperature as in Hobbs [49]. Notably the new model predicts the trend between wall materials that is observed in the experiments.

The Eq. (15) solutions are plotted in Figs. 9-10 with $\xi = 0.15$. However, the value of ξ is not well defined and Wettlaufer [30] bounded ξ between 0.1 and 0.2. The dependency of ξ on d in Eq. (5) is almost linear for the range of velocities examined herein. Therefore, changes in ξ will only alter the constant K_1 in Eq. (14), and thus, as long as ξ is a constant. it will not matter what non-zero value is used for the prediction of E_v. Fig. 11 shows d/R as a function of ξ together with a linear dashed line to illustrate the linear dependence between d/R and ξ. The figure assumes $V_i = 5$ m/s, which is a high V_i in this work. The linearity further increases with decreasing velocity because the contribution of the contact pressure in Eq. (5) decreases.

As shown in Fig. 10, Eq. (14) provides a good fit to the experimental measurements for the ice particles with a diameter of 1.64 mm ($R = 0.82$ mm). To address how e_n will scale with a change in particle size we extracted the values of e_n published by Higa et al. [27] for ice particles with radii of 1.4 mm and 4.0 mm at $T = 261$ K. These results together with the e_n predicted by the new model are shown in Fig. 12. Again the model captures the trend that is observed in the experiments.

3.2. General regime map for the coefficient of restitution of ice particle collisions

The measurements we have presented complement existing measurements and lead us to propose a regime map for ice collisions. We identify three e_n regimes for ice particle collisions: an intermolecular adhesive regime, a collisional melting regime, and a fragmentation regime. The intermolecular adhesive regime is characterized by damping due to intermolecular forces. In previous work [31], we studied when an ice particle sticks or bounces depending on intermolecular forces. Based on the Johnson-Kendall-Roberts (JKR) model, at low V_i, e_n can be defined as,

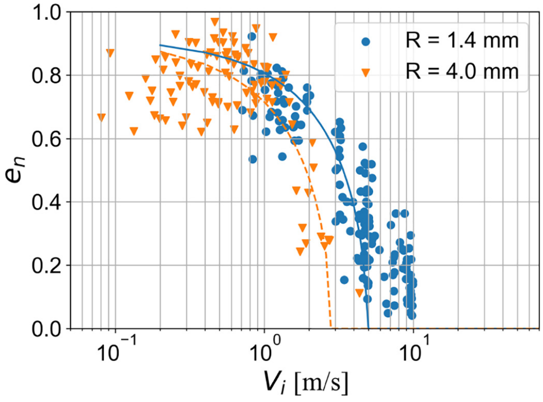

Fig. 12. The e_n for ice particles colliding with an ice wall at $T = 261$ K. Scattered with circles and triangles show experimental results published in Higa et al. [27] for radii 1.4 mm and 4.0 mm respectively. Dashed and solid lines show the novel model predictions for 1.4 mm and 4.0 mm radii, respectively.

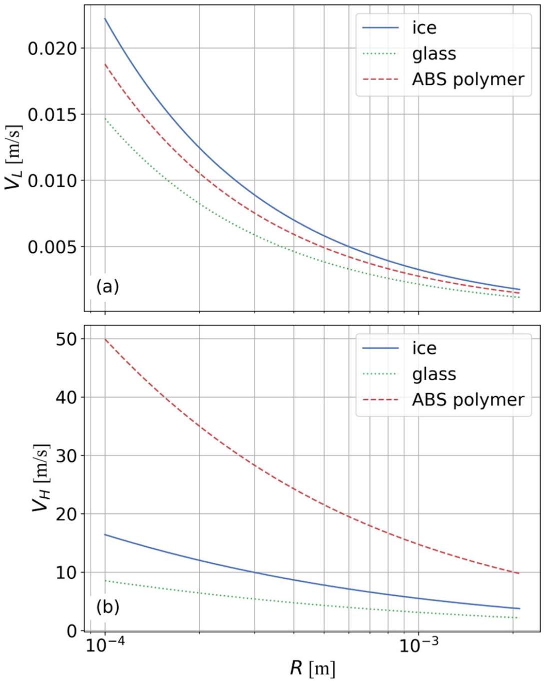

Fig. 13. The sticking velocities V_L (a) and V_H (b) for ice particles colliding with different massive walls as a function of R at $T = 261$ K. Solid, dashed and dotted lines shows the calculated sticking velocities for ice particles colliding with an ice wall, a polymer wall and a glass wall respectively. In (a) below each respective line particles sticking will occur. In (b) above each respective line particles sticking will occur.

$$e_n = \sqrt{1-\left(\frac{V_L}{V_i}\right)^2}, \tag{16}$$

where V_L is the lower sticking velocity and for collisional velocities below V_L, particles stick due to intermolecular adhesion. This lower sticking velocity is defined as,

$$V_L = \frac{3\sqrt{3}}{4}\sqrt{\frac{K_1}{\rho_s}}\left(\frac{\pi^2 W^5}{R^5 E^{*2}}\right)^{\frac{1}{6}}. \tag{17}$$

where $K_1 \approx 0.9355$ is an integration constant [31]. From Eq. (17) it can be seen that the V_L is mainly governed by the interaction properties E^* and W (work of adhesion), but will also increase with decreasing R. The collisional melting regime is defined by Eq. (15). In this regime an ice particle colliding with a massive wall will have a rapid increase in energy loss with increasing V_i until the particle begins to adhere to the wall. This will occur when the incoming kinetic energy is equal to the sum of energy causing damage at the interface and the energy lost due to viscous damping. This condition results in a separate, higher sticking velocity, V_H, that can be defined as,

$$V_H = \frac{3C}{2\pi(1-\xi)}\exp\left(\frac{G_0^+}{k_b T}\right)(d_H/\varepsilon)^{1.5}, \tag{18}$$

where d_H is the melted liquid layer thickness when this sticking occurs. However, d_H is a nonlinear function of V_i, as seen in Eq. (5) and therefore it is not possible to derive an explicit equation for the V_H and Eq. (18) can only be solved implicitly. In Fig. 13 the sticking velocities V_L and V_H are plotted as a function of R for ice particles colliding with an ice wall, a polymer wall and a glass wall at $T = 261$ K. As concluded by Eidevåg et al. [31], a polymer wall will have a higher V_L than a glass wall which means that a polymer wall will tend to accumulate more ice particles than a glass wall for V_i in the intermolecular adhesive regime. However, for high velocity collisions, where collisional melting dominates, a glass wall have a lower V_H than a polymer wall and therefore a glass wall is predicted to accumulate more ice particles than a polymer wall for V_i in the collisional melting regime.

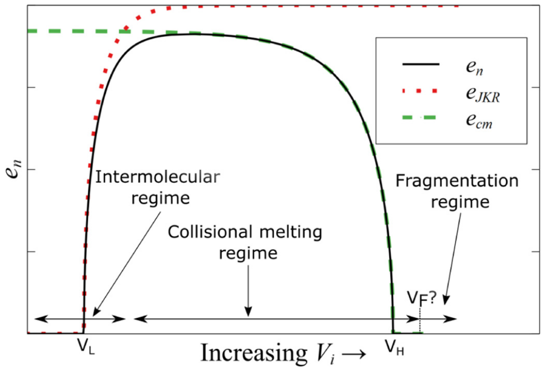

Fig. 14. The coefficient of restitution for ice particles upon collision with a massive wall. The red dotted line (e_{JKR}) shows the coefficient of restitution due to intermolecular forces. The dashed green line (e_{cm}) shows the coefficient of restitution due to collisional melting, and a fragmentation regime is also indicated where the e_n becomes undefined. The combined e_n is shown by the black solid line.

For even greater velocities ice particles will continue to adhere until fragmentation begins to influence the impacts at a certain fragmentation velocity V_F. Particles at these velocities, in excess of collisional fusion, will rebound but simultaneously fragment. Previous experiments have shown that for high velocity impacts, particles rebound and lose energy due to fragmentation but partial fragments may adhere to the wall [50]. Experimental data in this range is lacking and the e_n for such impacts is ill-defined given that the impacting particle will not remain intact.

The outlined regimes can be convoluted to yield a map for ice particle impacts (Fig. 14). In the figure, e_n is the convoluted coefficient of restitution that emerges from considering, e_{JKR} due to intermolecular forces and e_{cm} due to collisional melting. A fragmentation regime is indicated for velocities above an unknown V_F to illustrate that this is an experimentally unexplored region. The sticking velocities V_L and V_H are also indicated in the figure. The combined model predicts a horizontal plateau around the point $e_n = \sqrt{1-\xi^2}$ and this demostrates why previous studies have proposed a quasi-static regime for the e_n of ice particles. However, the new combined model also predicts that e_n will decrease for V_i below this point.

4. Conclusions

In this study we have investigated the damping mechanisms of ice particles that collide with walls, specifically in terms of the coefficient of restitution e_n. Experimental measurements of e_n for millimeter-sized particles at different temperatures and for different wall materials were presented. We obtain a velocity dependent e_n, similar to what has previously been observed by Higa et al. [27]. Different magnitudes of e_n for ice particles colliding with different wall materials were also obtained. Collisions with a polymer wall had the highest e_n and collisions with a hardened glass wall had the lowest e_n.

We propose that the rapid energy dissipation for ice particles colliding with walls can be explained by collisional melting and the associated viscous damping the increased premelted liquid-layer causes in a collision. A novel model has been derived that captures obtained temperature dependencies and observed differences attributed to wall material properties. We combined the new model with previous work [31] and proposed a regime map for the e_n of ice particles.

Nomenclature

e_n	normal coefficient of restitution (−)
V_i	normal impact velocity (m/s)
V_b	normal rebound velocity (m/s)
V_c	critical damping velocity (m/s)
V_L	lower sticking velocity (m/s)
V_H	higher sticking velocity (m/s)
d	liquid layer thickness (m)
ρ_s	density of solid water (kg/m3)
ρ_f	density of liquid water (kg/m3)
k_b	Boltzmann constant (eV/K)
E^*	effective Young's modulus (Pa)
T	experimental temperature (K)
T_m	melting temperature (K)
T_H	homologous temperature (−)
η	viscosity of the liquid layer (Pa-s)
ε	particle roughness length scale (m)
F_v	viscous force (N)
E_v	energy loss due to viscous damping (J)
R	particle radius (m)
W	work of adhesion (J/m2)
ξ	fraction of kinetic energy causing damage at interface (−)
q_m	latent heat of fusion (J)
δa	uncertainty of quantity a

Declaration of Competing Interest

Acknowledgments

The authors are grateful to Arctic Falls AB for making their facilities available for the experiments. We thank Per Gren at Luleå University of Technology for his help with the experimental setup. This work was funded by VINNOVA (2017-03029). EST is supported by the Swedish Research Council FORMAS (2017-00564) and Swedish Research Council VR (2020-03497), and by the Swedish Strategic Research Area MERGE.

References

[1] J. Blum, Dust evolution in Protoplanetary discs and the formation of planetesimals, Space Sci. Rev. 214 (2018) 1–19, https://doi.org/10.1007/s11214-018-0486-5.

[2] J.G. Dash, B.L. Mason, J.S. Wettlaufer, Theory of charge and mass transfer in ice-ice collisions, J. Geophys. Res. 106 (2001) 395–415, https://doi.org/10.1029/2001JD900109.

[3] R.A. Schmidt, Properties of blowing snow, Rev. Geophys. 20 (1982) 39–44, https://doi.org/10.1029/RG020i001p00039.

[4] P.O.A. Borrebæk, B.P. Jelle, Z. Zhang, Avoiding snow and ice accretion on building integrated photovoltaics – challenges, strategies, and opportunities, Sol. Energy Mater. Sol. Cells 206 (2020)https://doi.org/10.1016/j.solmat.2019.110306.

[5] B.E.K. Nygaard, H. Ágústsson, K. Somfalvi-Tóth, Modeling wet snow accretion on power lines: improvements to previous methods using 50 years of observations, J. Appl. Meteorol. Climatol. 52 (2013) 2189–2203, https://doi.org/10.1175/JAMC-D-12-0332.1.

[6] P. Abrahamsson, M. Eng, A. Rasmuson, An infield study of road snow properties related to snow-car adhesion and snow smoke, Cold Reg. Sci. Technol. 145 (2018) 32–39, https://doi.org/10.1016/j.coldregions.2017.09.008.

[7] M. Sommerfeld, Modelling of particle-wall collisions in confined gas-particle flows, Int. J. Multiphase Flow 18 (1992) 905–926, https://doi.org/10.1016/0301-9322(92)90067-Q.

[8] S. Matsusaka, H. Maruyama, T. Matsuyama, M. Ghadiri, Triboelectric charging of powders: a review, Chem. Eng. Sci. 65 (2010) 5781–5807, https://doi.org/10.1016/j.ces.2010.07.005.

[9] C. Thornton, Granular Dynamics, Contact Mechanics and Particle System Simulations: A DEM Study, vol. 24, Springer International Publishing, 2015 https://doi.org/10.1007/978-3-319-18711-2.

[10] J. Marshall, S. Li, Adhesive Particle Flow: A Discrete-Element Approach, Cambridge University Press, Cambridge, 2014 https://doi.org/10.1017/CBO9781139424547.

[11] J. Marshall, Modeling and sensitivity analysis of particle impact with a wall with integrated damping mechanisms, Powder Technol. 339 (2018) 17–24, https://doi.org/10.1016/j.powtec.2018.07.097.

[12] R. Boettcher, S. Eichmann, P. Mueller, Influence of viscous damping and elastic waves on energy dissipation during impacts, Chem. Eng. Sci. 199 (2019) 571–587, https://doi.org/10.1016/j.ces.2019.01.036.

[13] S. Aman, P. Mueller, J. Tomas, S. Kozhar, M. Dosta, S. Heinrich, S. Antonyuk, Combined viscoelastic and elastic wave dissipation mechanism at low velocity impact, Adv. Powder Technol. 27 (2016) 1244–1250, https://doi.org/10.1016/j.apt.2016.04.012.

[14] K.L. Johnson, H.M. Pollock, The role of adhesion in the impact of elastic spheres, J. Adhes. Sci. Technol. 8 (1994) 1323–1332, https://doi.org/10.1163/156856194X00636.

[15] N.V. Brilliantov, T. Pöschel, Collision of adhesive viscoelastic particles, Phys. Granular Media (2005) 189–209, https://doi.org/10.1002/352760362X.ch8 arXiv:0506253v1.

[16] C. Thornton, Z. Ning, A theoretical model for the stick/bounce behaviour of adhesive, elastic- plastic spheres, Powder Technol. 99 (1998) 154–162, https://doi.org/10.1016/S0032-5910(98)00099-0.

[17] S. Antonyuk, S. Heinrich, N. Deen, H. Kuipers, Influence of liquid layers on energy absorption during particle impact, Particuology 7 (2009) 245–259, https://doi.org/10.1016/j.partic.2009.04.006.

[18] B. Buck, S. Heinrich, Collision dynamics of wet particles: comparison of literature models to new experiments, Adv. Powder Technol. 30 (2019) 3241–3252, https://doi.org/10.1016/j.apt.2019.09.033.

[19] F. Gollwitzer, I. Rehberg, C.A. Kruelle, K. Huang, Coefficient of restitution for wet particles, Phys. Rev. E – Statist. Nonlinear Soft Matter Phys. 86 (2012) 1–9, https://doi.org/10.1103/PhysRevE.86.011303 arXiv:1202.1750.

[20] V.S. Sutkar, N.G. Deen, J.T. Padding, J.A. Kuipers, V. Salikov, B. Crüger, S. Antonyuk, S. Heinrich, A novel approach to determine wet restitution coefficients through a unified correlation and energy analysis, AICHE J. 61 (2015) 769–779, https://doi.org/10.1002/aic.14693.

[21] M. Khalilitehrani, J. Olsson, A. Rasmuson, F. Daryosh, A regime map for the normal surface impact of wet and dry agglomerates, AICHE J. 64 (2018) 1975–1985, https://doi.org/10.1002/aic.16072.

[22] J.P. Dilley, Energy loss in collisions of icy spheres: loss mechanism and size-mass dependence, Icarus 105 (1993) 225–234, https://doi.org/10.1006/icar.1993.1120.

[23] K.D. Supulver, F.G. Bridges, D. Lin, The coefficient of restitution of ice particles in glancing collisions: experimental results for unfrosted surfaces, Icarus 113 (1995) 188–199, https://doi.org/10.1006/ICAR.1995.1015.

[24] I.V. Roisman, C. Tropea, Impact of a crushing ice particle onto a dry solid wall, Proceed. Roy. Soc. A: Math. Phys. Eng. Sci. 471 (2015) https://doi.org/10.1098/rspa.2015.0525.

[25] C.R. Hill, D. Heißelmann, J. Blum, H.J. Fraser, Collisions of small ice particles under microgravity conditions, Astron. Astrophys. 573 (2015) A49, https://doi.org/10.1051/0004-6361/201424069 arXiv:1411.0563.

[26] C. Güttler, D. Heißelmann, J. Blum, S. Krijt, Normal Collisions of Spheres: A Literature Survey on Available Experiments, URL: http://arxiv.org/abs/1204.0001 2012arXiv:1204.0001.

[27] M. Higa, M. Arakawa, N. Maeno, Size dependence of restitution coefficients of ice in relation to collision strength, Icarus 133 (1998) 310–320, https://doi.org/10.1006/icar.1998.5938.

[28] S.C. Colbeck, An overview of seasonal snow metamorphism, Rev. Geophys. Space Phys. 20 (1982) 45–61, https://doi.org/10.1029/RG020i001p00045.

[29] A. Langlois, A. Royer, B. Montpetit, A. Roy, M. Durocher, Presenting snow grain size and shape distributions in Northern Canada using a new photographic device allowing 2D and 3D representation of snow grains, Front. Earth Sci. 7 (2020) https://doi.org/10.3389/feart.2019.00347.

[30] J.S. Wettlaufer, Accretion in protoplanetary disks by collisional fusion, Astrophys. J. 719 (2010) 540–549, https://doi.org/10.1088/0004-637X/719/1/540.

[31] T. Eidevåg, P. Abrahamsson, M. Eng, A. Rasmuson, Modeling of dry snow adhesion during normal impact with surfaces, Powder Technol. 361 (2019) 1081–1092, https://doi.org/10.1016/j.powtec.2019.10.085.

[32] M. Vargas, P.M. Struk, R.E. Kreeger, J. Palacios, K.A. Iyer, R.E. Gold, Ice Particle Impacts on a Moving Wedge, 2013 https://doi.org/10.2514/6.2014-3045.

[33] B. Crüger, V. Salikov, S. Heinrich, S. Antonyuk, V.S. Sutkar, N.G. Deen, J.A. Kuipers, Coefficient of restitution for particles impacting on wet surfaces: an improved experimental approach, Particuology 25 (2016) 1–9, https://doi.org/10.1016/j.partic.2015.04.002.

[34] J.Y. Tinevez, N. Perry, J. Schindelin, G.M. Hoopes, G.D. Reynolds, E. Laplantine, S.Y. Bednarek, S.L. Shorte, K.W. Eliceiri, TrackMate: an open and extensible platform for single-particle tracking, Methods 115 (2017) 80–90, https://doi.org/10.1016/j.ymeth.2016.09.016.

[35] K.L. Johnson, Contact Mechanics, Cambridge University Press, Cambridge, 1985https://doi.org/10.1017/CBO9781139171731.

[36] B. Yildirim, H. Yang, A. Gouldstone, S. Müftü, Rebound mechanics of micrometre-scale, spherical particles in high-velocity impacts, Proceed. Roy. Soc. A: Math. Phys. Eng. Sci. 473 (2017) https://doi.org/10.1098/rspa.2016.0936.

[37] K. Hashemnia, Experimental study of the effect of temperature on the coefficient of restitution of steel balls impact to some industrial metal sheets at elevated temperatures, Powder Technol. 368 (2020) 170–177, https://doi.org/10.1016/j.powtec.2020.04.053.

[38] J. Grau-Bove, C. Mangwandi, G. Walker, D. Ring, K. Cronin, Studies into the effect of temperature on the impact of model particles in co-melt granulation, Powder Technol. 294 (2016) 411–420, https://doi.org/10.1016/j.powtec.2016.02.041.

[39] J.G. Dash, Haiying Fu, J.S. Wettlaufer, The premelting of ice and its environmental consequences, Rep. Prog. Phys. 58 (1995) 115–167, https://doi.org/10.1088/0034-4885/58/1/003.

[40] J.G. Dash, A.W. Rempel, J.S. Wettlaufer, The physics of premelted ice and its geophysical consequences, Rev. Mod. Phys. 78 (2006) 695–741, https://doi.org/10.1103/RevModPhys.78.695.

[41] T. Bartels-Rausch, H.W. Jacobi, T.F. Kahan, J.L. Thomas, E.S. Thomson, J.P. Abbatt, M. Ammann, J.R. Blackford, H. Bluhm, C. Boxe, F. Domine, M.M. Frey, I. Gladich, M.I. Guzmán, D. Heger, T. Huthwelker, P. Klán, W.F. Kuhs, M.H. Kuo, S. Maus, S.G. Moussa, V.F. McNeill, J.T. Newberg, J.B. Pettersson, M. Roeselová, J.R. Sodeau, A review of air-ice chemical and physical interactions (AICI): Liquids, quasi-liquids, and solids in snow, Atmos. Chem. Phys. 14 (2014) 1587–1633, https://doi.org/10.5194/acp-14-1587-2014.

[42] L. Benatov, J.S. Wettlaufer, Abrupt grain boundary melting in ice, Phys. Rev. E – Statist. Phys. Plasmas Fluids Related Interdiscip. Top. 70 (2004) 7, https://doi.org/10.1103/PhysRevE.70.061606 arXiv:0412747.

[43] E.S. Thomson, L. Benatov, J.S. Wettlaufer, Erratum: abrupt grain boundary melting in ice (Physical Review E - Statistical, Nonlinear, and Soft Matter Physics (2004) 70 (061606)), Phys. Rev. E – Statist. Nonliner Soft Matter Phys. 82 (2010), 61606, https://doi.org/10.1103/PhysRevE.82.039907.

[44] E.S. Thomson, H. Hansen-Goos, J.S. Wettlaufer, L.A. Wilen, Grain boundary melting in ice, J. Chem. Phys. 138 (2013) https://doi.org/10.1063/1.4797468 arXiv:1212.5508.

[45] S. Murakami, Continuum Damage Mechanics: A Continuum Mechanics Approach to the Analysis of Damage and Fracture, Springer, Netherlands, 2012https://doi.org/10.1007/978-94-007-2666-6.

[46] M.J. Matthewson, Adhesion of spheres by thin liquid films, Philosop. Magaz. A: Phys. Condens. Matter Struct. Defects Mech. Proper. 57 (1988) 207–216, https://doi.org/10.1080/01418618808204510.

[47] D.Y. Chan, R.G. Horn, The drainage of thin liquid films between solid surfaces, J. Chem. Phys. 83 (1985) 5311–5324, https://doi.org/10.1063/1.449693.

[48] R.B. Bird, W.E. Stewart, E.N. Lightfoot, Transport Phenomena, John Wiley & Sons Inc, 2006.

[49] P.V. Hobbs, Ice Physics, Oxford University Press, 1974.

[50] T. Hauk, I. Roisman, C. Tropea, Investigation of the impact behaviour of ice particles, 6th AIAA Atmospheric and Space Environments Conference, Atlanta, 2014 https://doi.org/10.2514/6.2014-3046.

PAPER III

Angle of repose of snow: An experimental study on cohesive properties

Cold Regions Science and Technology 194 (2022) 103470

Contents lists available at ScienceDirect

Cold Regions Science and Technology

journal homepage: www.elsevier.com/locate/coldregions

Angle of repose of snow: An experimental study on cohesive properties

Tobias Eidevåg [a,b,*], Erik S. Thomson [c], David Kallin [b], Johan Casselgren [d], Anders Rasmuson [a]

[a] *Department of Chemistry and Chemical Engineering, Chalmers University of Technology, SE-41296 Gothenburg, Sweden*
[b] *Contamination and Core CFD, Volvo Car Corporation, SE-40531 Gothenburg, Sweden*
[c] *Department of Chemistry & Molecular Biology, Atmospheric Science, University of Gothenburg, SE-41296 Gothenburg, Sweden*
[d] *Division of Fluid and Experimental Mechanics, Luleå University of Technology, SE-97187 Luleå, Sweden*

ARTICLE INFO

Keywords:
Snow cohesion
Angle of repose
Snow physics
Snow
Snow adhesion
Snow accumulation
premelting

ABSTRACT

The angle of repose is a measure reflecting the internal friction and cohesion properties of a granular material. In this paper, we present an experimental setup and measurements for the angle of repose of snow for seven different snow samples over a large range of temperatures. The results show that the angle of repose is dependent on the fall height, the temperature, and the grain size of the snow. These variables are quantified, and their interdependencies are separately studied. With increased snow temperature, the angle of repose increases, and this can be explained by the presence of a liquid layer on ice that can be thermodynamically stable at temperatures below the melting point of water. With decreasing grain size the angle of repose also increases which is expected since the cohesive energy decreases more slowly than the grain mass. For increasing fall height, the snow grains generally accelerate to larger collisional velocities, yielding a smaller angle of repose. In general, the dimensionless cohesion number was found to largely reflect the dependencies of the variables and is therefore useful for understanding what affects the angle of repose. The results demonstrate that the drag force and collision dynamics of ice grains are important for understanding how snow accumulates on a surface, for example if one desires predicting snow accretion by simulating a dispersed cloud of snow.

1. Introduction

The cohesive properties of snow are important in many engineering and scientific applications. One example is in avalanche research where it has been observed that the dynamic movement of snow covers is sensitive to temperature, especially when temperatures are above -1°C (Heil et al., 2018). Another example is snow accretion on building roofs, which has an influence on the efficiency of solar panels (Borrebæk et al., 2020) and can cause roof failure (Holicky and Sykora, 2009). The presented research is driven by a need in the automotive industry to better understand snow adhesion. Active safety and autonomous systems have increased the need to understand how snow accretes on vehicle sensors (Eidevåg et al., 2019). The phenomenon of snow accretion on sensor surfaces generally involves a dispersed cloud of snow grains that collide, adhere, and accumulate on these surfaces.

The angle of repose α of a granular material (illustrated in Fig. 1) is a micro-mechanical property that reflects the internal friction of the material (Al-Hashemi and Al-Amoudi, 2018). The α of a granular material can generally be regarded as a bulk material property but, as was pointed out by Woodcock and Mason (1988), measured values of α depend not only on the material but also on the experimental setup used. Snow is a cohesive material where the cohesive properties are contact-time dependent due to sintering. The bond strength between grains in contact increases over time, which causes static approaches to measuring α, such as using a tilting table, to be problematic. Instead, it is advantageous to use a dynamic approach with grains of snow that collide and accumulate to form a heap, as has previously been done when studying snow. To the best of our knowledge, Kuroiwa et al. (1967) were the first to measure the α of snow in this way. In their experiments, they used a hopper to shake snow that then fell through a funnel onto a cylindrical platform. They released snow until a stable heap had been obtained such that α could be measured. They observed that α increased with increasing snow temperature T for $T > -20^\circ$C, and they related their findings to the presence of a liquid-layer on ice that can be thermodynamically stable at T well below the melting temperature of water (Jellinek, 1967; Dash et al., 1995; Dash et al., 2006). They observed a sensitivity to fall height H with larger H yielding smaller α. Willibald et al. (2020) proposed a similar experimental setup where the hopper and funnel were replaced with a sieve. They studied how snow grain shape and T affect the snow's α. They have proposed an empirical model based on their measurements that takes into account

---

* Corresponding author at: Contamination and Core CFD, Volvo Car Corporation, SE-40531 Gothenburg, Sweden
E-mail address: tobias.eidevag@volvocars.com (T. Eidevåg).

https://doi.org/10.1016/j.coldregions.2021.103470
Received 16 July 2021; Received in revised form 27 October 2021; Accepted 15 December 2021

Nomenclature

A_p	grain cross-section area (m^2)
Co	Cohesion number
D_B	base diameter (m)
d_A	projected area diameter (m)
d_V	volume-weighted mean projected area diameter (m)
E^*	effective Young's modulus (Pa)
g	gravitational constant (m/s^2)
G^+	activation energy (eV)
H	fall height (m)
h	heap height (m)
k_b	Boltzmann constant (eV/K)
P	length of grain boundary (m)
R^*	effective grain radius (m)
s	surface area of sphere (m^2)
S	surface area of grain (m^2)
T	snow temperature (K)
V_i	collisional velocity (m/s)
V_∞	terminal velocity (m/s)
L_e	distance top of inner table to cylinder (m)
L_h	distance top of inner table top to snow heap (m)
W	work of adhesion (J/m^2)
α	angle of repose (°)
δa	uncertainty of quantity a
ϕ	sphericity
$\widehat{\phi}$	circularity
σ	standard deviation
ρ_p	particle density (kg/m^3)

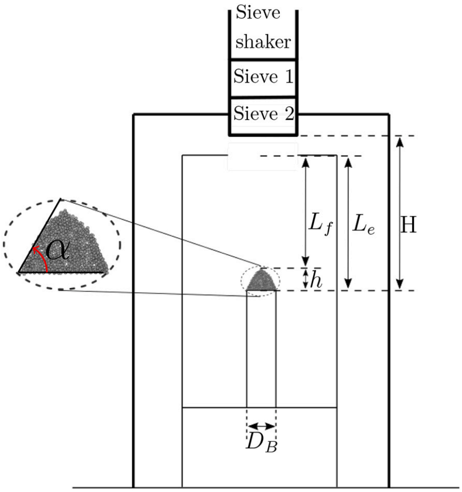

Fig. 1. Experimental setup with important dimensions labeled and the α of snow highlighted in the inset.

shape and T to predict α. In both studies, α was found to be sensitive to T for $T > -15°C$, but few data points were published for this range. The previous studies were also based on relatively large grain sizes and no data for α of snow with an average grain size less than 500 μm has been published, to the best of our knowledge.

In this work, we present and analyze new experimental results for the angle of repose of snow for multiple temperatures greater than $-15°C$ and particles as small as 100 μm. The observations allow us to characterize snow's α as a function of shape, size, T, and H.

The results extend the understanding of the cohesive properties of snow and ice. We show that cohesion is sensitive to T, collisional velocity, and grain properties. The data from this work can be used as validation when simulating snow adhesion and the buildup of snow, for example, using the Discrete Element Method or Smoothed Particle Hydrodynamics. The α for rounded grains at varying T and H reported in this work can also be referred to when validating the cohesive properties of machine made snow.

2. Method and materials

2.1. Experimental setup

Experiments were performed to measure α for different snow samples at different experimental conditions. The experimental setup consisted of a large metal table that held an electric sieve shaker with two sieves (sieve 1 and sieve 2) and a smaller metal table with a solid cylindrical base with diameter D_B (Fig. 1). The purpose of sieving was to shake the snow to separate individual grains. Sieve 1 and 2 had pore sizes 3.15 mm and 2.5 mm, respectively.

An experimental trial was performed by pouring snow into the sieve shaker and shaking the snow sequentially through sieve 1 and sieve 2. The snow grains from sieve 2 fell until they hit the cylinder under the sieve shaker. A growing snow heap formed as more grains accumulated on the cylinder base. Snow was continuously fed into the sieve shaker as long as snow continued to accumulate on the heap. A trial was completed when the height of the cylindrical cone h stopped changing with time, and a measurement usually took a few minutes to complete. To estimate α, h was calculated as

$$h = L_e - \left(L_f + c\right), \tag{1}$$

where L_e is the distance between the top of the inner table and the platform without any snow, and L_f is the distance between the top of the inner table and the top of the snow heap. Ideal cones with a sharp vertex at the top of the cone did not always form, and therefore, the length c (as illustrated in Fig. 2) was added as a correction factor.

With the obtained h, α can be calculated as

$$\alpha = arctan\left(\frac{2h}{D_B}\right). \tag{2}$$

The calculated h was estimated to have an uncertainty of $\delta h = 2$ mm, which emerges from measurement uncertainties. The result is a nonlinear and asymmetrical confidence interval for α. However, arctan (x) is a monotonically increasing function and the asymmetry was minor for the values reported in this work. The confidence interval was, therefore, simplified to

$$\alpha \pm \delta\alpha \approx \pm\left(arctan\left(\frac{2(h+\delta h)}{D_B}\right)\right). \tag{3}$$

Alternatively, α could also be measured with image analysis either indirectly using the projected heap area or directly by measuring the angle (Willibald et al., 2020). These methods are sensitive to camera angle, and because the image quality varied in this work, we found that the snow cone height estimate gave the most robust estimate for α.

Experimental trials were conducted with each snow sample and at

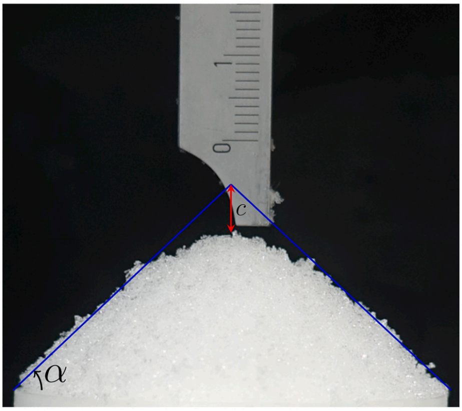

Fig. 2. Illustration of how the height measurements were corrected by adding the length c to the imperfect cone height.

each experimental condition. Average values combining multiple trials were computed, and a conservative error envelope was estimated as,

$$\delta\alpha = max(\delta\alpha_{max}, 2\sigma), \tag{4}$$

where $\delta\alpha_{max}$ is the largest obtained $\delta\alpha$ of the measurements, and σ is the standard deviation of α for the repetitions.

Previous work on the α of snow has shown that α is independent of D_B (Kuroiwa et al., 1967; Willibald et al., 2020). This was also observed in this work when testing diameters from 25 to 100 mm. $D_B = 50$ mm was used in the experiments for the majority of measurements if not stated otherwise, which is the same D_B used by Kuroiwa et al. (1967) and Willibald et al. (2020).

2.2. Snow samples

Snow samples were collected in containers, and total volumes of 20–30 l were collected for each sample. A sample was defined as a collection of snow at a specific time and place. The samples were labeled using the snow shape classes defined in Fierz et al. (2009), and the labels are summarized in Table 1. The samples RG 1, RG 2, RG 3, PP 1, and SH 1 were collected from the ground outdoors, and only the top layer of snow was collected. The sample RG 4 was collected from an underbody panel on an electric vehicle driven 100 km on a snowy road at the same location and during the same period as RG 3. The machine made snow (MM 1 sample) was collected from the ground in a climate wind-tunnel where the snow was created with a snow cannon.

Table 1
Snow characterization and experimental conditions for snow samples. The labels indicate: RG round grains, MM machine made snow, PP precipitation particles and SH surface hoar.

Label	$\widehat{\phi}_m$	d_V [μm]	T [°C]	H [m]
RG 1	0.70	455	−2 to −14	0.07–0.34
RG 2	0.75	775	−1 to −14	0.07–0.25
RG 3	0.72	492	−16 to −27	0.1–0.25
RG 4	0.82	288	−14	0.1–0.25
MM 1	0.95	80	−9 to −13	0.1–0.34
PP 1	N/A	N/A	−12	0.1
SH 1	N/A	N/A	−14	0.1

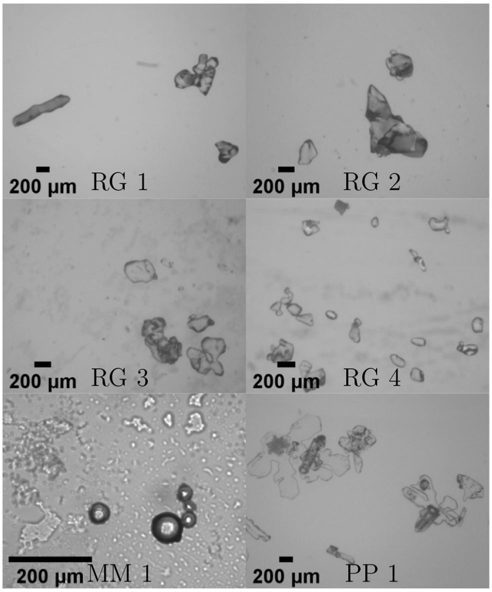

Fig. 3. Typical microscope images taken of six snow samples.

Each sample was characterized by placing microscope slides just below the sieve shaker and collecting particles from each sample onto the slides. The slides were then photographed using a microscope. Fig. 3 shows examples of microscope images for all the snow samples, except for the SH 1 sample. The magnification was similar for each sample except for the MM 1 sample, which had a higher magnification due to its small grain sizes. The grain boundaries for each image were extracted with manual segmentation of each boundary using the image analysis program Fiji, and the segments were analyzed to extract grain properties characteristic for each sample. On average, 450 grain boundaries were extracted for each sample with a minimum number of 291 for RG 1. Two properties were extracted for each grain: the projected area diameter, d_A, and the circularity, $\widehat{\phi}$. d_A and $\widehat{\phi}$ are defined as

$$d_A = \sqrt{\frac{4A_p}{\pi}}, \tag{5}$$

and

$$\widehat{\phi} = \frac{4\pi A_p}{P}, \tag{6}$$

where A_p is the grain cross-section area, and P is the length of the grain boundary. $\widehat{\phi}$ was used as an approximation of the sphericity, ϕ, since the microscope slides contained only 2D data, and ϕ is a 3D measure containing the surface area of a grain, defined as

$$\phi = \frac{s}{S}, \tag{7}$$

where s is the surface area of a sphere with the same volume as the grain, and S is the surface area of the grain. However, $\widehat{\phi}$ is often used as an approximation of ϕ, for example for volcanic particles (Bagheri and Bonadonna, 2016).

Experiments measuring α were performed either in cooling chambers or outdoors, depending on the snow sample. The air temperature in the cooling chambers could be controlled. The samples RG 1, RG 2, and PP 1 were measured in a cooling chamber with high precision control of the temperature (±0.5°C), while RG 3 was measured in a cooling chamber with low precision control of the temperature (±2°C). Samples RG 4 and SH 3 were measured outdoors. The measurements of the samples RG 1 and RG 2 are the largest datasets of α in this work, where multiple trials with varying T and H were performed. These two samples were stored in a cooling chamber before measurements to allow the grains to approach an equilibrium shape by means of snow metamorphism. Sample RG 1 was collected after outdoor dry snow metamorphism at a temperature of -5°C and stored for 3 weeks before testing. Sample RG 2 was collected after wet snow metamorphism at a temperature of 0°C and was stored at $T = -5^{\circ}$C for 4 days before testing.

The grain properties, d_A and $\widehat{\phi}$, for the different snow samples were visualized using a binned histogram showing the normalized frequency of d_A (Fig. 4 and Fig. 5) and a box-plot centered around the median for $\widehat{\phi}$ (Fig. 6). The histograms were normalized such that the sum of the bin heights for each sample is equal to 1. Particle properties, d_A and $\widehat{\phi}$ were not calculated for the PP 1 and SH 1 samples due to the observed shape complexities of these samples. The volume-weighted average projected area diameter d_V, and the median circularity $\widehat{\phi}_m$, for each snow sample are summarized in Table 1. The volume-weighted average was used to weight the volumetric effect a grain has on the overall volume of a snow heap. The MM 1 sample was significantly smaller than any other sample, with $\widehat{\phi} \approx 1$, two properties that are common for machine made snow from snow cannons (Fierz et al., 2009). The d_A range from $100 - 1000$ μm for the rounded grain samples, which implies that the sieve size of 2.15 mm was sufficiently large for the studied snow samples. The RG 4 sample had significantly smaller d_A than any of the other rounded grains, which implies that the collection method used for this sample acted as a grain-size filtering method, where only the smallest grains were lifted by the vehicle and accumulated on the underbody panel. This has been reported before, for example, Abrahamsson et al. (2018) have concluded that the snow that accumulates on the rear of a car is a subset of smaller particles than those present on the ground.

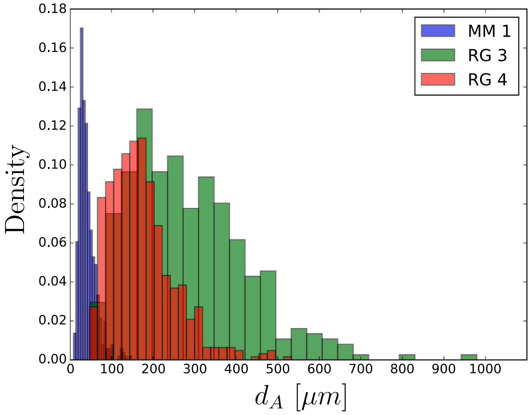

Fig. 5. Normalized particle size distributions determined from image analysis for snow samples MM 1, RG 3, and RG 4.

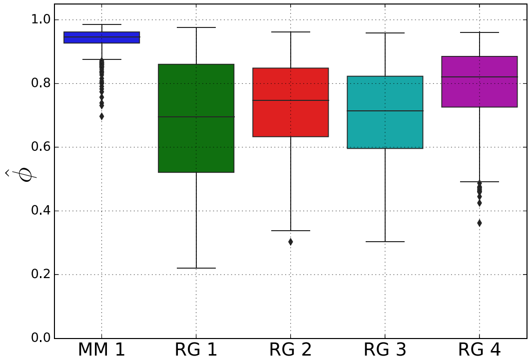

Fig. 6. Snow grain circularity $\widehat{\phi}$ determined from image analysis.

2.3. Experimental data interpretation

The Johnson-Kendall-Roberts (JKR) model has previously been extensively used to predict cohesive forces between ice grains (Eidevåg et al., 2019; Chokshi et al., 1993; Dominik and Tielens, 1997) and we will here use the JKR model to interpret our experimental observations. The model predicts that the cohesive sticking energy E_s for a colliding grain with diameter d, is proportional to $d^{4/3}$ and will thus decrease with decreasing grain size. The gravitational and kinetic energy acting against the cohesion will also be proportional to d but in this case $\propto d^3$ meaning it will decrease faster than the cohesion energy for a decreasing grain size. Therefore, cohesion is predicted to dominate over the grain mass for sufficiently small grains and grains will be more cohesive the smaller they are. To better understand these dependencies, we define a dimensionless number Co (the cohesion number) as the ratio between E_s and the kinetic energy at impact, E_i for a single grain impacting a solid wall. Our definition is similar to one proposed by Behjani et al. (2017), except here we use kinetic energy instead of gravitational potential energy. Using the expression for E_s (Eq. 11 in Eidevåg et al. (2019)) and $R^* = 0.5d$, it follows that

$$Co = \frac{E_s}{E_i} \approx \frac{5}{\rho_p V_i^2} \left(\frac{\pi^2 W^5}{d^5 E^{*2}} \right)^{1/3}, \tag{8}$$

where V_i is the grain collisional velocity, E^* is the effective Young's modulus, W is the work of adhesion and ρ_p is the grain density. For the snow samples in this work, all samples consist of a wide range of grain sizes and to simplify the analysis we will assume that the volume weighted average reflects the overall grain sizes in each sample ($d \approx d_V$).

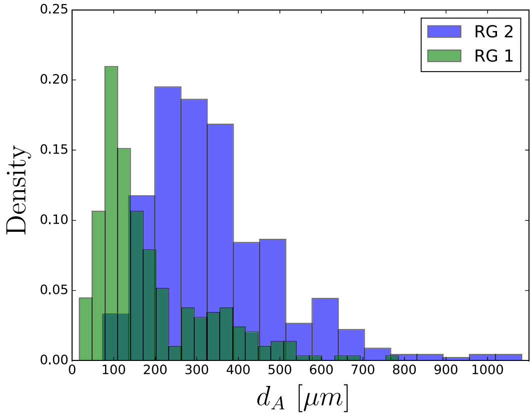

Fig. 4. Normalized particle size distributions determined from image analysis for snow samples RG 1 and RG 2.

3. Results and discussion

3.1. General

The α of snow for the different snow samples with $H = 0.1$ m as a function of T are shown in Fig. 7. All measurements presented in this

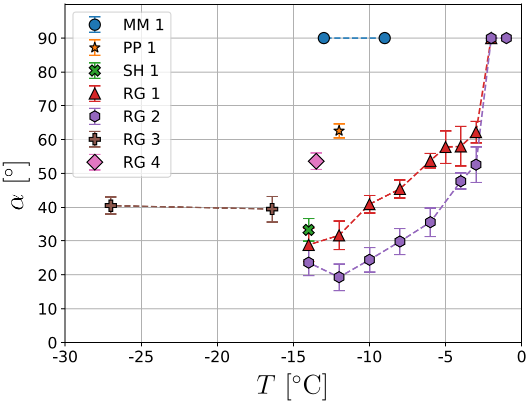

Fig. 7. The α of snow for the different snow samples as a function of T with H = 0.1 m, where the mean values of repeated trials are plotted with the error bars representing $\delta\alpha$.

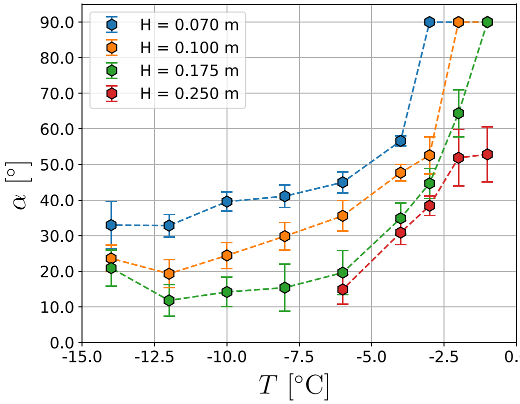

Fig. 9. The α of snow for RG 2 as a function of T for different H, where the mean values of repeated trials are plotted with the error bars representing $\delta\alpha$.

figure were done with $D_B = 50$ mm, except for the RG 4 data, where both 40 mm and 50 mm were used. The figure shows the average values from multiple trials with error bars representing $\delta\alpha$. The experiments generally had good repeatability, which is shown in Appendix A. The magnitude of the α for the different samples varied, for example, the PP 1 sample had an average $\alpha = 62^\circ$ while SH 1 had $\alpha = 33^\circ$, even though the difference in temperature was minor. Both samples had grains with complex crystalline shapes, but the observed difference implies different cohesion properties. This is in line with previous snow research that has shown that hoar grains have low-cohesive bonds, and they can cause avalanches when present as a layer deep in a snowpack (depth hoar) (Colbeck, 1997; Schweizer and Jamieson, 2001). The results for RG 1 and RG 2 imply that α is strongly dependent on T, which was also observed when H was varied, as shown in Fig. 8 and Fig. 9. At low enough T, lower than -10 or -12 °C, α appears to be constant and independent of T. It was only possible to measure α for the height $H = 0.25$ m above a certain T (-10°C for RG 1 and -6°C for RG 2) for these two samples. Almost all snow grains bounced away from the base, and no heap of snow formed below this T. This implies a limitation of the experimental setup, where $\alpha \leq 10^\circ$ could not be measured.

In certain trials $\alpha = 90^\circ$ was observed, indicating that a cylindrical snow heap had formed. The snow heap height observed in these trials increased until the heap touched the sieves. We refer to this phenomenon hereinafter as diverging α, since the α was not well defined. The phenomenon, however, remains interesting because it indicates when cohesive forces dominate over gravity. Fig. 10 shows an example of diverging α for snow sample RG 2 with $T = -1$°C and $H = 0.1$ m. Diverging α occurred for RG 1 and RG 2 at certain low values of H in combination with T above certain values. We observed diverging α in all measurements of sample MM 1 although the experiments were conducted at a low temperature ($T = -13$ °C). This implies that the MM 1 was more cohesive than any of the other snow samples.

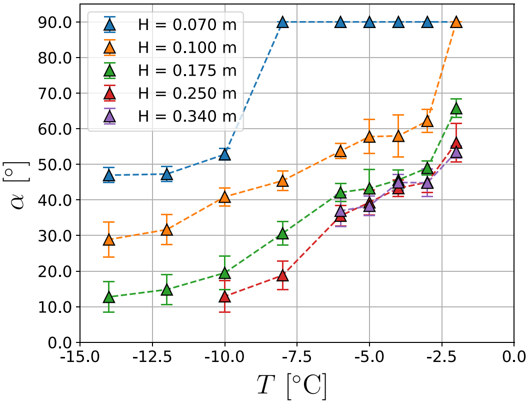

Fig. 8. The α of snow for RG 1 as a function of T for different H, where the mean values of repeated trials are plotted with the error bars representing $\delta\alpha$.

Fig. 10. Experimental trial with diverging α for sample RG 2 with $T = -1$°C and $H = 0.1$ m.

3.2. Snow temperature

As shown in Figs. 8 and 9 α is sensitive to changes in T and a high T can lead to diverging α as the snow cohesion is strong. Fig. 11 shows α as a function of T for snow samples RG 1, RG 2, and RG 3, as well as measurements from previous studies by Kuroiwa et al. (1967) and Willibald et al. (2020). The data in this figure was measured with $H = 0.1$ m except for the data from Willibald et al. (2020), which used $H = 0.04$ m. The figure shows that α changes for $T \gtrsim -12^{\circ}$C. Below this temperature range, α appeared constant and rather independent of T. A comparison with other experimental findings showed that the results reported by Willibald et al. (2020) were rather low given that H was only 0.04 m. This could be due to the larger grains in their samples; they reported grain sizes that ranged from $700 - 1400\,\mu$m. The α reported by Kuroiwa et al. (1967) is similar to the RG 3 sample with values around 40°.

Jellinek (1967) has studied the cohesion force between ice particles as a function of T. The results showed that cohesion increased with increasing T, and they proposed that the observed T dependency was caused by the existence of a liquid layer on ice that becomes thicker with increasing T. This phenomenon is often referred to as premelting and has been explained by the balance of the intermolecular forces at the surface of ice that causes a liquid layer to form at temperatures below the melting temperature of water (Dash et al., 1995; Dash et al., 2001; Wettlaufer and Worster, 2005; French et al., 2010). Jellinek, used the Arrhenius relation, $\propto \exp\left(-G^{+}/k_bT\right)$, to fit the cohesion force between ice particles as a function of temperature, where G^{+} is the activation energy, and k_b is the Boltzmann constant. It is common in ice physics to observe that ice properties have an Arrhenius relation with T. For example, it has been concluded that the creep rate of ice follows an Arrhenius relation but with a sudden increase of activation energy for T approximately above -15°C to -10°C (Weertman, 1983; Cuffey and Paterson, 2006; Goldsby and Kohlstedt, 2001). Goldsby and Kohlstedt (2001) credited this increase to premelting on the surface of ice.

Willibald et al. (2020) have proposed an empirical model for the α of snow, where they use the Arrhenius relation to capture the temperature dependence. Their model can be expressed as,

$$\alpha = A + B exp\left(-G^{+}/k_bT\right), \tag{9}$$

where A is a sum of the α for cohesionless spheres and a shape correction due to ϕ. In this model, B and G^{+} are free parameters. Willibald et al. (2020) obtained $B = 1.5 \cdot 10^{23}$ and $G^{+} = 1.2$ eV from curve fitting.

To extract the α dependence on T we performed curve fitting, where the averaged results for samples RG 1 and RG 2 were fitted to Eq. 9 for each individual H. We omitted data points with diverging α, and we have also omitted the data series with $H = 0.07$ m for sample RG 1, because it only contained 3 data points. The resulting least squares fits are shown in Table 2 for the parameters A, B, and G^{+} and for the correlation coefficient, R^2. We obtained almost identical activation energies with an average of $G^{+} = 1.15$ eV for the eight different series. The best fit of B was, on average, $1.03 \cdot 10^{23}$ with no obvious H dependence. We conclude, therefore, that α has a T dependence that follows an Arrhenius relation independent of H, and that the G^{+} we obtained was almost identical to the results reported by Willibald et al. (2020).

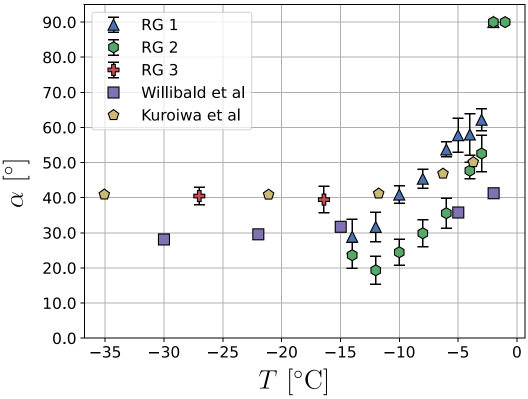

Fig. 11. The α of snow for samples RG 1, RG 2, and RG 3 as well as previously published results in Willibald et al. (2020) and Kuroiwa et al. (1967) as a function of T.

3.3. Grain size

The snow samples in this work had a large range of grain sizes. In Section 2.3 we introduced the cohesion number where $Co \propto d_V^{-5/3}$. How α depends on Co is unkown but it is expected that α increases for increasing Co and therefore, samples with smaller d_V should yield smaller α. Previous research has shown that α does depend on particle size and that α increases with decreasing particle size (Cadle, 1965). This can also be seen in our results for the RG 4 sample, which had a significantly higher α than the RG 3 sample, even though the type of grains and grain shape were similar. To assert how α depends on d_V we propose a dependence of the form $\alpha \propto a \cdot d_V{}^{b}$, for a constant a and an exponent b.

Fig. 12 shows the α for the snow samples RG 1, RG 2, RG 3, and MM 1 together with a curve fit assuming this proportionality. The effect of temperature difference between the samples was assumed to be negligible since, as shown in Section 3.2, the α dependence was expected to be small for $T \leq -12^{\circ}$C. The data for the MM 1 sample was excluded from the curve fitting since it is unknown if a diverging α also occurs for $d_V > 80\,\mu$m and the fitted line suggests that a diverging α may already occur for $d_V \approx 150\,\mu$m. The obtained best fit for the remaining four data points was $\alpha \propto d_V{}^{-0.86}$, which suggests that $\alpha \propto Co^{0.86 \cdot 3/5} \approx Co^{0.5}$, however, only a single data point was below 400 μm (RG 4). Thus, we regard the estimated exponent b as uncertain, but the results do show that samples with lower d_V have higher angles of repose.

3.4. Fall height and grain acceleration

Our results show that α is sensitive to H and generally decreases with increasing H. Fig. 13 shows α as a function of H for different samples of rounded grains, at different temperatures. α did not always decrease with an increase in H. Only small changes were observed between $H = 0.17$ m and $H = 0.25$ m, and no change was observed between $H = 0.25$ m and $H = 0.34$ m for RG 1. These observations can be explained by the acceleration of grains when falling. The acceleration of grains does also explain why some of the obtained α for high H is lower than what was previously reported by Willibald et al. (2020) for the α of snow.

When a grain falls in the experiments, it accelerates according to Newton's law of motion, where the acceleration is equal to the difference between the gravitational force and the drag force acting on the grain divided by grain mass. The grain accelerates until either it collides

Table 2
Least squares fits of Eq. 9 for the measured α for the RG 1 and RG 2 samples at varying H.

Sample	H	R^2	A	B	G^{+} (eV)
RG 1	0.10	0.93	27.84	$0.92 \cdot 10^{23}$	1.15
	0.17	0.95	9.58	$0.99 \cdot 10^{23}$	1.14
	0.25	0.93	4.64	$0.94 \cdot 10^{23}$	1.14
	0.34	0.93	21.86	$0.99 \cdot 10^{23}$	1.16
RG 2	0.07	0.96	28.51	$0.97 \cdot 10^{23}$	1.15
	0.10	0.97	15.32	$1.00 \cdot 10^{23}$	1.15
	0.17	0.85	6.08	$1.20 \cdot 10^{23}$	1.15
	0.25	0.90	1.00	$1.27 \cdot 10^{23}$	1.15

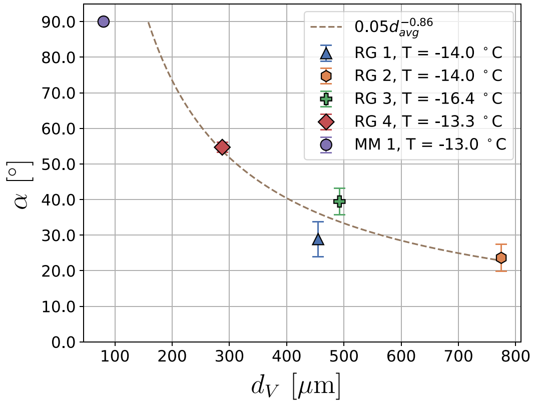

Fig. 12. The α of snow as a function of d_V for the samples RG 1, RG 2, RG 3, RG 4, and MM 1 with $H = 0.1$. The dashed line is the least-squares fitting of the RG samples.

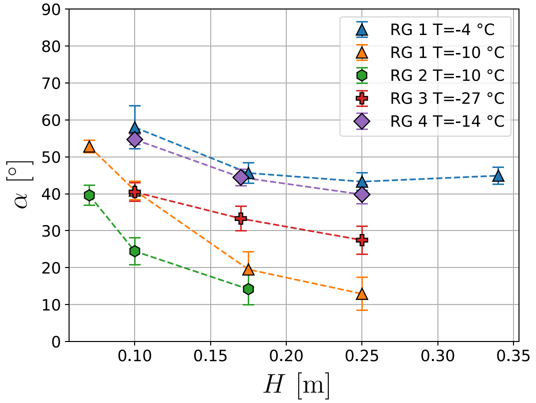

Fig. 13. The α of snow as a function of H for different snow samples with rounded grains and at different T.

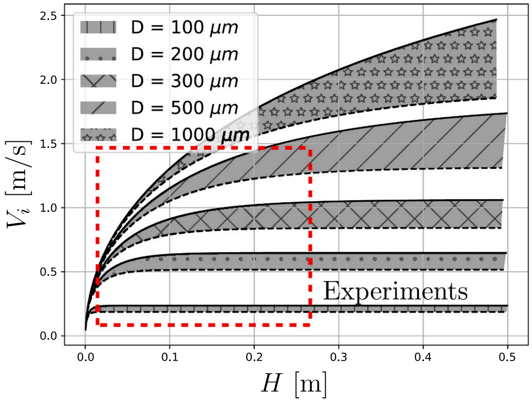

Fig. 14. Predicted V_i of snow grains as a function of H for different grain sizes. Solid lines show spherical grains ($\phi = 1.0$), and dashed lines show non-spherical grains ($\phi = 0.6$), while the shaded areas show the range between these values of ϕ.

with a collisional velocity V_i or reaches its terminal velocity V_∞, which occurs when the two forces are equal. Increasing H, therefore, yields an increase in V_i if $V_i < V_\infty$. The drag force depends on grain size, shape, and the current velocity of the grain. We calculated an estimate of V_i for different grains as a function of H by solving Newton's law of motion using the drag coefficient correlation proposed by Haider and Levenspiel (1989), (cf. their Eq. (11)). The drag coefficient depends on ϕ and the particle Reynolds number Re_p, which is defined as

$$Re_p = \frac{dV_p\rho_f}{\mu}, \tag{10}$$

where V_p is the relative velocity between the particle and the air, and since the air is not moving $V_s = V_i$. In the calculation we used the material properties for air (viscosity μ and density ρ_f) that are valid for $T = -15$°C (NOAA/NASA/USAF, 1976) and we approximate that $\widehat{\phi} \approx \phi$. In Fig. 14 the calculated V_i for different grain radii as a function of H are shown for ϕ between 0.6 (dashed lines) and 1.0 (solid lines) to reflect the range of values obtained for $\widehat{\phi}$. The difference between non-spherical and spherical grains increased with increasing grain size and H. We, therefore, expect that α will be more sensitive to snow shape for large snow grains. All grains are expected to approach a constant V_∞ with sufficiently high H. Each sample had a distribution of grain size, and therefore, we expected that the V_i would vary between grains in a snow sample. By assuming that the d_V and $\widehat{\phi}$ give an overall representation of the grains in each snow sample the data in Fig. 13 can be replotted as a function of V_i. Fig. 15 shows α as a function of the predicted V_i for different snow samples with rounded grains and at different temperatures. The figure shows that V_i was 1 m/s for most samples and α did not change with minor changes in V_i. For example, the $V_\infty \approx 1.4$ m/s was almost reached at $H = 0.25$ m for the RG 1 sample, which explains why a similar α was obtained for $H = 0.34$ m in Fig. 13.

Previous experiments have shown that collisional damping should increase with increasing V_i for ice grains with sufficiently high V_i (Higa et al., 1998; Eidevåg et al., 2021). A model for collisional melting that explains this phenomenon was proposed by Eidevåg et al. (2021). In the present study, V_i was lower than the theoretical stick velocity for collisional melting and was also lower than the critical velocity for ice particles proposed by Higa et al. (1998). Therefore, we expected the coefficient of restitution for these collisions to be almost constant and

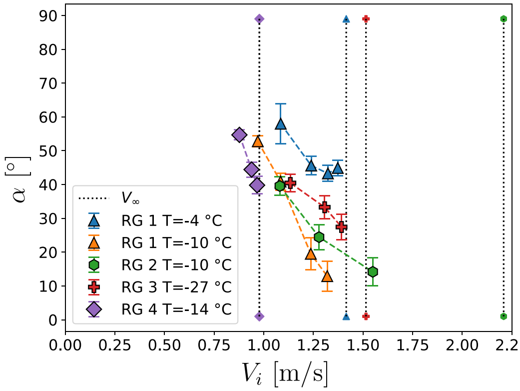

Fig. 15. The α of snow as a function of predicted V_i for different snow samples with rounded grains and different T.

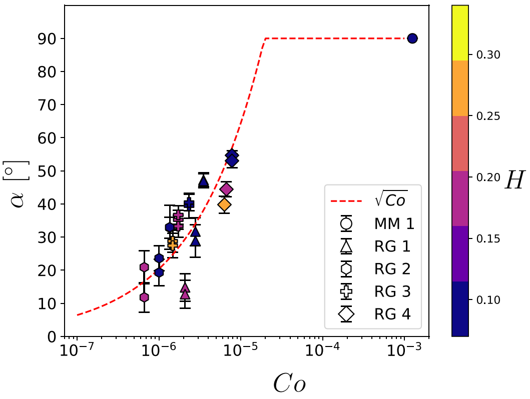

Fig. 16. The α of snow as a function of Co for different snow samples, with shading indicating H. The mean values of repeated trials are plotted with the error bars representing $\delta\alpha$. Dashed red line showing $\alpha = 20000\sqrt{Co}$. (For interpretation of the references to colour in this figure legend, the reader is referred to the web version of this article.)

only weakly dependent on V_i. This means that the collisions should be in the regime where intermolecular forces dominate sticking and not collisional melting (see regime map in Eidevåg et al. (2021)). During the experiments, the snow grains were observed to rebound from initial collision and bounce multiple times before settling. Consequently, we concluded that more grains fall off the base with increased V_i. This is a likely reason why α is sensitive to H. It also implies that more grains should be able to accumulate with increased D_B. We moreover see that h increased with increasing D_B such that the resulting α was constant.

3.5. The cohesion number

The experimental results shown above imply that $\alpha = \alpha(d_V, \widehat{\phi}, T, H)$. The dimensionless number Co depends on three of these key variables where an explicit relationship to T is missing. It can be argued that $W = W(T)$ due to the existence of a quasi-liquid layer on ice (Eidevåg, 2020), however the exact form is unkown. The experimental results imply that there is only a weak dependence on T for sufficiently low T. α is plotted in Fig. 16 as a function of Co for the experimental measurements with $T \leq -12\,°\mathrm{C}$. The material properties W, ρ_p and E^* were taken from what is used in Eidevåg et al. (2019) for ice-ice interactions. The figure also includes the best fit of $\alpha = A\sqrt{Co}$ for $A \approx 20000$ which is based on the dependence $\alpha(Co)$ obtained in Section 3.3. As can be seen in the figure, α generally increases with increasing Co. This is expected given that $Co \propto {V_i}^{-2}{d_V}^{-5/3}$, meaning that Co increases with a decrease in d_V or V_i, i.e., the same dependence as observed in the experiments. For most measurements Co ranged from 10^{-6} to 10^{-5}, except for the MM 1 sample, which had the significantly higher value of 10^{-3}. The results, however, show a spread in values and this could be because W might also depend on particle shape, for the proposed Co now $\widehat{\phi}$ will only affect the predicted V_i due to change in drag coefficient. This analysis assumes that d_V gives an overall representation of the grain sizes in each sample, which might be to crude of a simplification.

4. Conclusions

The α of snow is a seemingly simple parameter to study, dispersing a cloud of snow to fall, collide and accumulate on an upright cylinder. The underlying physics for this parameter are, in contrast, highly complex with nonlinear dependencies on multiple variables. We have presented new experimental measurements for the α of snow that extend the knowledge of ice and snow physics, specifically with regards to the cohesion properties of a dispersed cloud of snow. We have shown that α is sensitive to the variables H, T, d_V, and $\widehat{\phi}$, and that these dependencies are nonlinear. We propose that the non-dimensional cohesion number (Co) represents the dependencies for H, d_V, and $\widehat{\phi}$, and we have shown that there is a clear correlation between α and Co for $T \leq -12\,°\mathrm{C}$.

The α of snow is sensitive to $T > -12°\mathrm{C}$, while it appears rather independent below this range. We have shown that the observed dependence follows an Arrhenius relation, which confirms work by Willibald et al. (2020), and we obtained a similar activation energy (G^+) as in their. These results suggest that $W = W(T)$ however the exact form is unkown.

Our experimental findings for varying H highlight how important this parameter is for the resulting α. For example, the RG 1 sample at $T = -8\,°\mathrm{C}$ had an α that varied from 19° to 90° depending on H. The sensitivity to H was explained by the acceleration of the grains and the resulting V_i. This is a complex relationship that depends on the drag force of the grains and, therefore, depends on both the shape and size of the grains. When modeling snow to predict accretion events, we consequently believe that the drag force and the cohesive properties of snow are important to get right, for example, when using Discrete Element Method or Smoothed Particle Hydrodynamics.

We found that α increases with decreasing d_V for the snow samples studied; machine made snow was the extreme case with diverging α even at $T = -13\,°\mathrm{C}$. The α of snow with rounded grains collected outdoors from the ground, ranges from 20° to 40° for sufficiently low T with $H = 0.1$ m, while increased with increasing T until a diverging α, i.e., $\alpha = 90°$ was reached.

The α of snow can be used as a measure of cohesive properties when creating machine made snow. We have shown that the cohesive properties of a snow sample created with a snow cannon (the MM 1 sample) were significantly different from any naturally collected snow samples with a diverging α for all measurements. A clear difference was also observed between surface hoar crystals (the SH 1 sample) and precipitation particles (the PP 1 sample), where the PP 1 sample had a higher α than the SH 1 sample. These differences imply that measuring the α of snow can be a useful cohesion measure when manufacturing snow, for example, from a snow cannon or with vapor growth in a laboratory, which is a method often used in snow science.

Declaration of Competing Interest

The authors declare that they have no known competing financial interests or personal relationships that could have appeared to influence the work reported in this paper.

Acknowledgments

This work was funded by VINNOVA (2017-03029). EST is supported by the Swedish Research Councils, FORMAS (2017-00564) and VR (2020-03497), and by the Swedish Strategic Research Area MERGE.

Appendix A. Repeatability of measurements

The repeatability of the experimental trials was studied to assure the reliability of the measured α. The T studied in this work was close to the melting temperature of water, which makes the snow samples studied sensitive to environmental changes. The morphology of the snow grains was also expected to change over time due to snow metamorphism (Colbeck, 1982). Thus it was important to monitor repeatability to ensure that morphological changes in snow samples during experimental trials did not affect α. We observed that the experimentally determined α of the same snow sample at the same T was repeatably obtained with little variation between trials. An example is shown in Fig. A.1. The figure shows the experimental measurements of α for sample RG 1 for four different trials at $T = -10^\circ$C. The sample consisted of around 30 l of snow. Ensuring that different snow grains were present in the different measured heaps. However, the α for the different trials were almost exactly the same. For these measurements, the α was estimated to be $41 \pm 3^\circ$. We observed few cases with larger uncertainty, for example, the average value was estimated to be $\alpha = 52 \pm 8^\circ$ for the RG 2 sample, with $T = -2^\circ$C and $H = 0.25$. However, the changes in α observed for the different T and H in this work were significant compared to the uncertainties.

Measurements of the samples RG 1 and RG 2 were performed over 3 days, and therefore, repeatability was examined during this time by repeating the experiments after 14 h but at the same conditions (with the snow at rest overnight). We observed no statistically significant differences in the α between these trials and, therefore, conclude that the rate of change due to metamorphism was slow and only had a minor influence on the shape and size of the snow grains during the experimental time frame. Repeatability over time was also performed for sample PP 1 to compare freshly collected fallen snow with the same sample aged for 16 h at -12°C. We observed a lower α for all measurements of the aged PP 1 sample with an average difference of 4°. This is expected since fresh snow, with a high specific surface area, has a faster metamorphism rate than granular snow with a low specific surface area (Eppanapelli, 2018).

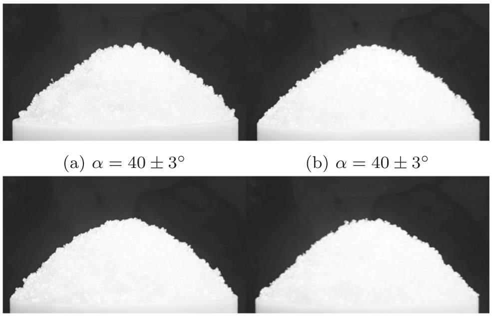

(a) $\alpha = 40 \pm 3^\circ$ (b) $\alpha = 40 \pm 3^\circ$

(c) $\alpha = 42 \pm 2^\circ$ (d) $\alpha = 41 \pm 2^\circ$

Fig. A.1. Four repeated measurements for the α of snow on RG 1 sample at $T = -10^\circ$C and $H = 0.1$ m.

References

Abrahamsson, P., Eng, M., Rasmuson, A., 2018. An infield study of road snow properties related to snow-car adhesion and snow smoke. Cold Reg. Sci. Technol. 145, 32–39. https://doi.org/10.1016/j.coldregions.2017.09.008.

Al-Hashemi, H.M.B., Al-Amoudi, O.S.B., 2018. A review on the angle of repose of granular materials. Powder Technol. 330, 397–417. https://doi.org/10.1016/j.powtec.2018.02.003.

Bagheri, G., Bonadonna, C., 2016. Aerodynamics of volcanic particles. Volcanic Ash 39–52. https://doi.org/10.1016/b978-0-08-100405-0.00005-7.

Behjani, M.A., Rahmanian, N., Ghani, N. Fardina Abdul, Hassanpour, A., 2017. An investigation on process of seeded granulation in a continuous drum granulator using DEM. Adv. Powder Technol. 28, 2456–2464. https://doi.org/10.1016/j.apt.2017.02.011.

Borrebæk, P.O.A., Jelle, B.P., Zhang, Z., 2020. Avoiding snow and ice accretion on building integrated photovoltaics – challenges, strategies, and opportunities. Sol. Energy Mater. Sol. Cells 206. https://doi.org/10.1016/j.solmat.2019.110306.

Cadle, R.D., 1965. Particle Size - Theory and Industrial Applications. Reinhold Publishing Corporation.

Chokshi, A., Tielens, A.G.G.M., Hollenbach, D., 1993. Dust coagulation. Astrophys. J. 407, 806–819. https://doi.org/10.1086/172562.

Colbeck, S.C., 1982. An overview of seasonal snow metamorphism. Rev. Geophys. Space Phys. 20, 45–61. https://doi.org/10.1029/RG020i001p00045.

Colbeck, S.C., 1997. A review of sintering in seasonal snow. CRREL Rep. 12.

Cuffey, K., Paterson, W.S., 2006. The Physics of Glaciers, 4th editio ed. Academic press. https://doi.org/10.3189/002214311796405906.

Dash, J.G., Haiying, Fu, Wettlaufer, J.S., 1995. The premelting of ice and its environmental consequences. Rep. Prog. Phys. 58, 115–167. https://doi.org/10.1088/0034-4885/58/1/003.

Dash, J.G., Mason, B.L., Wettlaufer, J.S., 2001. Theory of charge and mass transfer in ice-ice collisions. J. Geophys. Res. 106, 395–415. https://doi.org/10.1029/2001JD900109.

Dash, J.G., Rempel, A.W., Wettlaufer, J.S., 2006. The physics of premelted ice and its geophysical consequences. Rev. Mod. Phys. 78, 695–741. https://doi.org/10.1103/RevModPhys.78.695.

Dominik, C., Tielens, A.G.G.M., 1997. The Physics of Dust Coagulation and the Structure of Dust Aggregates in Space. Astrophys. J. 480, 647–673. https://doi.org/10.1086/303996.

Eidevåg, T., 2020. Snow Contamination of Cars: Collisions of Ice Particles with Surfaces. Licentiate thesis. Chalmers University of Technology.

Eidevåg, T., Abrahamsson, P., Eng, M., Rasmuson, A., 2019. Modeling of dry snow adhesion during normal impact with surfaces. Powder Technol. 361, 1081–1092. https://doi.org/10.1016/j.powtec.2019.10.085.

Eidevåg, T., Thomson, E.S., Sollén, S., Casselgren, J., Rasmuson, A., 2021. Collisional damping of spherical ice particles. Powder Technol. 383, 318–327. https://doi.org/10.1016/j.powtec.2021.01.025.

Eppanapelli, L.K., 2018. Experimental Investigation of Snow Metamorphism at near-Surface Layers. Doctoral thesis. Luleå University of Technology.

Fierz, C., Armstrong, R., Durand, Y., Etchevers, P., Greene, E., McClung, D., Nishimura, K., Satyawali, P., Sokratov, S., 2009. The international classification for seasonal snow on the ground. In: IHP-VII Technical Documents in Hydrology, vol. 83, p. 90.

French, R.H., Parsegian, V.A., Podgornik, R., Rajter, R.F., Jagota, A., Luo, J., Asthagiri, D., Chaudhury, M.K., Chiang, Y.M., Granick, S., Kalinin, S., Kardar, M., Kjellander, R., Langreth, D.C., Lewis, J., Lustig, S., Wesolowski, D., Wettlaufer, J.S., Ching, W.Y., Finnis, M., Houlihan, F., Von Lilienfeld, O.A., Van Oss, C.J., Zemb, T., 2010. Long range interactions in nanoscale science. Rev. Mod. Phys. 82, 1887–1944. https://doi.org/10.1103/RevModPhys.82.1887.

Goldsby, D.L., Kohlstedt, D.L., 2001. Superplastic deformation of ice: Experimental observations. J. Geophys. Res. Solid Earth 106, 11017–11030. https://doi.org/10.1029/2000jb900336.

Haider, A., Levenspiel, O., 1989. Drag coefficient and terminal velocity of spherical and nonspherical particles. Powder Technol. 58, 63–70. https://doi.org/10.1016/0032-5910(89)80008-7.

Heil, K., Kaitna, R., Fischer, J.-T., Reiweger, I., 2018. Granulation experiments with snow in a rotating drum, in. Int. Snow Sci. Workshop 21, 94–97.

Higa, M., Arakawa, M., Maeno, N., 1998. Size dependence of restitution coefficients of ice in relation to collision strength. Icarus 133, 310–320. https://doi.org/10.1006/icar.1998.5938.

Holicky, M., Sykora, M., 2009. Failures of roofs under snow load: causes and reliability analysis. In: Forensic Engineering, Proceedings of the Congress, pp. 444–453. https://doi.org/10.1061/41082(362)45.

Jellinek, H.H., 1967. Liquid-like (transition) layer on ice. J. Colloid Interface Sci. 25, 192–205. https://doi.org/10.1016/0021-9797(67)90022-7.

Kuroiwa, D., Mizuno, Y., Takeuchi, M., 1967. Micromeritical porperties of snow. In: International Conference on Low Temperature Science. I. Conference on Physics of Snow and Ice, II. Conference on Cryobiology, pp. 751–772.

NOAA/NASA/USAF, 1976. U.S Standard Atmosphere 1976, Technical Report. U.S. Government Printing, Washington, D.C.

Schweizer, J., Jamieson, J.B., 2001. Snow cover properties for skier triggering of avalanches. Cold Reg. Sci. Technol. 33, 207–221. https://doi.org/10.1016/S0165-232X(01)00039-8.

Weertman, J., 1983. Creep deformation of ice. Annu. Rev. Earth Planet. Sci. 11, 215–240. https://doi.org/10.1146/annurev.ea.11.050183.001243.

Wettlaufer, J., Worster, M.G., 2005. Premelting dynamics. Annu. Rev. Fluid Mech. 38, 427–452. https://doi.org/10.1146/annurev.fluid.37.061903.175758.

Willibald, C., Löwe, H., Theile, T., Dual, J., Schneebeli, M., 2020. Angle of repose experiments with snow: role of grain shape and cohesion. J. Glaciol. 1–9. https://doi.org/10.1017/jog.2020.36.

Woodcock, C.R., Mason, J.S., 1988. Bulk Solids Handling. Springer Netherlands, Dordrecht. https://doi.org/10.1007/978-94-009-2635-6.

PAPER IV

Snow contamination of simplified automotive bluff bodies: A comparison between wind tunnel experiments and numerical modeling